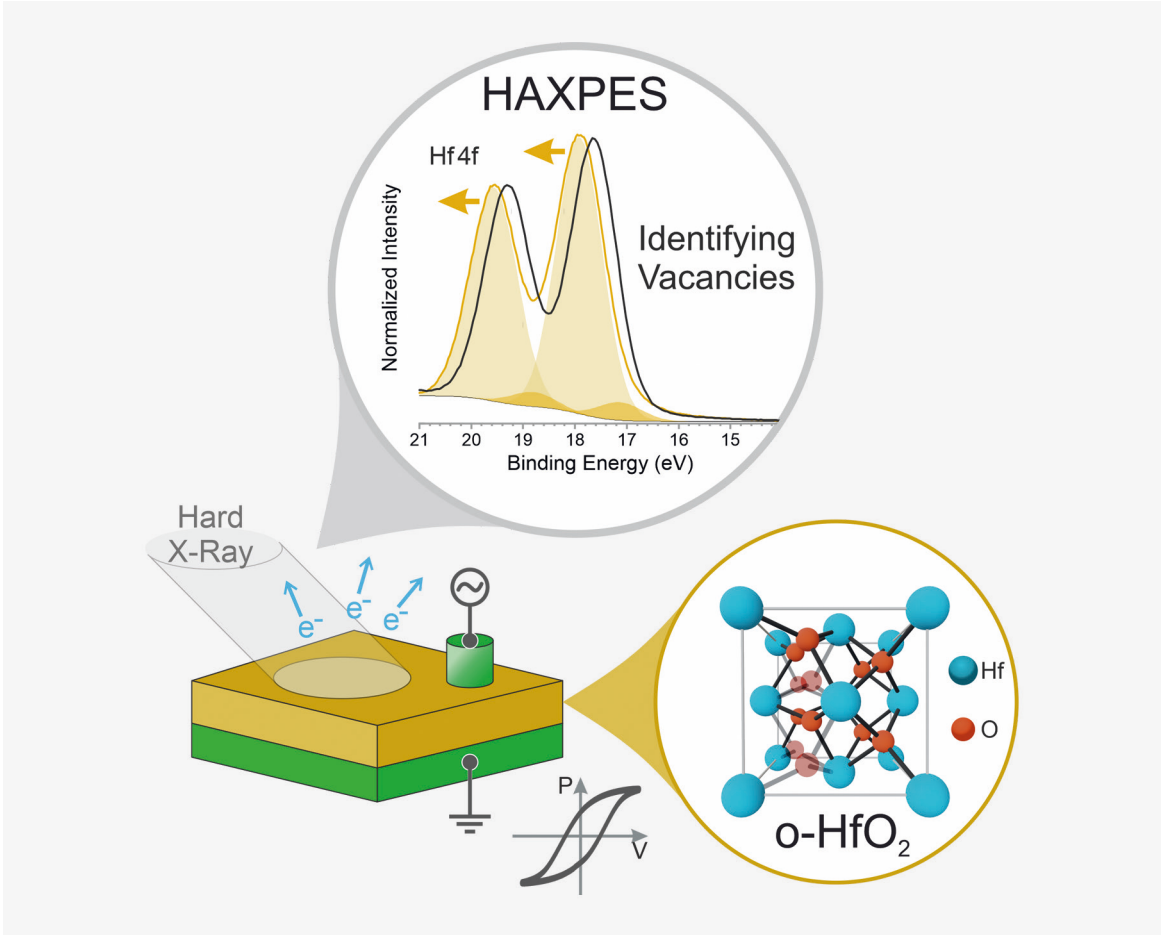

HAXPES study of interface and bulk chemistry of ferroelectric HfO_2 capacitors

Thomas Szyjka

Information
Band / Volume 94
ISBN 978-3-95806-692-2

Mitglied der Helmholtz-Gemeinschaft

JÜLICH
Forschungszentrum

Schriften des Forschungszentrums Jülich
Reihe Information / Information Band / Volume 94

Forschungszentrum Jülich GmbH
Peter Grünberg Institut (PGI)
Elektronische Eigenschaften (PGI-6)

HAXPES study of interface and bulk chemistry of ferroelectric HfO_2 capacitors

Thomas Szyjka

Schriften des Forschungszentrums Jülich
Reihe Information / Information Band / Volume 94

ISSN 1866-1777 ISBN 978-3-95806-692-2

Bibliografische Information der Deutschen Nationalbibliothek.
Die Deutsche Nationalbibliothek verzeichnet diese Publikation in der
Deutschen Nationalbibliografie; detaillierte Bibliografische Daten
sind im Internet über http://dnb.d-nb.de abrufbar.

Herausgeber und Vertrieb:	Forschungszentrum Jülich GmbH Zentralbibliothek, Verlag 52425 Jülich Tel.: +49 2461 61-5368 Fax: +49 2461 61-6103 zb-publikation@fz-juelich.de www.fz-juelich.de/zb
Umschlaggestaltung:	Grafische Medien, Forschungszentrum Jülich GmbH
Druck:	Grafische Medien, Forschungszentrum Jülich GmbH
Copyright:	Forschungszentrum Jülich 2023

Schriften des Forschungszentrums Jülich
Reihe Information / Information, Band / Volume 94

D 352 (Diss. Konstanz, Univ. 2022)

ISSN 1866-1777
ISBN 978-3-95806-692-2

Vollständig frei verfügbar über das Publikationsportal des Forschungszentrums Jülich (JuSER)
unter www.fz-juelich.de/zb/openaccess.

Kurzzusammenfassung

HfO_2 ist das erste bekannte ferroelektrische Material welches nur aus zwei Elementen gebildet wird. Die Entdeckung der ferroelektrischen Eigenschaften fand 2011 in Si dotierten HfO_2 Dünnschichtfilmen statt. Hierdurch wurden weitreichende Untersuchungen angeregt, die die Grundlagen und den Ursprung der ferroelektrischen Eigenschaften in HfO_2 basierenden Materialien studieren sowie mögliche Anwendungen in der Halbleiterindustrie erforschen. Als ferroelektrische Phase wurde die orthorhombische Kristallstruktur im HfO_2 identifiziert.
Diese Arbeit findet im Rahmen des EU Projekts 3ϵFERRO statt, die darauf abzielt auf HfO_2 basierende nichtflüchtige Speichermedien zu konzipieren. Hierbei hat HfO_2 die Rolle eines Dielektrikum, welches in einer Kondensatorstruktur von zwei Elektroden umschlossen ist. Zur Erreichung der Projektziele wird eine anwendungsnahe Grundlagenforschung benötigt, die Optimierungsmöglichkeiten der ferroelektrischen Materialien und Grenzflächen zu den Elektroden hervorbringt.
In dieser Arbeit werden anwendungsnahe HfO_2 basierende Kondensator Strukturen mithilfe von Harter Röntgen-Photoelektronenspektroskopie (HAXPES) untersucht. Hierbei liegt der Schwerpunkt in der Identifikation von stabilisierenden Faktoren für die ferroelektrische Phase in der HfO_2 Schicht, sowie die Bestimmung des Einflusses der Elektroden auf die elektrischen und ferroelektrischen Eigenschaften des Kondensators. Der wichtigste stabilisierende Faktor in dieser Arbeit sind Sauerstofffehlstellen im HfO_2 Gitter. Insgesamt werden drei unterschiedliche Probenreihen untersucht, wobei die erste aus TiN/HfO_2/TiN Filmschichten besteht, aufgebracht durch Physikalische Gasphasenabscheidung (PVD). In dieser Probenreihe wird die Sauerstofffehlstellenkonzentration mittels eines zusätzlichen O_2 Gasflusses während der HfO_2 Abscheidung reduziert. Durch die chemische Charakterisierung mittels HAXPES kann die relative Dichte von Sauerstofffehlstellen sowie durch Sauerstofffehlstellen induzierte Bildung zusätzlicher Zustände in der Bandlücke quantifiziert werden. Zudem wurde ein TiO_2 Signal gemessen, welches der unteren Elektrode zugeschrieben werden kann. Diese TiO_2 Zwischenschicht ist das Ergebnis einer Oxidation der unteren Elektrode durch den zusätzliche O_2 Gasfluss. Die Schichtdicke vom TiO_2 korreliert unmittelbar mit der Dosierung des Gasflusses und ist selbstlimitierend. Im Herstellungsprozess der Filmschichten gibt es einen Ausheizprozess der benötigt wird, damit die Schichten kristallisieren. Die TiO_2-Zwischenschicht verhindert jeglichen Austausch zwischen der TiN-Bodenelektrode und der HfO_2-Schicht während des Ausheizprozesses. Ohne diese Schicht können O- und N-Atome ausgetauscht werden, und zusätzliche Sauerstofffehlstellen in HfO_2 entstehen. Die Erkenntnisse aus den HAXPES Messungen lassen sich mit den ferroelektrischen Eigenschaften der Proben korrelieren, welche durch dynamische Hysterese Messungen (DHM) bestimmt wurden. Die DHM und weitere Vorstudien an den Proben wurden vom Projektpartner NaMLab durchgeführt. Die Korrelation der Ergebnisse ergibt, dass eine erhöhte Sauerstofffehlstellenkonzentration als auch die Existenz einer TiO_2 Zwischenschicht zwischen der unteren Elektrode und der HfO_2 Schicht die Stabilität der ferroelektrischen Phase positiv beeinflussen.
Als weitere Probenreihe wird ein identischer Schichtaufbau genutzt, wobei die HfO_2 Schicht anstelle von PVD mit Atomlagenabscheidung (ALD) aufgebracht wurde. Der identische Aufbau ermöglichte einen direkten Vergleich mit der vorangegangenen Probenreihe und somit auch ein Vergleich der beiden Methoden PVD und ALD. ALD basiert auf Zyklen, bei denen die Probenstruktur einem Ausgangsmolekül, welches das Hf Atom beinhaltet, sowie einem Reaktant, hier Ozon, abwechselnd ausgesetzt werden. Die Ausgangsmoleküle bilden einen Monolage, und werden durch den Reaktanten aufgebrochen, sodass sich eine Monolage HfO_2 formen kann. Die HAXPES Messungen ergibt, dass die Nutzung des Ausgangsmoleküls ($[(CH_3)(C_2H_5)N]_4Hf$), zusätzliche Verunreinigungen von C und N in die HfO_2 Schicht einbringt. Die erhöhte N Konzentration in den ALD Proben im Vergleich zu den PVD Proben hat einen direkten Einfluss auf die Art wie sich

die Sauerstofffehlstellen formen. Durch spektrale Merkmale in den HAXPES Messungen kann festgestellt werden, dass die N Atome in den ALD Proben einen Verbund mit den Sauerstofffehlstellen bilden und diese dadurch stabiler gegenüber äußeren elektrischen Feldern werden lassen.
Als letzte Probenreihe werden $IrO_2/HfZrO_4/IrO_2$ Kondensatoren untersucht. Hier liegt der Fokus auf die Wechselwirkungen der IrO_2 Elektroden mit der ferroelektrischen Schicht. Teil des Herstellungsprozesses der Kondensatoren ist ein Ausheizprozess bei dem das IrO_2 O Atome dem $HfZrO_4$ potenziell zur Verfügung stellen kann und somit die Sauerstofffehlstellenkonzentration lokal ändert. Die Atmosphäre während des Ausheizprozesses beeinflusst maßgeblich die Eigenschaften der Kondensatoren. Die Proben wurden in O_2, N_2 und Formiergas (FG) ausgeheizt. FG hat reduzierende Eigenschaften und besteht aus einem N_2:H_2 Gasgemisch im Verhältnis 9:1. Das Ausheizen in FG führte zu einer Reduktion der oberen Elektrode von IrO_2 zu Ir, einer erhöhten Sauerstofffehlstellenkonzentration am Interface und einem erhöhten Anteil der ferroelektrischen Phase im Vergleich zu Proben, die in Sauerstoff (Stickstoff) ausgeheizt wurden. In der reduzierten Elektrode können Spuren von ungebundenem Sauerstoff im Ir Gitter nachgewiesen werden. Zusätzliche HAXPES Messungen fanden an $IrO_2/HfZrO_4/IrO_2$ Proben statt, die in FG ausgeheizt und mit einem wechselnden elektrischen Feld behandelt wurden. Als Auswirkung des elektrischen Feldes nach 10^6 Schaltvorgängen kann festgestellt werden, dass die ungebundenen Sauerstoffatome im Ir mobil sind und sich am Interface zwischen der $HfZrO_4$ und Ir Schicht ansammeln. Hierbei werden Sauerstofffehlstellen im $HfZrO_4$ aufgefüllt und ein IrO_2 Grenzschicht geformt. Gleichzeitig kann festgestellt werden, dass sich bei dieser Anzahl an Schaltvorgängen die gemessene ferroelektrische Hysterese schließt und der Kondensator seine ferroelektrischen Eigenschaften verliert. Somit kann der Zusammenbruch der Ferroelektrizität im direkten Zusammenhang mit dem mobilen Sauerstoff gebracht werden.
Zusammenfassend kann auf der einen Seite die Detektierung und Unterscheidung von Sauerstofffehlstellen mittels HAXPES etabliert und zum anderen dessen Bedeutung für die Stabilität der ferroelektrischen Phase quantifiziert werden. Zudem kann der Einfluss der Elektroden auf die ferroelektrische Schicht ermittelt werden. Die mittels HAXPES ermittelten chemischen Unterschiede und Veränderungen kann direkt mit den durch DHM ermittelten ferroelektrischen Eigenschaften korreliert werden. Die Erkenntnisse können zum Teil als konkrete Designvorschläge zur Optimierung des ferroelektrischen Materials gesehen werden und regten innerhalb des EU Projekts weitere Untersuchungen an.

Abstract

HfO_2 is the first known ferroelectric material formed from only two elements. The discovery of the ferroelectric properties took place in 2011 in Si-doped HfO_2 thin films. This stimulated widespread investigations on the fundamentals and origin of the ferroelectric properties in HfO_2 based materials and the exploration of potential applications in the semiconductor industry. The orthorhombic crystal structure in HfO_2 has been identified as the ferroelectric phase. This work takes place in the framework of the EU project 3ϵFERRO, which aims to design HfO_2 based nonvolatile memory. Here, HfO_2 has the role of a dielectric enclosed by two electrodes in a capacitor structure. To achieve the project goals, application-oriented fundamental research is needed to produce optimization options for the ferroelectric materials and interfaces to the electrodes.
This thesis investigates applied HfO_2 based capacitor structures using hard X-ray photoelectron spectroscopy (HAXPES). Here, the focus is on identifying stabilizing factors for the ferroelectric phase in the HfO_2 layer, as well as determining the influence of the electrodes on the electrical and ferroelectric properties of the capacitor. The main stabilizing factor in this work is oxygen vacancies in the HfO_2 lattice. A total of three different sample sets are investigated, the first consisting of TiN/HfO_2/TiN film layers deposited by physical vapor deposition (PVD). In this sample set, the density at oxygen defects is reduced through an additional O_2 gas flow during HfO_2 deposition. Chemical characterization using HAXPES can quantify the relative density of oxygen vacancies as well as oxygen vacancy induced formation of additional states in the bandgap. In addition, a TiO_2 signal was measured that can be attributed to the bottom electrode. This TiO_2 interlayer is the result of oxidation of the bottom electrode by the additional O_2 gas flow. The film thickness of TiO_2 correlates directly with the gas flow rate and is self-limiting. In the manufacturing process of the film layers, an annealing process is required for the crystallization of the layers. The TiO_2 interlayer inhibits any exchange between the TiN bottom electrode and the HfO_2 layer during the annealing process. Without this layer, O and N atoms can be exchanged, and additional oxygen vacancies can be created in HfO_2. The findings from the HAXPES measurements can be correlated with the ferroelectric properties of the samples, which were determined by dynamic hysteresis measurements (DHM). The DHM and other preliminary studies on the samples were performed by the project partner NaMLab. The correlation of the results shows that an increased oxygen defect concentration, as well as the existence of a TiO_2 interlayer between the bottom electrode and the HfO_2 layer, positively influence the stability of the ferroelectric phase.
Another sample set with an identical layer structure is investigated where the HfO_2 layer was deposited with atomic layer deposition (ALD) instead of PVD. The similar layer structure allows a direct comparison with the previous sample set and thus a comparison of the two methods PVD and ALD. ALD is based on cycles in which the sample structure is alternately exposed to a precursor molecule containing the Hf atom and a reactant (ozone). The precursor molecules form a monolayer and are broken up by the reactant, allowing a monolayer of HfO_2 to form. The HAXPES measurements reveal that the use of the precursor ($[(CH_3)(C_2H_5)N]_4Hf$) introduces additional impurities of C and N into the HfO_2 layer. The increased N concentration in the ALD samples compared

to the PVD samples has a direct impact on the constellation of the oxygen vacancies. Through spectral features in the HAXPES measurements, it can be determined that the N atoms in the ALD samples form a complex with the oxygen vacancies, making them more stable to external electric fields.
As the last sample set, $IrO_2/HfZrO_4/IrO_2$ capacitors are investigated. Here the focus is on the interactions of the IrO_2 electrodes with the ferroelectric layer. Part of the capacitor fabrication process is an annealing process where the IrO_2 can potentially provide O atoms to the $HfZrO_4$, thus changing the oxygen defect concentration locally. The atmosphere during the annealing process significantly affects the properties of the capacitors. The samples were annealed in O_2, N_2 and forming gas (FG). FG has reducing properties and consists of an N_2:H_2 gas mixture in a ratio of 9:1. Annealing in FG resulted in a reduction of the top electrode from IrO_2 to Ir, an increased oxygen vacancy concentration at the interface, and an increased fraction of the ferroelectric phase compared to samples annealed in oxygen (nitrogen). In the reduced electrode, traces of unbound oxygen can be detected in the Ir lattice. Additional HAXPES measurements were performed on $IrO_2/HfZrO_4/IrO_2$ samples annealed in FG and treated with an alternating electric field. As an effect of the electric field, after 10^6 switching, it can be found that the unbound oxygen atoms in the Ir are mobile and accumulate at the interface between the $HfZrO_4$ and Ir layer. In this process, oxygen vacancies in the $HfZrO_4$ are filled, and an IrO_2 layer is formed at the interface. At the same time, it can be observed that at this number of switching cycles, the measured ferroelectric hysteresis closes, and the capacitor loses its ferroelectric properties. Thus, the collapse of ferroelectricity can be directly related to mobile oxygen.
In summary, on the one hand, the detection and discrimination of oxygen defects can be established via HAXPES. On the other hand, the significance of oxygen vacancies for the stability of the ferroelectric phase can be quantified. In addition, the influence of the electrodes on the ferroelectric layer can be determined. The chemical differences and changes determined by HAXPES can be directly correlated with the ferroelectric properties determined by DHM. The findings can partly be seen as concrete design proposals for the optimization of the ferroelectric material and stimulated further investigations within the EU project.

Contents

CHAPTER 1

Introduction

We live in an era in which the digitalization of our daily life and the living environment is in an important stage of development. The future technology is driven by the increasing widespread networking of everyday objects and industrial machines via the Internet, known as the *Internet of Things* (IoT). Due to the wide-ranging applications, there is a constant search for ways to implement IoT as cost-effectively and energy-efficiently as possible. Ideally, data is captured and processed in one sensor, creating the necessity for energy-efficient microprocessor units combined with high endurance *embedded non-volatile memories* (eNVM). Although *ferroelectric random access memories* (FeRAMs) have the highest endurance, their use has been limited for a long time since classic FeRAMs are perovskite-based and thus have limited scalability of the memory cell and poor compatibility with the Si-based complementary metal-oxide-semiconductor (CMOS) technology.
The situation radically changed with the discovery of ferroelectricity in doped HfO_2 thin films in 2011 [1]. From the fundamental point of view, the finding of a ferroelectric phase in the HfO_2 thin film was surprising since no thermodynamically stable phase was predicted under standard fabrication conditions [2, 3]. Compared to perovskite-based materials, HfO_2 has a much stronger bonding between the cation and the anions, making HfO_2-based materials more robust to degradation in very thin films $< 10\,\text{nm}$ (*scalability*) and at the exposure to reducing gases (*compatibility with CMOS technology*) [4]. These properties nurture the prospect of an entire range of cutting-edge semiconductor device applications [5–8]. Non-ferroelectric HfO_2 is already used as a high-permittivity (κ) gate insulator substituting Si in high-performance field-effect transistors (FETs), thus enabling a quick transition from fundamental research into actual devices based on ferroelectric HfO_2. The experiments in this thesis took place in the framework of the EU project 3ϵFERRO, which had as its objective the optimization of the material properties in the HfO_2-based ferroelectric capacitor stack and the integration of ferroelectric-

Hf(Zr)O_2-based NVM arrays with CMOS.
Since the discovery of ferroelectric HfO_2 thin films, many studies have already been conducted, determining stabilizing factor of the ferroelectric phase (e.g., doping, film thickness, thermal budget) [9], as well as the electrical properties of HfO_2-based metal-insulator-metal (MIM) hetero-structures, showing that the ferroelectric properties change over repetitive electrical field switching. The challenge still to face is to find the optimal combination of ferroelectric Hf(Zr)O_2 thin films and electrode metals, supporting applicable ferroelectric properties, which are reasonably constant over repetitive electrical field switching. Understanding the interaction between the different layers within this framework and building a fundamental understanding of how the manufacturing process affects the properties of the interfaces and ferroelectric layer is crucial. Furthermore, stabilizing factors like oxygen vacancies V_O have been identified by electrical characterizations.
This work tries to tackle those challenges by holistically studying the electrical and chemical properties of application-oriented HfO_2-based MIM structures. To realize such an investigation, the sample preparation and electrical characterization have been taken over by the cooperation partner NaMLab (Dresden, Germany), which are then complemented by in-depth chemical characterization presented in this work. Here Hard X-ray Photoelectron Spectroscopy (HAXPES) is used as a nondestructive technique, enabling the element-selective study of the chemical composition in the complete MIM layer stack. Since oxygen vacancies affect the chemical properties, HAXPES makes it also possible to detect V_O and to compare the V_O concentration.

This thesis is organized as follows: In **Chapter 2**, the basics of ferroelectricity are covered, followed by a description of the emergence of a ferroelectric phase in HfO_2, how it can be stabilized and affected by electric field switching. The second part of this chapter conveys the theoretical background of photoelectron spectroscopy, the implementation in the performed experiments, and the features composing the photoemission spectra. The end of this chapter is dedicated to the concept of information depth, illustrating the exceptionally enhanced depth sensitivity of HAXPES compared to conventional soft x-ray XPS and the respective technical requirements.
The different experimental aspects, beginning with a description of the samples and the pre-characterization, are covered in **Chapter 3**. Furthermore, a major focus in this chapter is on the description of the HAXPES measurement and analysis of the experimental data. The description of the data analysis is structured like a step-by-step guide, making it possible to be applied to any photoelectron spectra. An essential part of the analysis is the determination of layer thicknesses of buried layers in multilayer systems. The last part of this chapter derives the required formula of thickness determination for a two-layer model as well as their application to the experimental data.
The following three chapters present the results, each based on a different publication. The chapters are arranged so that the knowledge gained by the given result builds on each other. In chapter 4, the results of TiN/HfO_2/TiN samples are shown, which are deposited by Physical Vapor Deposition (PVD) and used an additional oxygen flow during the deposition of the HfO_2 layer, aiming to reduce the V_O concentration in a

controlled manner. Comparing the HAXPES measurements of samples with varying O_2 flow enabled the deduction of spectral features related to V_O. Additionally to the V_O concentration, the TiN bottom electrode is affected by the O_2 flow changing the composition of the interface between the bottom electrode and the HfO_2 layer to a TiO_2 interlayer. Since all samples are also electrically characterized, a direct correlation between the ferroelectric properties and the bottom interface as well as the V_O concentration can be established.
Chapter 5 covers the effects different deposition techniques have on the properties of the HfO_2 layer. Here the PVD-samples discussed in the previous chapter are compared to $TiN/HfO_2/TiN$ samples, where the HfO_2 is deposited using Atomic Layer Deposition (ALD). The HAXPES measurements reveal spectral features related to oxygen vacancies in the ALD-samples, but which are different from those in the PVD-samples. Thus different constellations of oxygen vacancies and their effects on the ferroelectric properties can be determined.
Chapter 6 expands the study using IrO_2 as electrode material, which has the potential to be an oxygen donor, reducing the V_O concentration at the interface. Here the samples have an $IrO_2/HfZrO_4/IrO_2$ layer structure and differ in the gas used during the annealing process, which is needed to crystallize the sample. The gases used are nitrogen, oxygen, and forming gas, which is a reducing gas mixture (N_2:H_2 in a 9:1 ratio), commonly used in the CMOS technology. Each chemical change induced by the annealing gas could thus be tracked. In addition, HAXPES measurements were conducted on a forming gas annealed sample, which was exposed to switching electrical fields. This sample allowed an investigation of the electrical field-induced chemical changes.
Finally, in chapter 7, the main results of this thesis are summarized and discussed.

CHAPTER 2

Background

Obtaining a thorough understanding of the underlying mechanisms behind the emergence of ferroelectricity in HfO_2 thin films and capacitors requires a holistic chemical and electrical characterization approach. This chapter provides a summary of the theoretical background, with sec. 2.1 focusing on ferroelectricity, its manifestation and stabilization in HfO_2, as well as the modifications occurring in HfO_2-based capacitors due to electrical field cycling. Section 2.2 covers the theoretical basics of photoelectron spectroscopy, the discussion of spectral features (sec. 2.2.3), and characteristics of a HAXPES experiment (sec. 2.2.5).

2.1. Ferroelectricity and HfO_2: Structural and electrical properties

2.1.1. Basics of ferroelectricity

Ferroelectricity is a material's property observed only in noncentrosymmetric crystals and characterized by a permanent (spontaneous) and reorientable polarization. The attribute of reorientable polarization can not be directly identified by the crystallographic structure and must be established by measuring the polarization response to an electric field. The hysteretic shape of the response to an external electrical field inspired the name *ferroelectricity* since similarly shaped hystereses define *ferromagnetism* in external magnetic fields (see Fig. 2.1). Further similarities are the existence of a Curie temperature and the formation of domains.
Generally, while an external electric field (E) polarizes a material, a polarization (P) is induced linearly proportional to the magnitude of E. This relation is called dielectric polarization. Above the Curie temperature T_C, ferroelectric materials are in a paraelectric

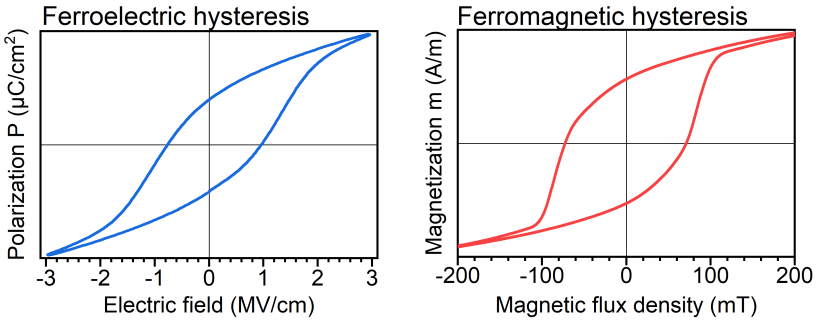

Figure 2.1.: Representation of ferroelectric and ferromagnetic hystereses. The data stem from a ferroelectric HfO_2 sample and a magnetic $Fe_{60}Al_{40}$ alloy.

phase and a nonlinear polarization is present with respect to an external electric field. Thus, the electric permittivity, defined by the slope of the polarization curve, is not constant. Below T_C, in addition to the nonlinearity, a spontaneous nonzero polarization stabilizes without an applied external field. Due to the reversibility of the spontaneous polarization by a sufficiently strong electric field, P is dependent on the currently applied electric field as well as the history, leading to the emergence of a hysteresis loop.
In a ferroelectric material, the electric dipoles and the crystal lattice are coupled. Thus, variation in the lattice can affect the strength of the spontaneous polarization. The lattice structure can, for example, be changed by mechanical force and temperature. If external stress results in the generation of surface charges, a material is classified as piezoelectric, while the change in spontaneous polarization due to the change in temperature is named pyroelectricity.
All crystals can be categorized into 32 point groups, where 21 classes are noncentrosymmetric, which is a necessary condition for piezoelectricity to exist. Twenty of them are piezoelectric, and among them, 10 crystals have pyroelectric properties. The necessity for a permanent dipole makes each ferroelectric crystal also a pyroelectric, limiting the possible crystal structures to the 10 pyroelectric groups. The feature distinguishing the ferroelectric crystal from all other pyroelectric crystals is the reorientability of the dipole moment by an external electric field [10, 11].

Phenomenological description of ferroelectricity

A phenomenological thermodynamic theory of the free energy (G) can help to understand and identify ferroelectric materials. This section presents the Landau-Devonshire theory of ferroelectrics, where in its simplest form, the theory deals with the phase transition from a parent nonpolar phase to a polar phase. For an exact representation, the polarisation vector $\vec{P}$ should be considered, but in order to explain the underlying concept more clearly, a more straightforward example is chosen, where the free energy is

expanded in terms of a single component of the polarization ($\vec{P} \rightarrow P$).
Leaving out external stimuli (e.g. electric field, mechanical stress), the free energy G of the crystal can be written as [11]:

$$G = \frac{1}{2}aP^2 + \frac{1}{4}bP^4 + \frac{1}{6}cP^6\,. \tag{2.1}$$

The coefficient a, b, and c are related to the symmetry of the crystals and could be either obtained through experimental measurement or be derived from *ab initio* calculation.
To find a stable state, G has to be minimized concerning the polarization P. For this, the first derivative $\frac{\partial G}{\partial P}$ must be equal to zero, and the second derivative $\frac{\partial^2 G}{\partial P^2}$ larger than zero:

$$\frac{\partial G}{\partial P} = aP + bP^3 + cP^5 = 0 \qquad \wedge \qquad \frac{\partial^2 G}{\partial P^2} = \frac{1}{\chi} = a + 3bP^2 + 5cP^4 > 0\,. \tag{2.2}$$

Above the phase transition, in the paraelectric state, the polarization becomes zero, all previous non-trivial minima ($P \neq 0$) have to vanish, and the second derivative becomes negative. Since $\frac{\partial^2 G}{\partial P^2}$ correlates to P^2 and P^4 the sign switch at a finite temperature T_0 has to happen in a. To account for this, a will be substituted by $a = a_0(T - T_0)$, where a_0 can only have positive values. In the applied theory, the other coefficients are temperature independent so that equ. (2.1) can be rewritten as:

$$G = \frac{1}{2}a_0(T - T_0)P^2 + \frac{1}{4}bP^4 + \frac{1}{6}cP^6\,. \tag{2.3}$$

For the following discussion, it has to be pointed out that c has only positive values since it is the coefficient of the highest order-term, and at $P \rightarrow \pm\infty$ negative values would create "false" minima. The coefficient b determines the nature of the phase transition and can be positive (second-order transition) or negative (first-order transition).

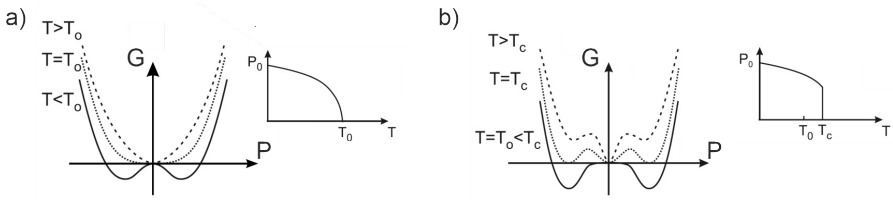

Figure 2.2.: Representation of the free energy for different temperatures as well as the spontaneous polarization $P_0(T)$ as a function of temperature. a) Second-order transition ferroelectric. b) First-order transition ferroelectric. In the temperature range between T_0 and T_C, two local minima exist in addition to the global minima at $P = 0$. Image source: [11].

Second-order transition

In the case of a positive b (and positive c), the highest order-term cP^6 brings no additional contribution and can be neglected, reducing equ. (2.3) to:

$$G = \frac{1}{2}a_0(T - T_0)P^2 + \frac{1}{4}bP^4\,. \tag{2.4}$$

The extrema of this equation are at:

$$\begin{aligned} \frac{\partial G}{\partial P} =& a_0(T - T_0)P + bP^3 = P(a_0(T - T_0) + bP^2) = 0 \\ \rightarrow P_1 =& 0 \qquad \rightarrow P_{2,3} = \pm\sqrt{-a_0(T - T_0)/b}\,. \end{aligned} \tag{2.5}$$

For $T \geq T_0$ the only real solution is $P_1 = 0$. At T_0 the polarization collapses and thus can be identified as the Curie temperature T_C. For $T < T_0$, the extrema have to be checked by the second derivation:

$$\begin{aligned} \frac{\partial^2 G}{\partial P^2} =& a_0(T - T_0) + 3bP^2 \overset{!}{>} 0 \\ \rightarrow \frac{\partial^2 G}{\partial P^2}(P_1) =& a_0(T - T_0) < 0 \qquad \rightarrow \frac{\partial^2 G}{\partial P^2}(P_{2,3}) = -2a_0(T - T_0) > 0\,. \end{aligned} \tag{2.6}$$

$P_{2,3}$ form two minima separated by the maximum at P_1 (see Fig. 2.2 a)).

First-order transition

For negative b values, the full equ. (2.3) has to be taken into account, such that five possible extrema arise:

$$\begin{aligned} \frac{\partial G}{\partial P} =& a_0(T - T_0)P - |b|P^3 + cP^5 = P(a_0(T - T_0) - |b|P^2 + cP^4) = 0 \\ \rightarrow P_1 =& 0 \qquad \rightarrow P^2_{2,3,4,5} = \frac{|b|}{2c} \pm \sqrt{\left(\frac{|b|}{2c}\right)^2 - a_0(T - T_0)/c}\,. \end{aligned} \tag{2.7}$$

Due to the additional contribution of $(|b|/2c)^2$ in the square root, a temperature higher than T_0 is needed to make $P^2_{2,3,4,5}$ irrational. In this case, T_0 is smaller than the Curie temperature T_C, and is known as *Weiss constant*. In the temperature range between T_0 and T_C meta-stable states exist (see Fig. 2.2 b)). During the phase transition upon heating or cooling, different meta-stable states could be occupied and thus lead to hysteresis behavior in the spontaneous polarisation.

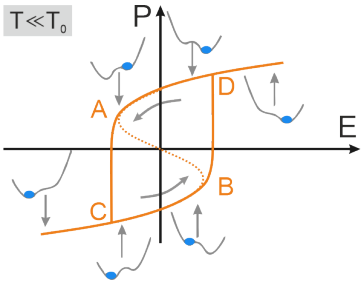

Figure 2.3: Polarization as a function of E below T_0. The sketches around the hysteresis show how the external electrical field bends the free energy. Following the P to E relation of equ. (2.9) strictly would result in the S-shaped path C-B-A-D, but the central part of the "S" corresponds to a free energy local maximum. Hence the path C-B-D-A is conventionally observed.

External electrical field

Ferroelectrics are defined by their reorientability of the dipole moments in an external electrical field. To add the contribution of an external electric field E to the free energy, an additional term has to be added to equ. (2.1):

$$G = \frac{1}{2}aP^2 + \frac{1}{4}bP^4 + \frac{1}{6}cP^6 - EP\,. \tag{2.8}$$

Due to the linear proportionality between the electrical field E and the polarisation P, the added term acts like a seesaw lowering or raising the free energy and thus is able to reduce the number of stable states at $T < T_0$ to one (see Fig. 2.3). An expression for the electric field E parallel to the polarization can be derived by the first derivation of equ. (2.8):

$$\frac{\partial G}{\partial P} = 0 \rightarrow E = aP + bP^3 + cP^5\,. \tag{2.9}$$

Plotting this equation as a function of P and switching the axes will result in an "S" shaped curve, where the central part corresponds to a free energy local maximum (see Fig. 2.3). To obtain the conventionally observed hysteresis loop, the central part has to be excluded, and vertical lines connect the top, and bottom portions of the "S" curve at the discontinuities.
In a real ferroelectric crystal, there are regions with the same magnitude of spontaneous polarization but are oriented in opposite directions, called domains. Applying an external electrical field switches the domains one after the other, creating a smooth transition at the discontinuities (see Fig. 2.1).

Ferroelectricity in HfO_2

Conventional ferroelectrics consist of at least three different elements and have two stable eccentric positions of an ion or a collective of ions in the unit cell forming the dipole moment. For oxide ferroelectrics a degree of covalency in chemical bonding has been postulated as a requirement for ferroelectricity [12]. A classical example is $BaTiO_3$, which has a Ti 3d-O 2p hybridization [13] and a phase transition at the Curie temperature T_C= 110 °C from the tetragonal into a cubic crystal structure [14]. Below T_C, the positively charged Ba^{2+} and Ti^{4+} shift along the c-axis relative to the negatively charged O^{2-}, forming a spontaneous polarization in the c-direction (see Fig. 2.4).
HfO_2 can also form a tetragonal crystal structure, but no symmetry is broken due to only having two elements. The ferroelectric phase of HfO_2 is orthorhombic (o), which has two different oxygen lattice places, one where oxygen has four bonds with Hf and another one with only three. The coordination (CN) of the Hf atoms in the o-phase is sevenfold. The oxygen with three bonds is stably displaced, forming the dipole moment.

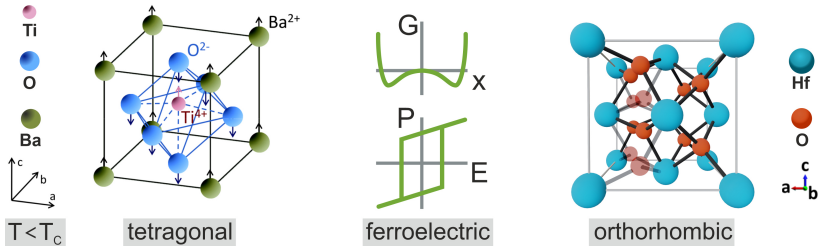

Figure 2.4.: (left) Crystal structure of tetragonal $BaTiO_3$: Below the Curie temperature the ferroelectric tetragonal structure is energetically favoured. The positively charged Ba^{2+} and Ti^{4+} ions shift upwards, and the negatively charged O^{2-} ions shift downwards, indicated by arrows. This leads to a slightly elongated c-axis breaking the inversion symmetry and creating a spontaneous polarization in the c-direction. Image source: [14]. (right) Crystal structure of orthorhombic HfO_2: In the ferroelectric orthorhombic phase, the oxygen atoms have lattice positions with 3 and 4 bonds to Hf, respectively. The inversion symmetry is broken by stable displacement of the O atoms with only three bonds. The shaded O ions represent the second stable position which is possible. Own representation. The crystal structure is taken from ref [15]

2.1.2. Stabilizing the ferroelectric phase in HfO_2

As bulk material at ambient pressure and room temperature, HfO_2 exhibits a monoclinic phase of space group $P2_1/c$, which undergoes upon heating a phase transition into a higher symmetry tetragonal phase of space group $P4_2/nmc$ at about 1700 °C [16]. Experimentally the crystallographic phase can be determined by grazing incident X-ray diffraction (GiXRD) (see sec. 3.1.2). The use of thin films and doping of SiO_2 has been found to stabilize the tetragonal phase also at room temperature [17–19]. Many deposition methods of thin-film HfO_2 produce an amorphous film and crystallization is realized by an additional annealing process. During the annealing, thermic energy is introduced into the system and depending on the free energy landscape, a particular crystal structure is adopted. Figure 2.5 a) depicts the free energy landscape of a doped HfO_2 thin films schematically, showing the tetragonal (t) and monoclinic (m) phase as two minima, separated by a kinetic barrier [20]. Considering phase transition kinetics, often an intermediate/metastable phase forms, lowering the transition barrier between two phases, which is generally discussed as the Ostwald step rule [21]. In the case of HfO_2, the ferroelectric orthorhombic (o) phase of space group $Pca2_1$ is the metastable phase lying between the monoclinic and tetragonal phases. Thus, a t↔m-phase transition undertakes first a t↔o-phase transition, followed by the o↔m-transition. For completeness, it is important to point out that in the low-energy phases (m and o), the Hf atoms have bonds to seven neighboring oxygen atoms, thus a coordination (CN) of 7, and the relatively higher energy phases, such as the tetragonal- and cubic-phases, have Hf atoms with a CN of 8 [20]. The first realization of HfO_2 in a stabilized orthorhombic phase was achieved by the use of thin films and doping with SiO_2 [1].

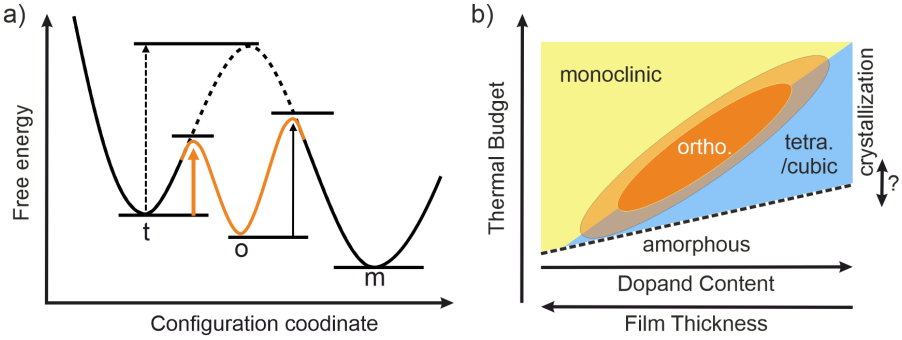

Figure 2.5.: a) Schematic of the free energy landscape of a doped HfO_2 thin film. The kinetic barrier height between the t- and m-phase is lowered through the intermediate o-state. Images from ref. [20] page 117. b) A qualitative model of the most critical process factors and their influence on the phase transitions of HfO_2. Image template: [9]

Factors stabilizing the orthorhombic phase can be classified as follows:

- Film thickness
- Strain and stress
- Doping
  - Isovalent doping
  - Aliovalent doping
- Oxygen vacancies V_O
  - "neutral" V_O
  - "charged" V_O
  - V_O-nitrogen complex

The overall effect of a reduced film thickness is stabilizing high-temperature phases at lower temperatures. The reasons for this are diverse and lie in the different effects introduced by thin layers. During deposition, thin films are typically processed at reduced temperatures than their bulk and single-crystal counterparts, leading to a higher defect concentration and reduced grain sizes. Defects can reduce the CN of the Hf^{4+} ions, stabilizing the higher energy phases [22].
Due to reduced grain sizes, the relative volume fraction of grain to grain boundaries increases. At the grain boundaries, defects tend to accumulate. The small grain sizes in ferroelectric HfO_2 make it likely that grain and domain boundaries overlap [23, 24].
Thin films also reduce the fraction between the layer and the interfaces to the electrodes/substrate. At the interfaces, layers can form that do not possess the same properties as the bulk, e.g., due to lattice mismatches, which can introduce strain. Additional stress can occur if the coefficients of thermal expansion differ between the film and the substrate and an amorphous film is exposed to a higher temperature for crystallization. In addition to the thickness, temperature, electrode material, and doping have a decisive role. Figure 2.5 b) depicts a qualitative model of the most critical process factors and their impact on the phase transitions of HfO_2 [9].

Oxygen vacancies and their configurations

Oxygen vacancies are a form of point defects that can exist in any metal oxide. They may be introduced to the lattice during the manufacturing process or by electrical field cycling when the electric field weakens bonds. Applications utilizing this effect are, e.g., resistive random-access memories (RRAMs) [25]. Following are some ways oxygen vacancies can form:

- During the production process and incorporated into the crystal.
- During the production process of a doped film, where the V_O ionically compensates the charge introduced by the dopant (ionic compensation).
- During electric field cycling.

Depending on the preparation and treatment of the HfO_2 thin films, oxygen vacancies can be introduced to the system differently and can be located or distributed in the lattice in many different ways.

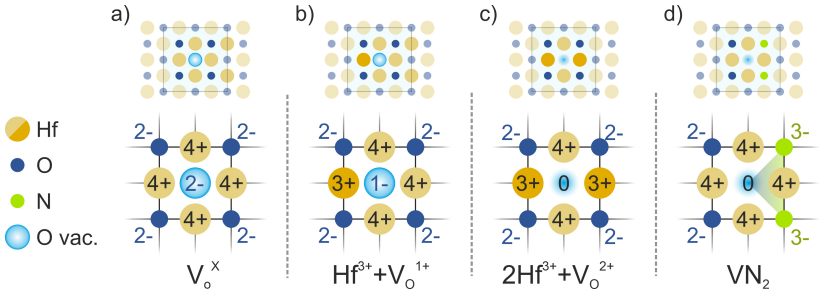

Figure 2.6.: a)-d) represents different configurations of an oxygen vacancy (center) in the lattice. The number in the center (2-, 1-, 0) counts the electrons at the V_O side. a) *Neutral* oxygen vacancy $V_O^{\times}$, containing two electrodes. b) & c) *Charged* oxygen vacancy V_O^{1+} (V_O^{2+}) in combination with (2)Hf^{3+} ion(s). d) Vacancy-nitrogen complex VN_2. Two N ions substitute oxygen atoms, preferred next to a vacancy.

The Kröger-Vink notation can be used to formalize how the vacancies and also dopants are incorporated into the lattice of a crystal structure. For the syntax three parameters are used: Q_S^C. Q corresponds to the species, e.g., atoms or vacancies V. S indicates the lattice site that the species occupies, and C corresponds to the electronic charge of the species relative to the site it occupies. A relative positive charge is indicated by bullet points $\bullet$, a relative negative charge is indicated by the apostrophe ' and a null charge is marked by a times symbol $\times$. A vacancy at an O^{2-} site containing two electrons thus would be written as $V_O^{\times}$ and a dopant like La^{3+} at the Hf^{4+} lattice site as La_{Hf}'.
Creating an oxygen vacancy by removing a neutral O from the crystal lattice leaves two remaining electrons at the oxygen site. For the electrons at the vacancy position, there are several possibilities to be located or distributed in the lattice (see Fig. 2.6):

a) **Neutral vacancy:**

$$\boxed{HfO_2 \rightarrow Hf_{Hf}^{\times} + O_O^{\times} + V_O^{\times} + \tfrac{1}{2}\ O_2}$$

If an oxygen vacancy has two electrons, it is considered neutral $V_O^{\times}$.

b) **Positively charged vacancy:**

$$\boxed{HfO_2 \rightarrow Hf_{Hf}' + O_O^{\times} + V_O^{\bullet} + \tfrac{1}{2}\ O_2}$$

In the constellation of one Hf^{3+} ion next to V_O and one remaining electron at the vacancy site, the vacancy is considered as positively charged V_O^{1+}.

c) **Double positively charged vacancy:**

$$\boxed{2HfO_2 \rightarrow 2Hf_{Hf}' + 3O_O^{\times} + V_O^{\bullet\bullet} + \tfrac{1}{2}\ O_2}$$

Two Hf^{3+} ions next to V_O can leave the vacancy site without electrons and thus creates a double positively charged vacancy V_O^{2+}. In undoped HfO_2, this configuration should be the most stable, but also V_O^{1+} is experimentally observed [26].

d) **Vacancy-N_2-complex:**

$$2HfO_2 + N_2 \rightarrow 2Hf_{Hf}^{\times} + O_O^{\times} + V_O^{\bullet\bullet} + 2N_O' + \frac{1}{2}\,O_2 + O_2$$

Doping HfO_2 with the anion N^{3-} replaces oxygen at their lattice side. Theoretical models [27–29] found that the energetically most favorable incorporation of N is at the two oxygen positions nearest to a vacancy. Incorporating two nitrogen atoms will capture both electrons from the oxygen vacancy and form a closed shell VN_2 complex [27, 30, 31]. Locally, the valencies of the oxygen vacancy and the N atoms combined amount to $(VN_2)^{-8}$, and hafnium remains in a Hf^{4+} state.

Effect of capping electrodes on the ferroelectricity of HfO_2

In most fabrications of ferroelectric HfO_2 thin films, the HfO_2 is first capped by an electrode before the needed annealing step is applied. The top electrode seems to add additional strain and stress. This clamping effect by a top electrode seems vital to suppress the formation of the nonpolar monoclinic phase [22, 32]. HfO_2 films with a robust ferroelectric response but without capping are possible and have, for example, been realized by additional Al interlayers inside the HfO_2 film, which add the needed strain, and stress [33].

Differences in the electrode material

In addition to the clamping effect, electrodes can introduce additional vacancies or other elements into the HfO_2 layer during the annealing process. At higher temperatures, atoms at the interfaces are mobile and depending on the electrode material, an exchange of elements is possible. Used electrode materials are, e.g., TiN, TaN, Pt, or RuO_2. In the case of TiN or TaN, O from the HfO_2 and N from the electrode material can exchange and lead to the diffusion of N into HfO_2, and the formation of Ti-O-N or Ta-O-N at the interfaces [34, 35]. During this exchange, new O vacancies can be created at the HfO_2 side. Oxides as electrode material can act as an oxygen vacancy sink, reducing the V_O concentration in HfO_2. For example, for RuO_2, this leads to a degradation of the ferroelectric phase, showing less contribution of the ferroelectric phase than found in a TiN reference samples [36].

Vacancy states in HfO_2

HfO_2 as a semiconductor has a bandgap separating the valence band (VB) and conducting band (CB), where the Fermi-level lays in the bandgap. HfO_2 in the ferroelectric orthorhombic (o) phase has a bandgap of around 5.8 eV [37].
In an intrinsic semiconductor (with no doping), the Fermi level lies at the middle of the energy bandgap (at T=0 K), assuming the same density of states at the CB and VB. In an extrinsic semiconductor (with doping), the Fermi level shifts depending on the dopant type. With n-type dopants, additional electrons are added to the system, shifting the Fermi level towards the CB. P-type doping does the opposite, reducing the number of electrons and thus shifting the Fermi level towards the VB.

O vacancies in HfO_2 act like n-type dopants, creating new states close to the CB and shifting the Fermi level towards it. Figure 2.7 shows the calculated energy level of differently charged vacancies and the VN_2-complex of cubic HfO_2. With increasing vacancy positive charge, the levels raises, due to an outward relaxation of the Hf ions adjacent to the vacancy [29]. For the VN_2-complex no gap state exist, because the level previously formed by the vacancy moved into the CB, due to repulsion by the N ions. The electrons left by the oxygen vacancy are transferred to the nitrogen ions. In addition, N introduces filled N 2p states above the oxide valence band edge [38], an thus HfO_2:N can have a reduced band gap compared to HfO_2.

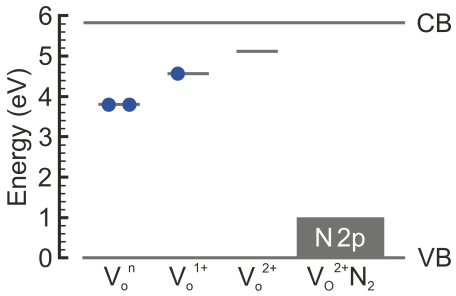

Figure 2.7: Energy levels of (charged) vacancies and VN_2 complex. N introduces filled N 2p states above the oxide valence band edge [38]. Image based on ref. [29].

Isovalent and Aliovalent doping

The stabilizing effect of doping relies on the dopant concentration and the choice of dopant material since its size and valency determine how the dopant can be incorporated into the lattice and how it affects the properties of the HfO_2 films. In stoichiometric HfO_2, the Hf and O atoms have valencies of 4+ and 2-, respectively. If the used doping element has the same valency, such doping is called *isovalent* otherwise *aliovalent*. Some commonly used cation dopants for HfO_2 are Si^{4+}, Zr^{4+}, La^{3+}, and Gd^{3+}. For anion dopants, N^{3-} is known to be able to stabilize the o-phase [39]. Due to similar effects, in a broader sense, oxygen vacancies can be counted as a form of *anion doping* as well.
Dopants influence the local environment in the lattice by distortion and changing the charge. Figure 2.6 a) and b) shows a simplified schematic of these influences:

a) **Lattice distortion by doping:**

   Dopants with different ionic radii can influence the bond lengths and distort the lattice. Zr^{4+} as an example, has a slightly bigger ionic radius than Hf^{4+} ($\approx$2%) [40] and thus increases the volume of the (Hf,Zr)O_2 unit cell with increasing Zr^{4+} substitution.

In this thesis, in addition to HfO_2 thin films also $Hf_{0.5}Zr_{0.5}O_2$ (HZO) thin films are studied. For the description of ferroelectric properties in HZO thin films, HZO can be considered as Zr doped HfO_2. Figure 2.8 c) depicts a schematic diagram of the behavior of $Hf_{1-x}Zr_xO_2$ films for various film compositions and thicknesses, showing ferroelectric properties for Zr to Hf ratios around 50% across a larger thickness range.

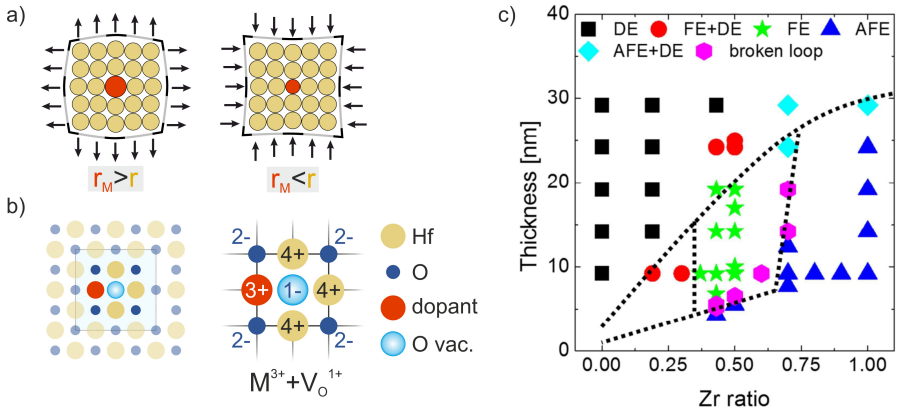

Figure 2.8.: a) Schematic representation of the lattice distortion by doping with bigger/smaller radius than the solvent. b) Aliovalent doping with trivalent cation M^{3+}: A Hf^{4+} is replaced and a *charged* oxygen vacancy V_O^{1+} is created. One electron remains at the V_O side. c) Schematic diagram of the dielectric behavior of $Hf_{1-x}Zr_xO_2$ films for various film compositions and thicknesses. The films were deposited using atomic layer deposition (ALD). The abbreviations in the image stand for **DE:** dielectric, **FE:** ferroelectric, and **AFE:** antiferroelectric-like. Diagram is taken from ref. [41].

b) **Changing the charge by aliovalent doping:**

In addition to the effect of different ionic radii, aliovalent dopants will also change the charge. The use of trivalency cation to substitute the Hf^{4+} atoms will result in a charge deficiency, which may be compensated by the formation of an oxygen vacancy next to the cation (ionic compensation). The local CN is reduced. In the constellation where one electron remains at the lattice position of the oxygen vacancy, the vacancy side is considered positively charged. This example with the trivalency cation M can be noted in the Kröger-Vink notation as:

$$HfO_2 + M \rightarrow M_{Hf}' + O_O^{\times} + V_O^{\bullet} + Hf + \tfrac{1}{2}\ O_2$$

Schottky contact

Two materials in contact share the same Fermi energy in thermal equilibrium. Since two materials in general exhibit different vacuum work functions, this results in a potential step at the vacuum levels accompanied by a charge transfer at the interface. A Schottky contact is formed by bringing a semiconductor in contact with a metal. At the interface, the bands of the semiconductor bend up or down, called band bending, depending on the difference in the work functions and the charge density at the interface. Figure 2.9 shows a schematic representation of the Schottky contact for an n-type semiconductor and a metal with larger and smaller work functions ϕ_M compared to the work function ϕ_S of the semiconductor. The n-type semiconductor contains impurity states close to the

conduction band minimum (CBM), which shifts the Fermi level of the semiconductor towards its CBM. For an alignment of the Fermi levels in the case $\phi_M > \phi_S$, the bands of the semiconductor are bent downwards, resulting in the formation of a depleted space-charge region called the Schottky barrier. The extension d_n of this barrier typically does not exceed one nanometer and can be calculated by [14]:

$$d_n = \left(\frac{2\epsilon\epsilon_0}{n_D}(\phi_M - \phi_S)\right)^{1/2}. \tag{2.10}$$

Here ϵ is the permittivity of the semiconductor, ϵ_0 is the vacuum permittivity, and n_D is the density of the impurities. A higher impurity concentration at the interface reduces the extension of the barrier since d_n is inverse proportional to n_D.
For the other case with $\phi_M < \phi_S$, the bands bend upwards. Depending on the amount of bending at the interface, the Fermi level may lay inside the conduction band, resulting in an accumulation of electrons on the semiconductor site.

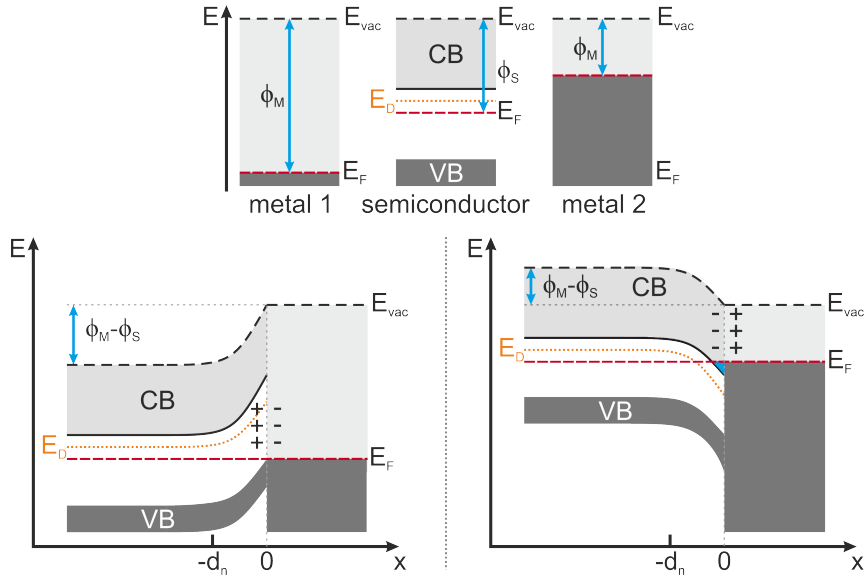

Figure 2.9.: Schematic representation of a Schottky contact in thermal equilibrium. The Fermi Level in the semiconductor lays between the conduction band (CB) and the valence band (VB). (left) Metal 1 with $\phi_M > \phi_S$; (right) Metal 2 with $\phi_M < \phi_S$; The band bending is defined by the difference in the work functions.

2.1.3. Ferroelectricity under switching electric field

The ferroelectric HfO_2 thin-films discussed in this thesis have a capacitor structure consisting of conductive electrodes encapsulating the isolating ferroelectric layer. In thermal equilibrium, the Fermi level is aligned across all layers. In the case that the work functions of the top and bottom electrode differ, an internal bias filed across the ferroelectric layer can emerge (see Fig. 2.10 a)). Contacting the capacitor structure enables the study of the ferroelectric response by applying a voltage and measuring the resulting current $I(E)$ (see Fig. 2.10 b)). A detailed description of the method used to measure the ferroelectric response can be found in section 3.1.2 *Electrical field switching*. Integrating the current measurements $I(E)$ creates the polarisation hysteresis curves $P(E)$ (see Fig. 2.11). If an internal bias field exists, the measured hysteresis curves will show a shift since the internal bias field eases the switching in one direction and impedes it in the other. The value of the remanent polarization P_r at zero fields is used to indicate and compare the strength of a specific ferroelectric material. Most often the negative and positive values of P_r are added up to form the double remanent polarisation $2P_r$. Over electrical field cycling the ferroelectric capacitor transitions through different $2P_r$ values. Figure 2.11 shows the behavior of the double remanent polarisation upon the number of cycles n and examples of the hysteresis from the pristine, after wake-up, and after fatigue measurement. The remanent polarization changes in two phases, starting with the wake-up phase, which is characterized by a continuous increase of $2P_r$. After the maximum value of $2P_r$ is reached ($n \approx 10^5$), the fatigue phase begins, where the $2P_r$ steadily decreases till a hard breakdown (here $n \approx 10^8$) with a significant increase in leakage current [42, 43].
Possible reasons for the wake-up phase are seen in the pinning of domains at vacancies in their pristine polarization directions and in local internal bias field, caused by trapped

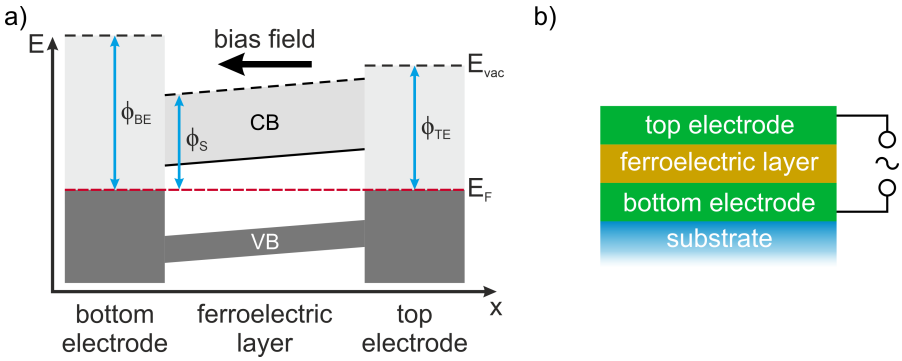

Figure 2.10.: Schematic representation of the capacitor structure. The isolating ferroelectric layer is encapsulated by conductive electrodes forming a capacitor. a) Band structure: Internal bias fields emerge for different work functions between the bottom and top electrode. b) An electric field can be applied to the ferroelectric layer using a voltage.

electrons at the V_O site if those are accumulated at the interfacial layer between the ferroelectric layer and electrodes. Another possible location for higher V_O density is at domain walls. The local bias fields reduce the electric field required for switching for some domains while decreasing it for oppositely oriented domains.
A sign of those trapped charges and pinned domains can be seen in the pristine hysteresis loops, where the current-hysteresis has a "split up" of the switching distribution, and the polarisation-hysteresis is pinched. During electric field cycling, charges can redistribute and reduce the local bias fields.
With increasing number of cycles, not only charges are altered but also oxygen vacancies can migrate to interfaces, including domain walls. The accumulation of vacancies restricts domain wall motion [44, 45]. Such pinned domains no longer contribute to the measured responses, explaining the decrease in the $2P_r$ value during fatigue. Eventually, the accumulated vacancies can form filaments through the ferroelectric layer, leading to an increased leakage current and hard breakdown.

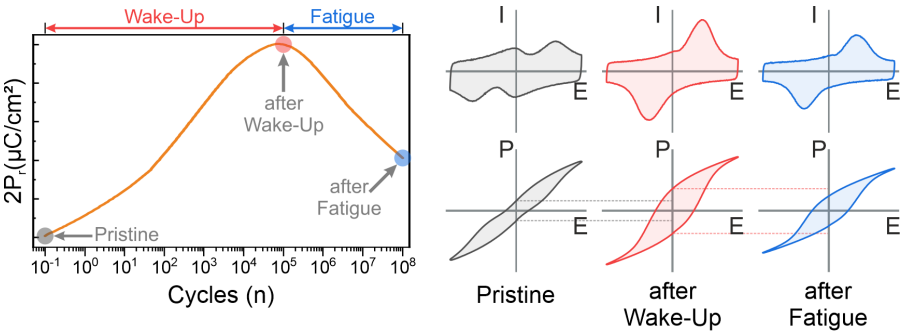

Figure 2.11.: Double remanent polarization of a ferroelectric HfO_2 capacitor over the number of electric field cycles. On the right are the hysteresis added fitting to the marked points.

2.1.4. Ferroelectric HfO_2-based applications

Using ferroelectric HfO_2-based materials for non-volatile memories, the information in the form of bits is stored in the polarisation direction. For example, such a bit can be realized in ferroelectric field-effect transistors (FeFET). Figure 2.12 depicts the schematic structure of a FeFET as well as the ON and OFF state. In this example, the FeFET consists of a p-type semiconductor channel with electrodes at either end, called source and drain. The gate is used to control the flow of the current in the channel. Applying a voltage to the gate alters the conductivity between the source and the drain. With a ferroelectric as the gate dielectric, the electrical field persists, storing the transistor's state (on or off) even in the absence of the applied voltage. The information is read out using a source-drain voltage, where the state "current" or "no current" correspond to the polarization state and can be seen as 1 and 0, respectively.

The quality of memory devices can be evaluated be the characteristics retention and fatigue. Retention is the ability to maintain the written state over a certain time period. In ferroelectric HfO_2 the so-called imprint is the dominating phenomenon influencing retention. Imprint is the tendency of a ferroelectric to stabilize the state it is stored in, which leads to a loss of retention of the opposite state [46]. Generally, the imprint effect is associated with charge trapping at oxygen vacancies. For non-volatile memories, the retention should exceed ten years.
As illustrated in the previous section, fatigue describes the decrease of the ferroelectric properties, which also reduces the difference between the 1 and 0 states. If the difference falls below a certain limit, an accurate device operation becomes impossible. For this limit, the expression endurance is used.

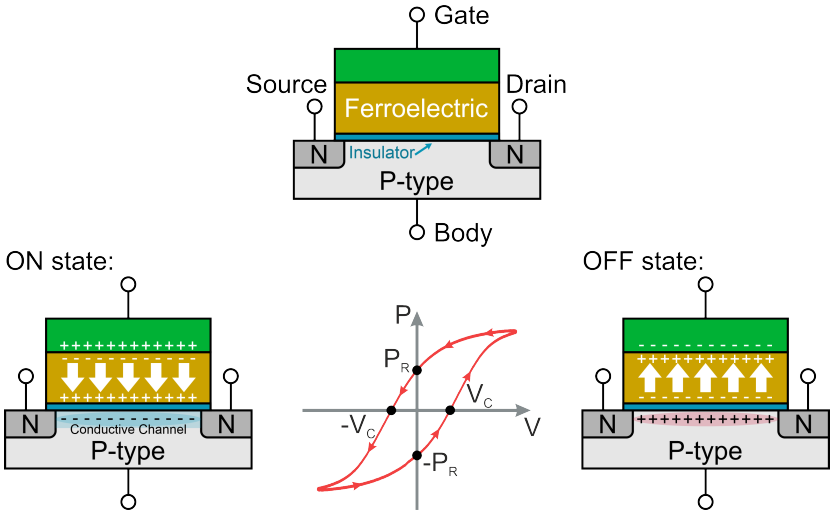

Figure 2.12.: Schematic structure of a ferroelectric field-effect transistors (FeFET). The gate voltage controls the polarization (white arrows) of the ferroelectric layer. A polarisation towards the p-type channel increases its conductivity enabling a current between source and drain (ON state). An opposite polarisation decreases the conductivity hindering a current flow.

2.2. Photoelectron spectroscopy

For this thesis, photoelectron spectroscopy with high-energy x-rays is the essential method that is based on the photoelectric effect and can element-selectively measure many properties of matter. The use of high photon-energies is crucial for the conducted experiments, bringing many benefits but complicating the experimental execution. In the following sections, the theoretical aspects required to understand the photoelectric effect will be described, as well as the benefits high energy x-rays bring and how a Hard X-ray Photoelectron Spectroscopy (HAXPES) experiment is realized.

The photoelectric effect describes the interaction between the electrons of matter and absorbed light quanta (photons). Depending on the photon's energy ($h\nu$), the electrons can either be excited into an unoccupied state (photon absorption) or the material can be ionized (photoelectric effect). During the ionization, photoelectrons are emitted, whose intensity is studied as a function of the kinetic energy E_{kin} via photoelectron spectroscopy.

2.2.1. Three step model of photoemission

Photoemission can be phenomenologically described in a three-step model (Excitation, Propagation, and Transmission) [47]. Due to the division of the underlying physical mechanism into three consecutive events, this model is a semiclassical approach to the photoemission process. The division allows for an independent treatment of each step using a single-particle picture, but it neglects the coherence of the total process and the possible importance of many-body effects. To include these effects and use a non-approximative model, the photoemission process has to be seen as a one-step event. The theories behind the one-step photoemission can be used to calculate spectra that can be compared with experimental ones, but such calculation requires considerable computational effort, which makes it impractical for general usage. The simplified approach of the three-step model is usually more suitable for a quantitative interpretation of the experimental results and will be briefly presented in the following.

I. Excitation In the first step, a photon is absorbed and transmits its entire energy ($h\nu$) to an electron of an occupied state which is excited into an empty state above the vacuum level within the electronic band structure of the solid. Those states are described as initial **i** and final **f** states in the single-particle picture. The quantum mechanical description of this process is discussed in more detail in sec. 2.2.2.
II. Propagation to the surface The excited electron propagates through the solid towards the surface. During this process, inelastic scattering events can occur, changing the electron's kinetic energy. For photoelectron spectroscopy, not scattered electrons or ones that were elastically scattered are most relevant. The scattering processes limit the mean free path λ of the photoelectrons traveling within the solid and thus the probing depth. An important fact is that λ depends on the kinetic energy of the photoelectrons [48] (see sec. 2.2.4). In this work, the photon energy of 6 keV is used, enabling the study of several nm thick films.

III. Transmission and escape If a photoelectron reaches the surface and still has enough energy to overcome the material-specific work function ϕ, it leaves the solid into the vacuum. In this case, the energy relation for not scattered/elastically scattered photoelectrons is [14]:

$$h\nu = E_{\text{bin}} + \phi + E_{\text{kin}} \,. \tag{2.11}$$

Here E_{bin} represents the binding energy, which is defined as the energy difference between the initial occupied state and the Fermi-level E_{F}, and E_{kin} is the kinetic energy of the electron outside the solid.

2.2.2. Quantum mechanical description of the excitation process

Quantum mechanically, the excitation process can be described as a perturbation of the wave function of an electronic N particle system (initial state) by the electric field of a photon. After the photoelectron is excited, the N particle system transforms into an N-1 particle system (final state), with the creation of a core hole and the occupation of the Nth electron in a (previously) unoccupied state above the Fermi-level E_{F}. To accurately describe the excitation process in a solid, the many-body Hamiltonian H has to be solved, determining all initial and final states $\Phi_{\text{i,f}}$. Since this Hamiltonian contains all interactions of all particles, a general analytic solution can not be obtained. However, the problem can be simplified with some approximations.
The photoemission process is assumed as instantaneous (sudden approximation), allowing to neglect all other interactions in the solid, which are weaker and much slower in comparison. As a result, the many-body Hamiltonian can be reduced to the single-particle Hamiltonian. In addition, the incoming light can often be treated in the electric dipole approximation, as long as the wavelength of the electromagnetic radiation λ is much larger than the typical size of an atom. Both approximations together allow for the treatment with established perturbation theory [49], leading to the following form of Fermi's golden rule:

$$W \propto |\langle \Phi_{\text{f}} | \, \mathbf{T} \, | \Phi_{\text{i}} \rangle|^2 \cdot \delta(E_{\text{f}} - E_{\text{i}} - E_{\gamma}) \,. \tag{2.12}$$

W describes the probability of an electron's transition from a ground state Φ_{i} to an excited state Φ_{f}. The dipole operator $\mathbf{T}$ describes the electronic dipole transition. The energy conservation is ensured by the δ function, only allowing transitions where the photon energy E_{γ} matches the energy difference of the inital and final state. Besides the energetic constraints, solutions of equ. (2.12) are also subject to the dipole selection rules [49]. Those only allow transitions where the difference in the quantum numbers for initial and final stats are

$$\Delta J = 0, \pm 1 \quad \Delta M_J = 0, \pm 1 \quad \Delta S = 0 \,. \tag{2.13}$$

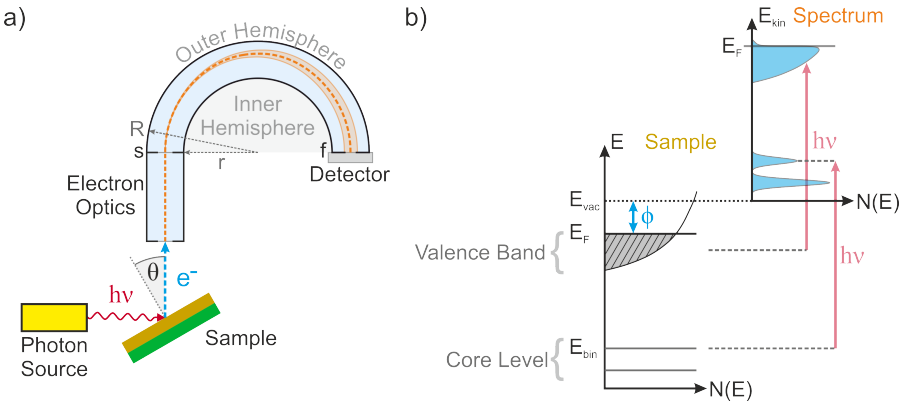

Figure 2.13.: a) Sketch of a photoemission experiment. Photons with the energy $h\nu$ irradiate the sample's surface, exciting photoelectrons. The analyzer setup studies the intensity depending on the kinetic energy. s and f are the entrance and exit slits of the 180° hemispherical analyzer, respectively. The angle θ defines the depth sensitivity (see sec. 2.2.4). b) Schematic representation of the electronic structure of a solid and the resulting spectra $I(E_{\mathrm{kin}})$ in the excitation process of a bound electron by a photon to a state above the vacuum level. The electronic structure consists of the localized core levels as well as the dispersed valence band. The electron density is reflected in the spectrum creating sharp peaks for the core level electrons and an energetically broadened feature for the valence electrons. Own image, adapted from ref. [47].

Here J is the total angular momentum quantum number. M_J is the projection of the total angular momentum and S is the spin. The selection rules (2.13) are a direct consequence of the photon spin ($S = 1$) coupled to the initial state in the excitation process. The energy selectivity shown in equ. (2.12) combined with unique binding energies in each element makes the photoelectron effect ideal for studying the composition and chemistry of solids and their surfaces.

Obtaining photoelectron spectra

The general experiment to obtain photoelectron spectra consists of a photon source, the sample, and an analyzer setup (e.g., a 180° hemispherical analyzer). The photons irradiate the sample's surface, generating photoelectrons that radiate in all spatial directions. A segment of the radiated electrons at the angle θ reaches the analyzer, which is focused by the electron optics to the entrance slit of the electrostatic 180° hemispherical analyzer (see Fig. 2.13 a)). The analyzer consists of an inner and outer metallic hemisphere of radius R and r, concentrically arranged. A potential difference ΔV applied between them bents the trajectory of the incoming electrons such that the electrons are "dispersed" as a function of their kinetic energy. Entering from the entrance slit s, only electrons with well-defined kinetic energy will have a trajectory leading to the exit slit

f and contribute to the measured intensity at the detector. This energy is the so-called pass energy E_{pass} and is kept constant during the measurement. The choice of the pass energy significantly influences the energy resolution of the measurement. Smaller E_{pass} increases the overall energy resolution ΔE of the analyzer and reduces the number of detected electrons. Thus the higher resolution comes at the expense of signal intensity. In order to scan over different kinetic energies, the electron optics are also used to retard (or accelerate) the velocity of the electrons so that their kinetic energy after passing through the transfer lenses matches E_{pass}. Figure 2.13 b) shows the excitation process of a bound electron by a photon to a state above the vacuum level. The energy difference between the Fermi level E_{F} and the vaccum level E_{vac} is the work function ϕ. Detecting the photoelectrons as a function of their kinetic energy E_{kin} results in a photoelectron spectrum, which is element selective since the electronic structure of the sample is determined by the involved elements and the chemical composition. Electrons from a core level form a sharp peak structure due to their localization, whereas the valence band has strong dispersion and is energetically broadened in the spectrum.

Spin-orbit coupling

An energetically deep-lying core-level has a fully occupied electron shell, and thus the *total orbital momentum* L of the electrons is $L = 0$. During the excitation process, a photo hole is created at the core-level, enabling a single particle description so that the spin (s) and orbital moment (l) of a single electron is used. In the excited state, s and l can couple, giving rise to a doublet with two possible states and different binding energies [50] in the spectra, except for the **s** core-levels, where $l = 0$. These doublet states are characterized by the total quantum number $j = l \pm s$. In addition to the binding energies, the resulting double-peak structure will have different peak areas, respectively, based on the degeneracy of each spin state $(2j + 1)$. The area ratio A of these doublet pairs is given by

$$\frac{A_{j=l-s}}{A_{j=l+s}} = \frac{2(l - 1/2) + 1}{2(l + 1/2) + 1} = \frac{l}{l + 1}\,. \tag{2.14}$$

As an example, using this equation for the p electrons ($l = 1$) results in an area ratio of 1:2 between $p_{1/2}$ and $p_{3/2}$. Table 2.1 lists all j-values and area ratios for the subshells.

Subshell	j-values	Area Ratio
s	1/2	n/a
p	1/2 3/2	1:2
d	3/2 5/2	2:3
f	5/2 7/2	3:4

Table 2.1.: Relative areas of the doublet pairs of the respective subshell, calculated by equ. (2.14).

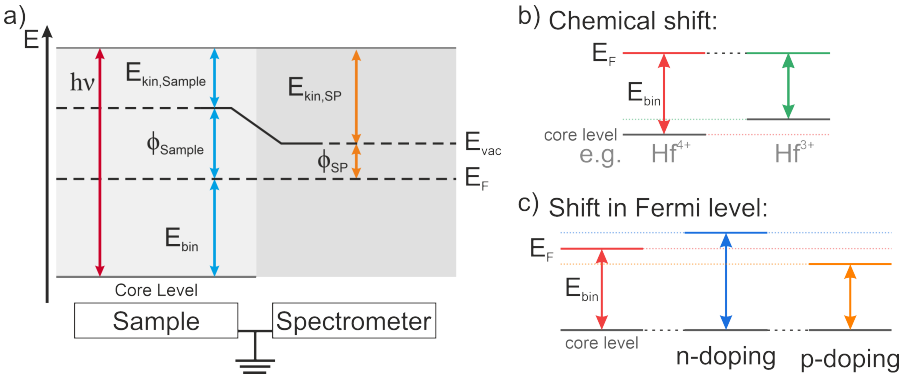

Figure 2.14.: a) Schematic of the photoemission measurement process. A bound electron from the sample is excited to a state above the vacuum level by a photon. The energy relation of equ. (2.11) is depicted by red and blue arrows. Due to an ohmic contact, the Fermi level of the sample and spectrometer is even, enabling the determination of the binding energy in relation to the Fermi level E_F (see equ. (2.17)). Schematic representation of binding energy shifts: a) *Chemical Shift* Changes in the core level due to chemical environment; b) Changes in the Fermi level due to doping.

Binding energy and shifts

With the photon energy used in the photoemission experiment, the kinetic energy of a spectrum changes. The Fermi level is used as a reference to make spectra comparable and determine the binding energy E_{bin}. Figure 2.14 a) shows a schematic of the energy relations for a photoemission measurement, where a spectrometer detects the photoelectron, e.g., as depicted in Figure 2.13 a). Due to an ohmic contact between sample and spectrometer (SP), the Fermi level is even so that the sum of each kinetic energy and work function is equal:

$$\phi_{\text{Sample}} + E_{\text{kin, Sample}} = \phi_{\text{SP}} + E_{\text{kin, SP}}. \tag{2.15}$$

The binding energy is defined by the Fermi-level E_F, such that E_{bin} at E_F equals zero. Using this information in equ. (2.11) we get:

$$h\nu = \phi + E_{\text{kin,F}} \Leftrightarrow E_{\text{kin,F}} = h\nu - \phi\,. \tag{2.16}$$

This definition can again be used in equ. (2.11) to get the binding energy E_{bin}:

$$E_{\text{bin}} = h\nu - \phi - E_{\text{kin}} = E_{\text{kin,F}} - E_{\text{kin}}\,. \tag{2.17}$$

Photoelectron spectra using E_{bin} are sensitive to changes in the binding energy of the core level as well as changes of the Fermi level. The changes in the core level arise due to changes in the chemical environment (*Chemical Shift*) and in semiconductors/insulators

the Fermi level can change due to chemical doping (*Fermi level shift*) (see Fig. 2.14). An example of a change in the chemical environment can be charged vacancy in the HfO_2 lattice, changing the valency of the neighboring Hf ions from 4+ to 3+ (see sec. 2.1.2). The E_{bin} for Hf^{3+} is lower than for Hf^{4+} leading to an shift in the spectra, which is different for each element and core level.
If the electron density in a solid is changed, for example, by doping (e.g., oxygen vacancies), the position of the Fermi level changes. In semiconductors/insulators, doping can create gap states which also change the Fermi level. Since the Fermi level is the reference point, all core levels of any element in the material shift similarly.
The example of the charged vacancy in HfO_2 shows that the separation into the two types of E_{bin} shifts is a simplified model, and both types of shifts often appear in combination.

2.2.3. Spectral features

Apart from the primary core level excitation, core level photoelectron spectra generally consist of an inelastic scattering background and secondary excitations.This section describes possible spectral features for in-depth analysis and interpretation of the photoelectron spectra.

Shake-up features and plasmon excitation

The excitation of a photoelectron leaves the remaining atom in a highly excited state. The description of this state by a simple single particle binding energy E_{bin} is a simplification, which in practice often fails. In general, the excited state of the ion together with the photoelectron has to be described by a set of excited states with different and excitation energies and probabilities. In particular low energy excitations at localized states near the Fermi energy are of importance and may be observed as satellites of the single particle excitation in the core level spectra. This photoelectron will appear at higher energies of the binding energy scale as a shake-up peak. The energy difference between the main peak and the shake-up peak is element-specific. For any comparison of peak intensities, the main and shake-up peaks have to be combined.
Another peak structures possible at higher binding energies than the main peak are plasmons. For conductive materials, a photoelectron traveling to the surface may lose energy by inelastic scattering with the conduction electrons in well-defined energy quanta E_p arising from group oscillations of the conduction electrons [51]. The energy loss E_p for the photoelectron is equal for all elements and core levels in the same solid and can be calculated by:

$$E_p = \hbar\omega_p = \hbar\sqrt{\frac{ne^2}{m\epsilon_0}}\,. \tag{2.18}$$

Here $\hbar$=h/(2π) is the reduced Planck constant, and ω_p is the plasmon frequency. The defining parameters of this frequency are the conduction electron density n, the electron charge e, the mass of an electron m, and the dielectric constant ϵ_0.

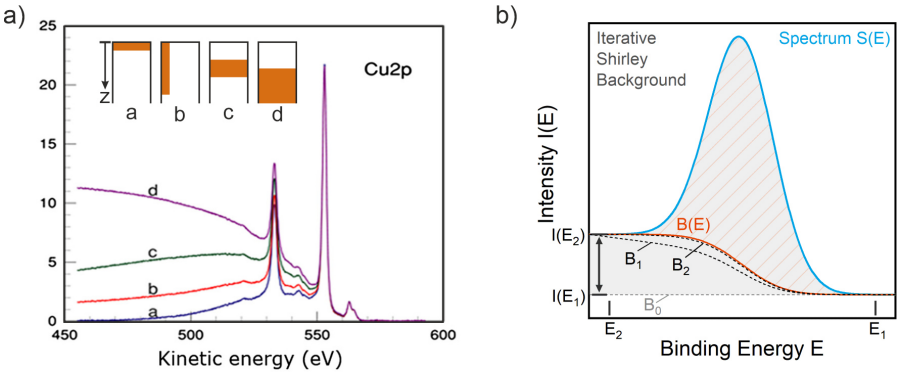

Figure 2.15.: a) Comparison of different backgrounds in a model system from Cu atoms with varying distributions of concentration in an Au matrix. Image source: [52]. b) Schematic of the Iterative Shirley background method. Own representation.

Secondary electron background

During the photoemission process, the excited electrons propagate through the solid, with the probability of inelastic scattering. Inelastically scattered electrons transmit/loose part of their kinetic energy and create a background intensity in the region of higher binding energies for every photoemission feature. This background must be separated from the measured spectrum since only the unscattered photoelectrons carry the information on the electronic structure directly.
The location of the atoms in the studied layer system emitting the photoelectron, the studied element, and the photon energy define the shape of the background [52]. Figure 2.15 a) shows Cu 2p spectra of a model system where Cu atoms are differently distributed in an Au matrix, giving rise to different backgrounds. In the small binding energy range around the core-level peaks, the backgrounds are similar and are defined by an increase proportional to the signal intensity. At lower kinetic energies, in all presented scenarios, the background decays. The scenario **d** of a bulk layer covered by a thin film has the longest ranging background (the decay is not visible in Fig. 2.15 a)). In the simplest case of a thin film at the surface, the background at lower kinetic energy can be described by an exponential decay. There are various methods to deal with the background around the peaks [53]. For the simplest cases, modelling a linear background is sufficient. The main method used in this thesis is the *Iterative Shirley background* [54], which forms a step-like function where the step is aligned to the peak maximum. The idea behind the Shirley background is that the intensity of the inelastically scattered electrons is proportional to the signal intensity of the unscattered photoelectrons.

Figure 2.15 b) depicts how this method is applied [53]. The first step starts with the selection of the start point (E_1) and end point (E_2) of the background, followed by the removal of a linear flat background (B_0) so that the intensity at $E_1 = 0$.

The iteration can be described in two steps:

1. Integration over the spectra $S(E)$, which is subtracted by B_0 and the previous iteration of the background $B_{n-1}(E)$.

2. Normalisation to the intensity at the end point $I(E_2)$.

The integration is performed in such a way that each binding energy E is assigned to the integral between E_1 and E. Without normalization, the curve formed in this way has at E_2 a value that corresponds to the integration over the complete energy range. The iteration process can formally be expressed as:

$$B_n(E) = k_n \int_{E_1}^{E} dE' [S(E') - B_0 - B_{n-1}(E')] \,, \tag{2.19}$$

where the normalisation factor k_n is calculated as:

$$k_n = \frac{I(E_2) - I(E_1)}{\int_{E_1}^{E_2} dE' [S(E') - B_0 - B_{n-1}(E')]} \,. \tag{2.20}$$

Usually, only a few iterations are needed until convergence of the background curve is achieved [53]. The use of the Iterative Shirley background for the analysis of the measured data is described in section 3.2.2.

2.2.4. Information depths and photoionization cross section

The information depth is commonly defined as $3\,\lambda_{in}$, with λ_{in} being the Inelastic Mean Free Path (IMFP) of an excited electron. The IMFP is given by the average distance an electron travels between successive inelastic collisions. Only unscattered electrons or ones that were elastically scattered can contribute to the intensity of a photoelectron peak. The Beer-Lambert law:

$$I(x) = I^{\infty} \exp(-x/\lambda_{\mathrm{in}}) \tag{2.21}$$

describes the electron intensity I of each layer at a depth x. I^{∞} is the integrated intensity over an infinitely thick layer, and the attenuation length λ_{in} equals the IMFP. Integrating equ. (2.21) over a depth of $3\,\lambda_{\mathrm{in}}$ accounts for around 95% of the total intensity. In the experiment, additionally to the photon energy, the angle θ between the surface normal and the detected photoelectron beam determines the depth sensitivity (see Fig. 2.16). As consequence equ. (2.21) reads:

$$I = I^{\infty} \exp(-x/\lambda_{\mathrm{in}} \cos\theta) \,. \tag{2.22}$$

Figure 2.16 b) plots equ. (2.22) for different θ. The value of the IMFP depends on the density of the elements or compounds as well as the kinetic energy of the electrons. Figure 2.17 a) depicts the IMFP as calculated from optical properties for 41 elements, showing a significant increase for high kinetic energies. A straight dotted line marks the

photon energy used for the HAXPES experiments in this thesis. Exemplary calculating the information depth ($3\,\lambda_{in}$) for Ir and Hf at this energy results in 15 and 25 nm [48]. Although higher energies yield an enhanced information depth, the trade-off is a reduced photoionization crosssection $\sigma(E_{kin})$ (see Fig. 2.17 b) as well as appendix A.2). Experimentally, this constraint can be overcome by using high photon flux found, e.g., at synchrotron facilities (see sec. 2.2.5).

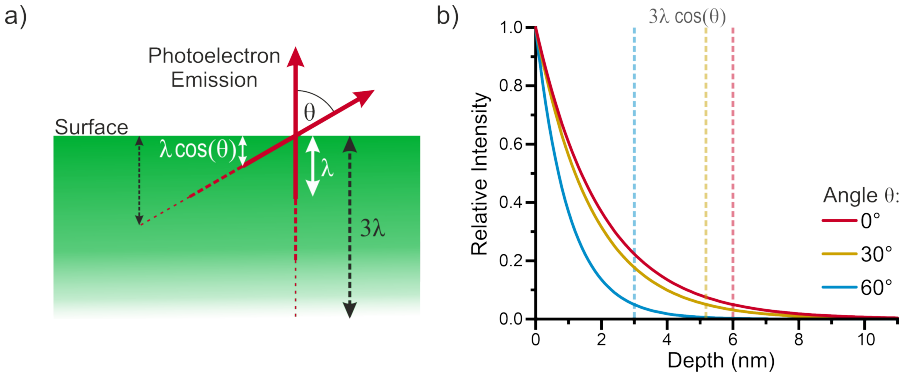

Figure 2.16.: a) Schematic representation of the angle dependence in equation 2.22. b) Plot of equ. (2.22) for different angles and $\lambda = 2$ nm. The dotted lines mark the position of the information depth 3λ at different emission angles.

(Hard) x-ray photoelectron spectroscopy

Hard X-ray Photoelectron Spectroscopy (HAXPES) is a powerful element selective technique for studying the chemical and electronic properties with significant bulk sensitivity. Comparing HAXPES (E_{Ph} = 2 keV to 10 keV) to X-ray Photoelectron Spectroscopy (XPS) (E_{Ph} = 1.2 keV to 1.5 keV), many benefits of high photon energies become apparent. In both energy ranges, deeply bound core-level electrons can be reached, but the higher energies of HAXPES result in much larger probing depths. The energy ranges are depicted in Figure 2.17 as shaded areas. The layer structures studied in this thesis have a thickness of around 20-30 nm making high energies a requirement.
The enhanced bulk sensitivity within HAXPES also makes it easier to neglect surface contamination, which can have a strong impact on the quality of the measurement in the case of XPS. This effect will be illustrated in the following, using an example in which a typical X-ray source for XPS, e.g., an Al anode ($E_{K\alpha}$=1486.6 eV), is compared to the photon energy used in this thesis (E_{Ph}=6 keV). The increased bulk sensitivity reduces the relative signal intensity of possible surface contamination (e.g., C).
Figure 2.18 shows the estimated C contribution in the C 1s core level for the surface and bulk C in a HfO_2 model layer with 1% C in the bulk of the layer and a 2 Å carbon layer at the surface. Where for XPS with 1.5 keV photon energy, the C contribution of the surface amounts to 77%, for HAXPES with 6 keV this contribution is reduced

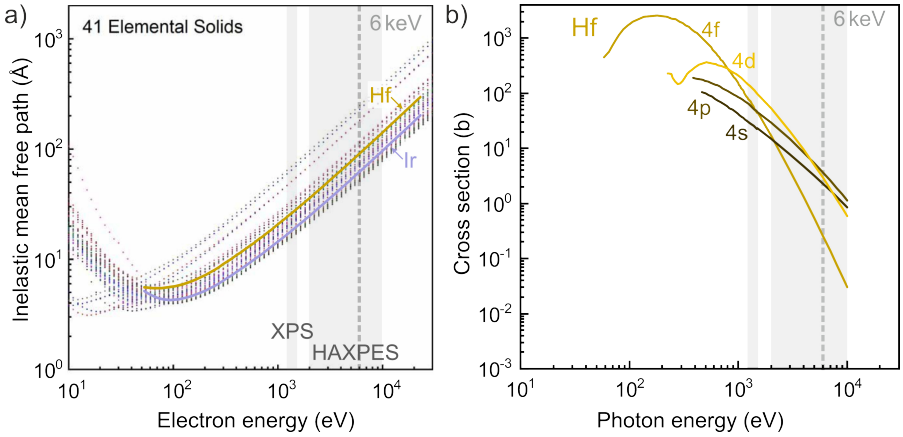

Figure 2.17.: a) Electron inelastic mean free paths as calculated from optical properties for 41 elements. Solid lines highlight the curves for Hf and Ir. The image and data are from [48]. b) Photoionization cross sections of the Hf 4f, 4d, 4p and 4s core level. The data for these plots stem from [55, 56].

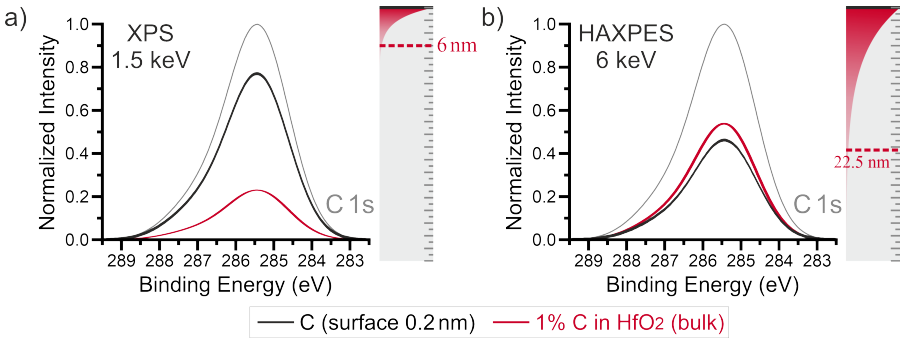

Figure 2.18.: Comparison of the contribution of surface C on the C 1s core level. The model system is a 0.2 nm thick C layer at the surface and HfO_2 bulk material with 1% C content. The C 1s plots show the C contribution of the surface in black, the contribution of the bulk C in red, and the sum of both in grey. The surface contribution in a) is 77%, and in b) 46.2%. The diagrams show the information depth marked by a dashed red line.

to 46.2% (see appendix A.3 for the complete calculation). With HAXPES, it is easier to distinguish between surface and bulk carbon. Another advantage of higher photon energies is that spectral analysis is simplified in several ways [57]:

- Since the IMFP is enhanced, the secondary electron background is significantly reduced, making the analysis process more reliable and effortless.
- After a core ionization by photoelectron emission, an outer shell electron can fill the created vacancy, releasing energy which can result in the emission of an Auger electron, detectable as a peak in the spectrum. The binding energy of Auger peaks is linearly proportional to the photon energy. For XPS, Auger peaks can overlap with photoelectron peaks whose detailed analysis is desired. At higher photon energies, the Auger peaks are "pushed" to higher binding energies, thus avoiding the overlap.
- The analysis and interpretation of the peak intensities become simpler. This fact has several reasons, e.g., that the IMFP, a crucial factor influencing peak intensity, has much less variation at higher energies (see Fig. 2.17 a)).

In order to reach the photon energy and flux needed for the HAXPES experiment synchrotron radiation is used.

2.2.5. Synchrotron radiation

Synchrotron radiation is a special case of bremsstrahlung, where charged particles (e.g. relativistic electrons) have a velocity close to the speed of light c. Considering an accelerated electron in a non-relativistic case, it exhibits the radiation field of a Hertzian dipole. The intensity maximum of the radiation field is perpendicular to the acceleration $\vec{a}$ and disappears in the direction of acceleration (see Fig. 2.19 a)). In the case of a circular motion, acceleration and direction of motion of the electron are perpendicular to each other, and the intensity maximum of the radiation field points in the direction of flight [58]. Figure 2.19 shows the radiation fields for different velocities. If an electron has a velocity >90% of the speed of light, the radiation field in the laboratory system resembles a radiation cone with an opening angle $\theta = 1/\gamma$ [49]. Here γ is the Lorentz factor, which can be described by the ratio of the electron velocity v to the speed of light as well as by the ratio of the total energy E_{total} to the rest energy of the electron E_0:

$$\gamma = \frac{1}{\sqrt{1 - \frac{v^2}{c^2}}} = \frac{E_{\text{total}}}{E_0}\,. \tag{2.23}$$

Synchrotron facilities like the Deutsches Elektronen-Synchrotron (DESY) can operate at E_{total} up to 6 GeV, which compared to the rest energy of an electron ($E_0 \approx 0.5$ MeV), results in γ=$1.2 \cdot 10^4$ or a velocity of $\approx$ 0.99999999% c. Thus the opening angle of the emitted photon beam is just a few µrad. Synchrotron radiation is realized and used in synchrotron facilities such as DESY. Figure 2.20 shows a schematic of a general design of a synchrotron. Electrons are emitted from an electron gun and then accelerated in a

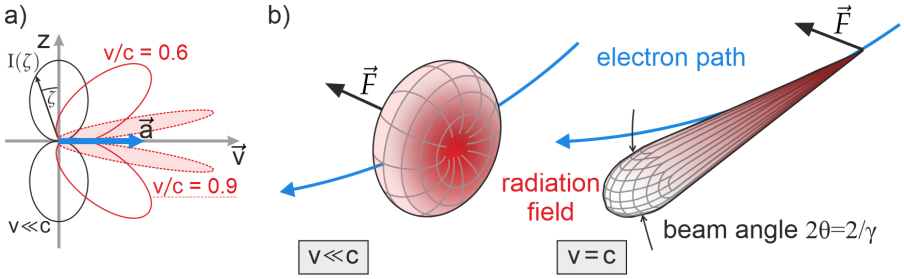

Figure 2.19.: a) Section through the radiation characteristic of a uniformly accelerated charge at different velocities $\vec{v}$ ($\vec{a}||\vec{v}$). The radiation pattern is rotationally symmetric around the direction of acceleration $\vec{a}$. The template for the picture is taken from ref. [58]. b) Radiation field of an electron on a circular orbit in the non-relativistic and relativistic case.

linear accelerator to a speed >90% of light before being transferred to the storage ring. Inside the storage ring, the electrons are kept at the same speed and are forced onto circular paths by magnetic fields to emit photons tangentially at the beamlines. In the storage ring, the electrons must also be accelerated to compensate for the kinetic energy released by the radiation. This is done with the help of cavity resonators for microwaves which are located in linear sub-segments.

Undulator

For the magnetic fields deflecting the electron to produce synchrotron radiation, so-called *undulators* are used in the combination with HAXPES. In general, an undulator consists of dipole magnets placed in alternating north-south alignment. The periodic length λ between two consecutive magnets with the same alignment is generally several centimeters. At the beamline P22 at DESY, the undulator U33 has a periodic length of $\lambda = 32.8\,\text{mm}$ [59].
The magnet arrangement forces electrons on their trajectory onto a sinusoidal path, emitting synchrotron radiation each time the electrons accelerate (see Fig. 2.20 b)).
The radiation emitted at the different points of the electron path interferes with each other so that the radiation is confined to a small angular range [60]. The resulting photon flux can reach values of $10^{13}\,\text{Ph/s}$ [61], which is ideal for HAXPES experiments.
The emitted synchrotron radiation consists of photons with continuously varying energies. For HAXPES experiments, the photon beam has to be reduced to the desired photon energy and be focused on the studied object. Following the layout of the beamline P22 at DESY is used as an example to show the optical components needed.

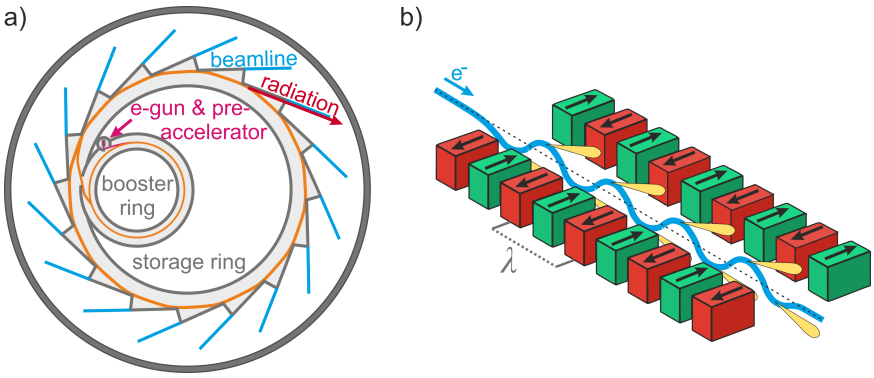

Figure 2.20.: a) Schematic representation of a synchrotron. The path of the electrons is drawn in orange. After the multi-stage process of acceleration (electron gun, pre-accelerator, booster ring), the electrons pass through the storage ring. Deflecting magnets in the storage ring force the electrons onto circular paths, at which the synchrotron radiation is emitted tangentially. The beamline contains the optics and the experiment. b) Schematic depiction of an undulator. The different magnetization directions of the magnets are marked in different colors. In blue, the trajectory of the electrons is drawn.

2.2.6. Beamline P22 at DESY, Hamburg

Figure 2.21 shows the layout of P22 schematically. The photon source is a 2 m long spectroscopy undulator (U33), which provides an energy range from 2.4 to 30 keV. The energy is filtered by a double Si-crystal monochromator, consisting of remotely interchangeable Si(111) and (311) crystal pairs and a post-monochromator. Depending on the crystal pair used and photon energy filtered, different energy bandwidths are achieved (see Fig. 2.22). The energy bandwidth substantially determines the energy resolution of the HAXPES experiment. For the experiments in this thesis, the Si(311) crystal is used in combination with E_{Ph} =6 keV, resulting in an energy bandwidth of 100 meV. Further x-ray optics are used to focus the beam, achieving a beam spot size at the sample down to around 50x100 µm^2. The angle between the photon beam and the surface of the sample is described by θ. The small spot size enabled measurements at dot structures (≈400 µm^2) found at the structured surfaces of the studied samples (see Fig. 3.1). At a 90° angle to the photon beam, the SPECS Phoibos 225 HV hemispherical analyzer is positioned (see Fig. 2.23). Due to the 90°, θ also describes the angle between the detected photoelectron beam and the surface normal of the sample. Figure 2.23 shows the CAD model and a picture of the HAXPES experiment at P22.

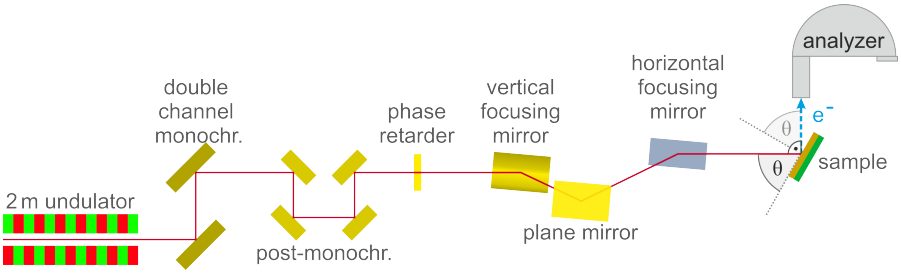

Figure 2.21.: Schematic layout of beamline P22, consisting of the undulator, the optical components, and the experiment. The photon beam and the analyzer have 90° angle. The angle between the surface of the sample and the beam is described by θ. Own image, adapted from ref. [59].

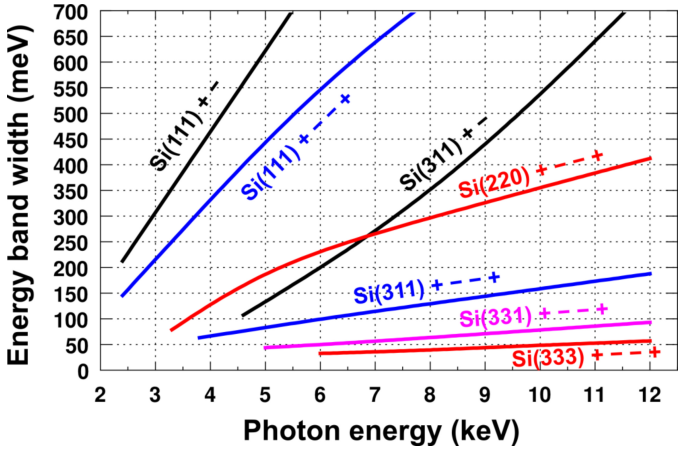

Figure 2.22.: Energy band width of different monochromator crystal configurations. The primary monochromator has two-crystal sets, Si(111) and Si(311), in (+-) configuration. The post-monochromator uses a double channel-cut with (+ - - +) configuration (zero offset). Image is taken from ref. [59].

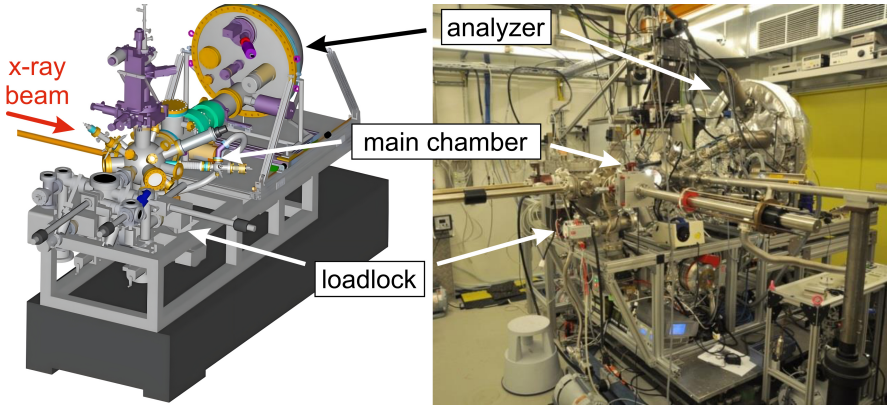

Figure 2.23.: CAD model and picture of the HAXPES experiment at the beamline P22 (DESY, Hamburg). Images are taken from ref. [59].

CHAPTER 3

Experiment

This chapter provides the experimental details of the sample preparation, pre-characterization, and parameters of the HAXPES measurement, as well as a detailed description of the data analysis. The experiments in this thesis took place in the framework of the EU project 3ϵFERRO, which had as one objective the optimization of the material properties in the HfO_2-based ferroelectric capacitor stack. Pursuing this goal, the correlation between oxygen vacancies in the $Hf(Zr)O_2$ layer and the ferroelectric properties are studied. In addition, great attention was given to the electrodes and their impact on the overall properties of the ferroelectric capacitor stack. A total of three different sets of HfO_2 capacitors were examined, which use complementary deposition techniques and electrode materials. Due to the collaboration in the EU project, the samples have been studied together with project partners using various complementary methods. In addition to studying the density and crystal structure, the electrical properties of the capacitors were investigated in a pre-characterization using electrical field switching. The sample preparation and pre-characterization are done by the project partner at NaMLab (Dresden, Germany) and are described in detail in section 3.1.
The spectroscopy experiments complete the characterization of the samples and allow a deeper understanding of the physical processes involved. The experimental details of the HAXPES measurements, as well as the analysis of the received data, are described in section 3.2.

3.1. Preparation of the HfO_2 capacitor structure

The samples studied in this thesis were fabricated at NaMLab (Dresden, Germany) by Terence Mittmann and Monica Materano. The general sample structure is a metal-insulator-metal (MIM) capacitor stack, incorporating a ferroelectric HfO_2- or HZO-layer. Figure 3.1 depicts a schematic of the sample preparation step-by-step.

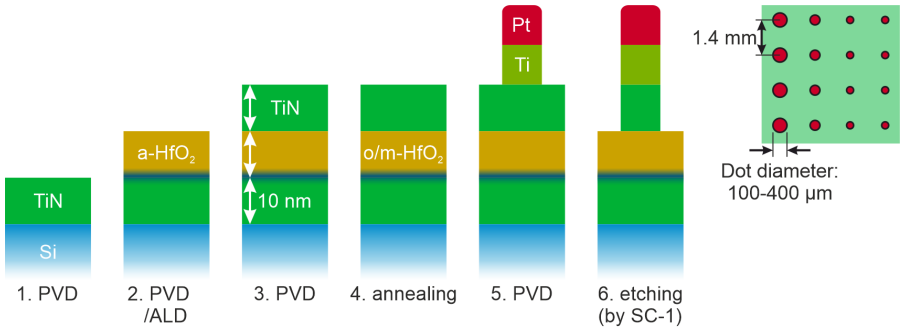

Figure 3.1.: Preparation schematics of the MIM capacitor stack. The layers of the bottom and top electrode (step 1., 3., and 5.) were deposited by PVD. For the HfO_2-layer either PVD or ALD was used. The annealing step (4.) crystallizes the structure, and the etching step (6.) structures the surface.

In the first three steps, the electrodes (TiN or IrO_2) and the ferroelectric layer (HfO_2 or HZO) are deposited onto a Si-substrate, using either Physical Vapor Deposition (PVD) or Atomic Layer Deposition (ALD), followed by an rapid thermal annealing (RTA) step.

Physical Vapor Deposition (PVD)

PVD comprises a variety of deposition methods using sputtering and evaporation [62]. In the following, the methods used in this thesis are briefly described. In reactive sputtering, the materials are sputtered from targets (TiN, HfO_2, IrO_2) in the presence of a reactive gas (N_2, O_2) usually mixed with an inert working gas (commonly Ar). In addition to reactive sputtering, also e-beam evaporation is used, where an electron beam heats the material (Ti, Pt) for deposition. The deposition takes place in a vacuum, making the layers produced via PVD of high quality with very low impurity concentration (e.g., C).

Atomic Layer Deposition (ALD)

The ALD process is based on sequential, self-saturating surface reactions, cycling between gaseous reactants (e.g., ozone, oxygen plasma) and precursors [63]. During the whole process, the substrate is heated to a specific temperature (e.g., 250°C), and an inert carrier gas (N_2 or Ar) creates an atmosphere of 1 mbar. Figure 3.2 a) shows schematically one of such a cycle. Short pulses of the precursor chemical (step 1) are introduced into the reaction chamber, followed by a purge (step 2) using the carrier gas (N_2). After those steps, a monolayer of the precursor molecule covers the surface. In the third step, the reactant is introduced and used to break up the precursor molecule and create a monolayer of the desired material. Purging the chamber again (step 4) completes one cycle.

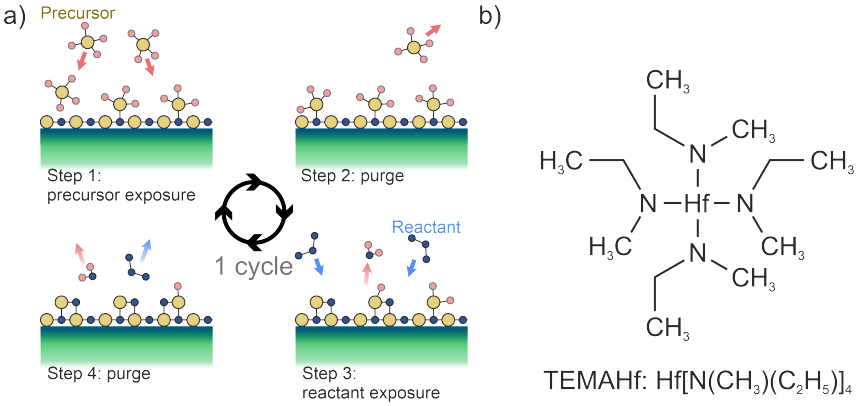

Figure 3.2.: a) Schematic of the ALD-process. In a four-step cycle, precursor and reactant are used to deposit a monolayer of the desired material. b) Schematic representation of the precursor TEMAHf.

For the the samples studied in this thesis, $[(CH_3)(C_2H_5)N]_4Hf$ (TEMA-Hf) is used as the precursor molecule. Figure 3.2 b) depicts this molecule schematically. It is possible that the precursor molecule is not entirely broken up by the reactant so that impurities like N, C, and H are incorporated into the deposited layer. Compared to the PVD process, therefore ALD incorporates a higher concentration of impurities.

Rapid Thermal Annealing (RTA)

Films produced by PVD or ALD are typically amorphous in the as-deposited state and need to be annealed to crystallize. For ferroelectric HfO_2 thin films, the orthorhombic crystal structure is targeted. In this thesis, the RTA process is used, which takes place in an ambient atmosphere, typically using nitrogen gas. Here the layer stacks are rapidly heated up and kept at a fixed temperature for crystalization. Alternative atmospheric gases in this thesis are oxygen and forming gas, which is a mixture of 90% nitrogen and 10% hydrogen.

Surface structuring

The surface of all samples is structured in an array of circular contacts ("dots") with diameters ranging from 100 µm to 400 µm. Figure 3.3 depicts the dots and the gap between them magnified by a factor of 10. For stacks with a TiN top electrode, this is achieved by depositing a 10 nm Ti adhesion layer and 50 nm Pt through a shadow mask and subsequent etching of the TiN top electrode using an SC-1 solution (50:2:1; H_2O:H_2O_2:NH_3). For IrO_2, as electrode material, depositing IrO_2 through a shadow mask is used.

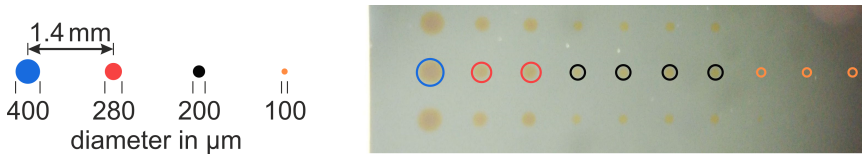

Figure 3.3.: (left) Representation of the contact dots at a scale of 1:10. (right) Microscope image of a structured surface with TiN dots.

3.1.1. Sample sets

In this thesis, three different sample sets are discussed (see Fig. 3.4 and Tab. 3.1). The first sample set is preparaed by PVD only and consists of TiN electrodes and HfO_2. An additional oxygen flow, introduced 3 min before and during the HfO_2 deposition, varies the stoichiometry of the HfO_2. For the second sample set, ALD is used for depositing the HfO_2 layer. During one ALD cycle, the precursor TEMA-Hf was supplied for 2 s, and ozone as the reactant for 10 s or 60 s. The third sample set has IrO_2 electrodes prepared by PVD and HZO as the ferroelectric layer prepared by ALD. A homogeneous HZO layer is realized by switching between deposition of HfO_2- and ZrO_2-layer and by applying the subsequent annealing step. The reactant used was oxygen plasma. As the parameter, different annealing gases were used (O_2, N_2, forming gas). Forming gas (FG) is a gas mixture of N_2:H_2 with a 9:1 ratio.

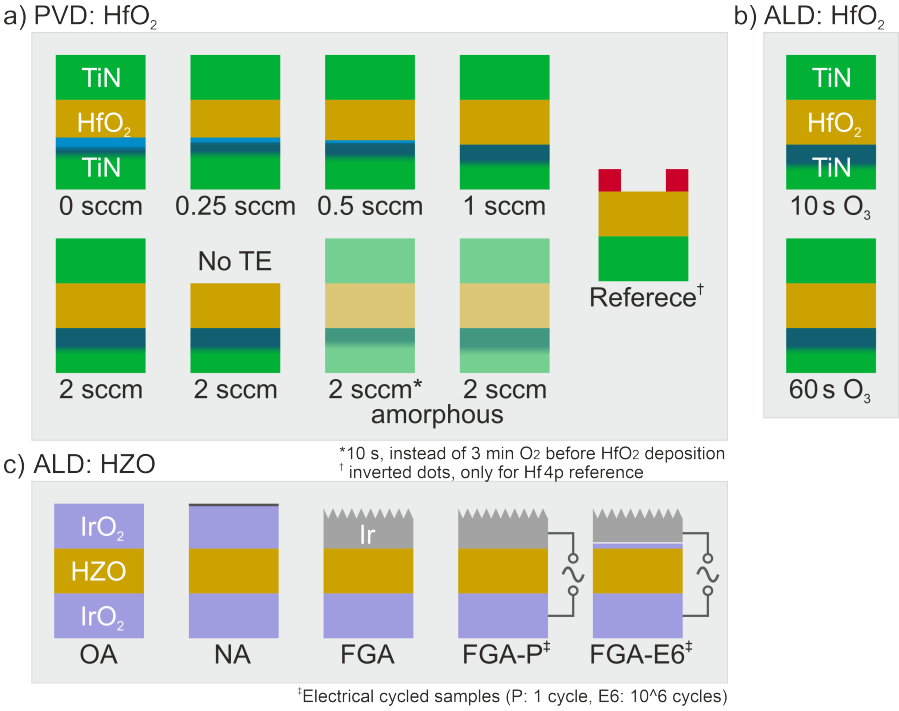

Figure 3.4.: Sample sets studied in this thesis. a) Deposition of all layers using PVD. The defining parameter is an additional oxygen flow during the HfO_2 which starts 3 min prior deposition. b) For the HfO_2 layer, ALD is used as preparation technique. The defining parameter is the time used for the reactant O_3 in each ALD cycle. c) IrO_2/HZO/IrO_2 layer stack, where only the HZO is deposited via ALD. The defining parameter is the atmospheric gas used during annealing (O_2, N_2, FG). In addition, also cycled FG annealed samples are studied.

Table 3.1.: Sample sets studied in this thesis. Samples without separating line originated from one piece and were separated during processing. The sample names are identical to the nomenclature used in the publication. The last column (Publ.) lists all publications where the sample is discussed, respectively.

Sample Name	BE	Hf-Layer	TE	Parameter	Annealing	Publ.
Method	PVD	PVD	PVD	add. O_2 flow	N_2 atmosphere	
Thickness	10 nm	10 nm	10 nm			
$S0/PVD_{0\,sccm}$	TiN	HfO_2	TiN	0 sccm	20 s at 800°C	[64–67]
S025	TiN	HfO_2	TiN	0.25 sccm	20 s at 800°C	[64, 65]
S05	TiN	HfO_2	TiN	0.5 sccm	20 s at 800°C	[64, 65]
S1	TiN	HfO_2	TiN	1 sccm	20 s at 800°C	[64, 65]
$S2/PVD_{2\,sccm}$	TiN	HfO_2	TiN	2 sccm	20 s at 800°C	[64–67]
S2 without TE	TiN	HfO_2	-	2 sccm	20 s at 800°C	[64]
a-S2	TiN	HfO_2	-	2 sccm	amorphous	[64]
$a\text{-}S2_{10\,s}$ *	TiN	HfO_2	-	2 sccm	amorphous	[64]
$R_{Hf\,4p}$ †	TiN	HfO_2	TiN		20 s at 800°C	
Method	PVD	ALD	PVD	O_3 cycle-time	N_2 atmosphere	
Thickness	10 nm	10 nm	10 nm			
$ALD_{10\,s}$	TiN	HfO_2	TiN	10 s	20 s at 700°C	[66]
$ALD_{60\,s}$	TiN	HfO_2	TiN	60 s	20 s at 700°C	[66]
Method	*PVD*	*ALD*	*PVD*	*annealing gas*		
Thickness	10 nm	17 nm	>20 nm			
OA	IrO_2	HZO	IrO_2	O_2	1 min at 500°C	[67–69]
NA	IrO_2	HZO	IrO_2	N_2	20 s at 500°C	[68, 69]
FGA	IrO_2	HZO	IrO_2	FG	20 s at 500°C	[67–69]
FGA-P‡	IrO_2	HZO	IrO_2	FG	20 s at 500°C	[67]
FGA-E6‡	IrO_2	HZO	IrO_2	FG	20 s at 500°C	[67]

* 10 s, instead of 3 min additional O_2 flow before the deposition of the HfO_2 layer
† sample with "inverted dots", only used as Hf 4p reference
‡ Electrical cycled samples (P: 1 cycle, E6: 10^6 cycles)

3.1.2. Pre-characterization

Prior to the HAXPES study, all samples were pre-characterized at NaMLab. Using a Bruker D8 Discover XRD system with a Cu K_α source, the thickness and density of the films were determined by X-ray reflectometry (XRR) and the crystal structure was investigated by Grazing incident X-ray diffraction (GiXRD). Polarization hystereses were performed on an aixACCT TF Analyzer 3000.

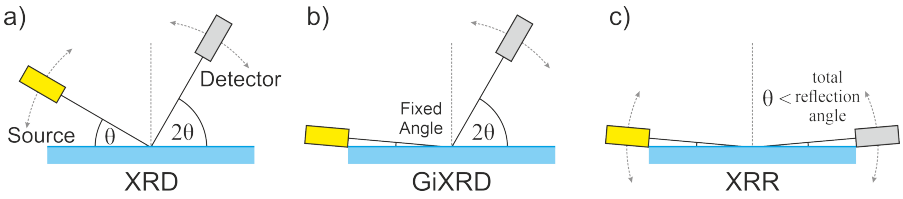

Figure 3.5.: Representation of the XRD, GiXRD, and XRR methods. a) During the XRD measurement, the Photon source and detector are moved at an angle of θ and 2θ, respectively. b) For the GiXRD measurement, the angle of the source is fixed, and only the detector is moved. c) In the case of XRR, only angles below the total reflection angle are studied. The source and detector are moved using the same angle.

Grazing incident X-ray diffraction (GiXRD)

X-ray diffraction (XRD) is a versatile technique for the characterization of crystal solids. Traveling through the crystal, the irradiated photons with the wavelength λ interact with the electronic structure of the lattice and scatter. Due to the periodicity of the crystal lattice, the scattered photons interfere with each other and form a diffraction pattern. Angles of incidence θ leading to constructive interference fulfill Bragg's condition

$$n\lambda = 2d_{hkl}\sin\theta \tag{3.1}$$

where d_{hkl} is the lattice spacing of the crystal planes with the Laue-indices (hkl). n is an integer describing the diffraction order.
During a typical XRD measurement, the incidence angle of the x-ray beam is varied, and at an angle of 2θ, the intensity of the scattered photons is measured with a detector (see Fig. 3.5 a)). This scanning method generally produces a weak signal from the surface layer and an intense signal from the lower layer of the sample. To obtain a stronger signal from the surface and avoid an intense signal from the substrate, X-ray scanning is performed with a fixed grazing angle of incidence (GiXRD), and only the detector is moved to measure the intensity of the scattered photons (see Fig. 3.5 b)).
Figure 3.6 a) shows the theoretical diffraction pattern of GiXRD for cubic TiN and the different crystal structures of HfO_2. The monoclinic HfO_2 crystal structure has a distinctly different pattern and can thus be clearly distinguished from the others.
Figure 3.6 b) depicts a GiXRD measurement of a HfO_2 layer with contributions of the orthorhombic (o) and monoclinic (m) phase.

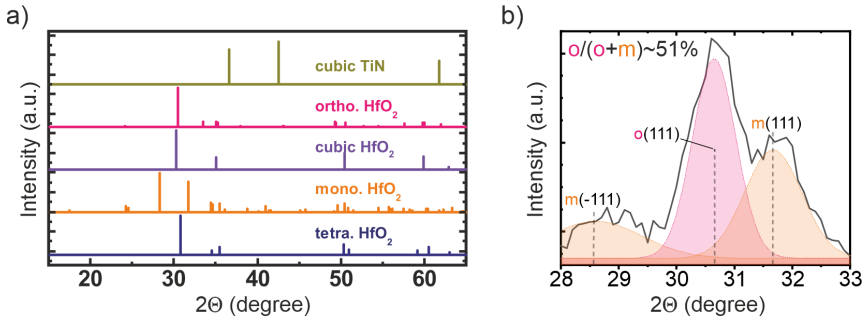

Figure 3.6.: a) Theoretical peak positions for cubic TiN, orthorhombic, monoclinic, and tetragonal HfO_2. This figure originates from [65] (Figure 4). **b)** GiXRD signal of a HfO_2 layer with contributions of the orthorhombic (o) and monoclinic (m) phase. The area of the peaks is used to determine the o/(o+m) ratio.

The ratio o/(o+m) is an important reference value and can be determined by the area ratio of the respective peaks. It is important to note that the angle of the o(111) peak is nearly identical to the tetragonal t(011) peak. Thus a source of error for the ratio o/(o+m) can lay in hidden contributions of tetragonal HfO_2.

X-ray reflectometry (XRR)

A similar experimental setup can be used to characterize materials by analyzing X-rays that are reflected by the sample. Here the sample is irradiated at an angle lower than the total reflection angle ($2\theta \approx 0° - 5°$), and at the same angle the intensity of the reflected X-rays is measured (see Fig. 3.5 c)). The reflection is based on the optical density change at interfaces. Due to reflection at multiple layers, reflected beams can interfere and produce a characteristic oscillation pattern containing thickness, density, and roughness information.

Electrical field switching

The capacitor structure of the samples enables the measurement of polarization hysteresis and thus the ferroelectric properties. A schematic representation of the measurement can be seen in Fig. 3.7 a). Two needles contact the dots, where one dot has an ohmic contact to the bottom electrode. This is achieved by applying a high voltage shortening the ferroelectric layer. One way to measure the polarization hysteresis is the so-called "dynamic hysteresis measurement". Figure 3.7 b) depicts the pulse sequence of the voltage (electric field E), which is switched in a triangular manner. While switching, the current is measured and integrated to obtain the polarization hysteresis. The pulse sequence consists of four cycles to get a relaxation-free closed hysteresis loop. The closed loop is constructed only of data measured during the sweep from one saturation to the opposite saturation, excluding any relaxation of domains.

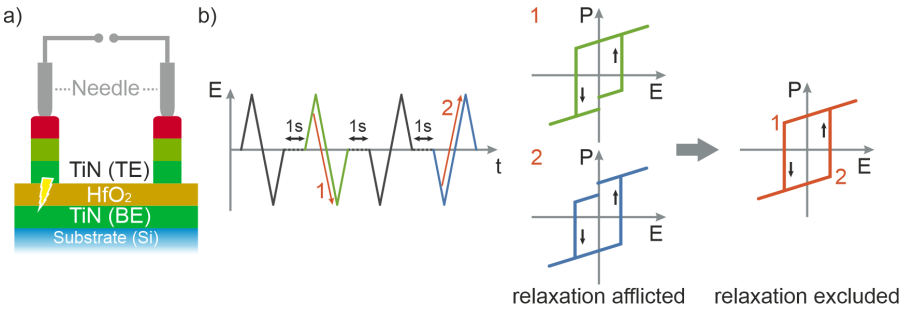

Figure 3.7.: a) Capacitor structures with measurement connections. b) Schematic of the Dynamic Hysteresis Measurement (DHM) pulse sequence using a triangular excitation as well as the obtained hystereses with and without relaxations of $P_{r-/+}$.

In this thesis, the values of the remanent polarisation P_r of the hysteresis and the switching field E_SW are mainly used to classify the ferroelectric properties. Figure 3.8 plots the measured current during DHM and the resulting hysteresis loop. The switching field is determined at the maxima of the current measurements, which can be influenced by internal electrostatic fields.
In all representations of P_r the negative and positive values are added up to form the double remanent polarisation $2P_\mathrm{r}$. Comparing the positive and negative values of the coercive field can reveal shifts linked to the chemical properties:

$$(E^+_\mathrm{SW} - E^-_\mathrm{SW})\,. \tag{3.2}$$

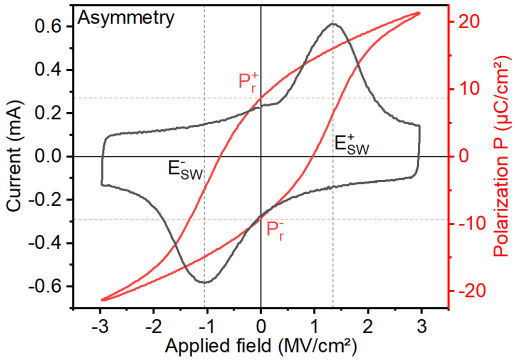

Figure 3.8.: Measured current during DHM and resulting hysteresis loop. In this thesis, the values of the switching field E_SW and the remanent polarisation P_r of the hysteresis are used.

3.2. HAXPES measurement and Analysis

In this thesis, the main technique used is hard X-ray photoelectron spectroscopy (HAXPES). The conducted HAXPES experiments were performed at the synchrotron facilities BESSY II (Berlin) and PETRAIII (DESY, Hamburg). Throughout this thesis, a photon energy of 6 keV had been used. The beamline P22 at PETRA III, DESY was mainly used to acquire the data and is described in detail in section 2.2.6.
All HAXPES experiments have been performed during so-called beam times, which lasted on average a week. Thus each experiment had to be planned considering the time constraints, finding the right balance between accuracy and time of measurement. Both are influenced by the following measurement parameters:

- Start Energy E_{Start}
- End Energy E_{End}
- Energy Stepsize ΔE
- Dwell Time t_{dwell}
- Pass Energy E_{pass}
- Position/Angle θ
- Numper of Repetions (Sweeps) n_{sweep}

Each spectrum is defined by its start and end energy (eV), divided by the energy stepsize. The intensity is measured on each energy position for the dwell time (s). The following formula can be used to estimate the time t for a spectrum:

$$t = \frac{E_{\text{End}} - E_{\text{Start}}}{\Delta E} \cdot t_{\text{dwell}} \cdot n_{\text{sweep}} \,. \tag{3.3}$$

The dwell time t_{dwell} has to be adjusted in accordance to the intensity $\mathrm{I}(E_{\text{pass}}, \theta, ...)$, which strongly depends on the angle θ between the surface normal and the analyzer. Studying buried layers (e.g., bottom electrodes) at higher angles (e.g., 5° vs. 42°) would require increasing the dwell time by 4-5 in order to get the same intensity output. The pass energy significantly influences the energy resolution of the measurement, where smaller E_{pass} increases the overall energy resolution ΔE of the analyzer but also reduces the total number of detected electrons. Thus the higher resolution comes at the expense of signal intensity (see sec. 2.2.2 *Obtaining photoelectron spectra*). Typically the pass energy is set once and then stays unchanged during a beam-time.
The majority of the HAXPES data are stored using the Hierarchical Data Format 5 (HDF5)[70], which is designed to store and organize large amounts of data. The advantage is that all experiment parameters are stored in addition to the measurement data. Those metadata include beamline-specific parameters, analyzer settings, measurement parameters, and the position on the sample holder/sample during the measurement.
All obtained data are analyzed by the software OriginPro [71].

3.2.1. Data preparation: Fermi edge determination

HAXPES spectra display the kinetic energy as a function of the measured intensity of the photo emitted electrons. To prepare the data for further analysis and to compare spectra, first the spectra have to be normalized by the dwell time (I/t_{dwell}) and the kinetic energy has to be converted into binding energy ($E_{\text{bin}} = E_{\text{Fermi}} - E_{\text{kin}}$). For the

conversion, the kinetic energy of the Fermi edge has to be determined. The Fermi edge follows the Fermi-Dirac-distribution and can be fitted by:

$$f_{\mathrm{BM}}(x) = A_2 + \frac{A_1 - A_2}{1 + \exp((x - x_c)/dx)}\,, \tag{3.4}$$

where the center x_c provides the E_{Fermi} value (see equ. (2.17)). A_1 and A_2 are the highest and lowest value of the sigmoidal (s-shaped) curve and dx defines the slope at x_c by $m_{x_c} = (A_2 - A_2)/(4dx)$. In the software OriginPro this function is named *Boltzmann*, which does **not** describe the Boltzmann distribution. Figure 3.9 shows a spectrum of the Fermi edge with the fitted function and a depiction of its parameters.

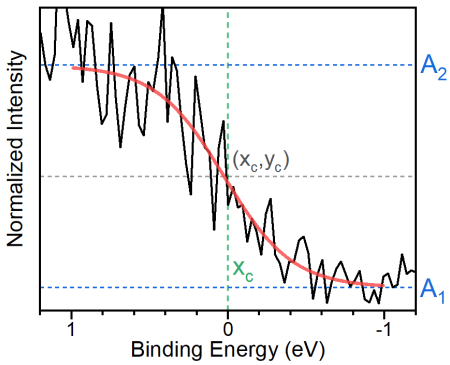

Figure 3.9.: Spectrum of the Fermi edge with the fitted function of equ. (3.4).

3.2.2. Background-subtraction

An important part of the analysis is the separation of the features of unscattered photoelectrons (core-level peaks and shake-up features), and the inelastically scattered electrons (background), see sec. 2.2.3. The primary method used to subtract the background below the peak structure is the *Iterative Shirley background*, which will be referred to as Shirley background from now on. For stand-alone peak structures, the Shirley background can directly be applied but depending on the elements, and the binding energies of the core levels contributing to the spectrum, additional overlap of different peaks and backgrounds can occur. In this case, the different contributions have to be separated first, if possible.

This section focuses on discussing the Shirley background as this method is applied to all spectra analysis, directly in the case of stand-alone peak structures or after separating possible overlap with other elements or core-levels first. Following a simple example of overlap of a stand-alone peak structure with a long rang background of another element and core-level is described.

The Shirley background evolves from an integration over the spectra and is defined by its start and end point (see equ. (2.19) and equ. (2.20)). In many cases, the start point can be set explicitly, and, in contrast, the end point has to be chosen reasonably. Figure 3.10 a) shows an extended spectrum of the O 1s, and Hf 4s core-level. To determine the start point and cut through the noise of the signal, the area before the peak is locally fitted by an exponential function. The minimum of the fit provides the start point.
A closer look at the area behind the peaks shows structures assigned to plasmons, complicating a precise determination of the end point. The intensity value of the end point has to be smaller than the plasmons. To approach a reasonable end point, the minima between the high energy features are determined by polynomial fits.
As an example, the Shirley background created by two different minima are compared (see dotted lines in Fig. 3.10 a)). Since the starting point is equal, the shape of the background and the relative areas of the peaks remain the same. Only the normalization and thus the total area of the combined peaks changes. In the shown example, the area of the O 1s and Hf 4s peaks (522 eV-545 eV) differ around 4% between the different backgrounds.

Some peak structures overlap with the background of others. Figure 3.10 b) depicts the overlap of the Hf 4d core level background and the C 1s core level. In the vicinity of the C 1s core level, the Hf background can be assumed to be linear and be approximated by a linear fit (see inset 1.). Subtracting this linear fit leaves the C 1s core level with a Shirley background.
Regardless of the chosen background treatment, comparability is given as long as the treatment is the same for identical systems.

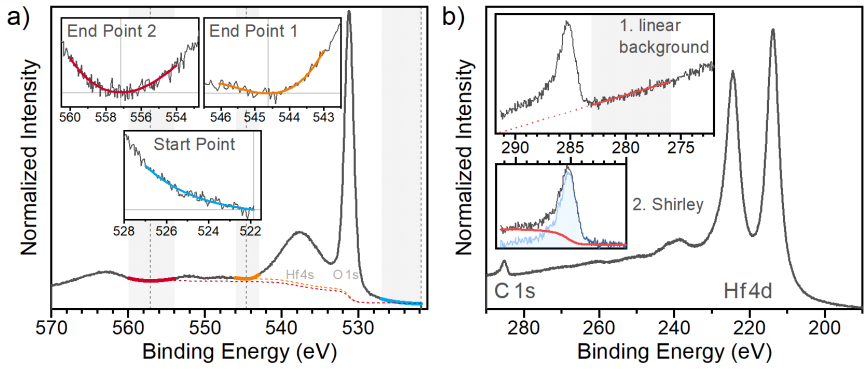

Figure 3.10.: Background determination: a) Extended O 1s, Hf 4s spectrum with exponential and polynomial fits (see insets). The minima of the fits are used as start and end points for Shirley backgrounds (dotted curves). b) Overlap of the Hf 4d core level background and the C 1s core level. In the vicinity of the C 1s core level, the Hf background can be assumed to be linear (see inset 1.). Without this linear background, the remaining one can be treated by a Shirley background.

Using reference data

All sample sets and references were conceptualized for broad comparability. Following the data processing for background subtraction and distinguishing hidden signals via reference data will be described using the example of Hf 4p spectra.
The Hf 4p spectra have strong plasmon contributions overlapping with the N 1s, and Ti 2p core levels. To separate the Hf 4p signal and its features from a typical spectra (*Sample*), a reference spectra containing no signal from TiN is used (see Fig. 3.11 a)). In Figure 3.11 b) the sample and reference spectra are shown, normalized to the lowest datapoint (1) and the maximum of the Hf $4p_{3/2}$ peak (2). With increasing binding energy both spectra deviate from each other (see inset in Fig. 3.11 b)). This deviation stems from a slightly different background signal, which can be corrected by subtracting the linear fit of the difference. Figure 3.11 c) plots the normalized and corrected spectra and has two insets depicting the extractable Ti 2p, and N 1s core levels.
The remaining background of the obtained Ti 2p and N 1s spectra are treated as described in the previous section 3.2.1. Figure 3.11 d) shows the isolated Ti 2p spectrum containing overlapping contributions of TiN and TiO_2. Using a reference Ti 2p spectra with a low TiO_2 signal, the TiO_2 contribution can be isolated, and the peak position and shape of the TiO_2 contribution can be determined.
After dealing with the background, the spectra can be fitted using the area constraints of the spin-orbit coupling and specified core-level line-shapes.

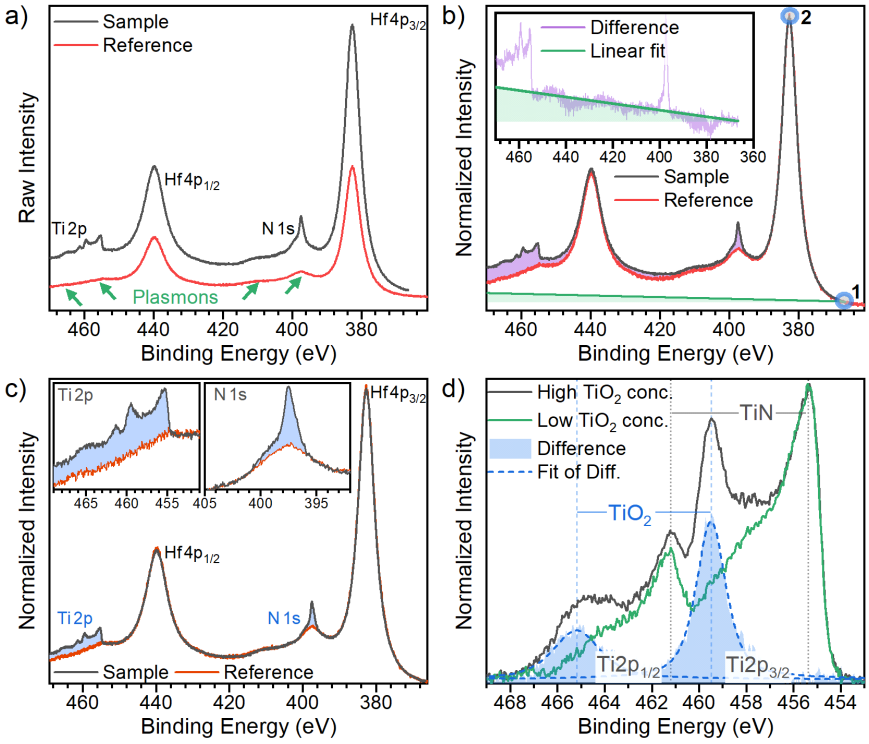

Figure 3.11.: Examples of how to use reference data: a) Raw Hf $4p_{3/2}$ spectra of samples with (*Sample*) and without Ti and N signal (*Reference*). The Hf $4p_{3/2}$ shows plasmons overlapping with the Ti 2p and N 1s core levels. b) Aligning the sample to the reference spectra by normalizing to the Hf $4p_{3/2}$ peak and compensating differences in the background. The inset shows a linear fit of the difference to determine the additional background. c) Using the aligned spectra, the Ti 2p, and N 1s core level can be extracted. d) Comparison of Ti 2p spectra from samples with high and low TiO_2 concentration to separate the signal from TiO_2. The difference's fit allows for identifying the exact position and shape of the hidden peaks.

Core-level line-shapes

Modeling the core-level shape in photoelectron spectroscopy requires a reasonable choice of the line shape. Considering the ionization process and the finite lifetime of the excited states, a Lorentzian-type profile is a basic representation. Some Gaussian characteristics have to be added to the line-shape, due to temperature-induced Doppler and phonon broadening [57, 72], possible imperfections (randomness) in the sample, and the experimental resolution, e.g., of the monochromator and analyzer.
The Gaussian character can be introduced to the Lorentzian line shape through a convolution known as the Voigt function $V(x)$. For this thesis, the Pseudo-Voigt function $V_{\mathrm{P}}(x)$ is used, which is an approximation of the Voigt profile $V(x)$ and represents a linear combination of a Gaussian curve $G(x)$ and a Lorentzian curve $L(x)$:

$$\begin{aligned} V_{\mathrm{P}}(x) &= \mu \cdot L(x) + (1-\mu) \cdot G(x) \\ &= y_0 + A \left[\mu \frac{2}{\pi} \frac{w}{4(x-x_c)^2 + w^2} + (1-\mu) \frac{\sqrt{4ln2}}{\sqrt{\pi} w} e^{\frac{4ln2}{w^2}(x-x_c)^2} \right] . \end{aligned} \tag{3.5}$$

The form factor μ defines the weighting between $G(x)$ and $L(x)$. The parameters of the curve consist of a contant factor y_0, the amplitude A, the center position x_c, and the Full Width at Half Maximum (FWHM) w. A representation of the the different curves can be seen in Fig. 3.12.
Metallic materials usually display asymmetry in the peak form due to electron-hole excitations near the Fermi level, not observed in semiconductors and insulators. For the latter, the bandgap inhibits the excitation of low-energy electrons just below the Fermi level.

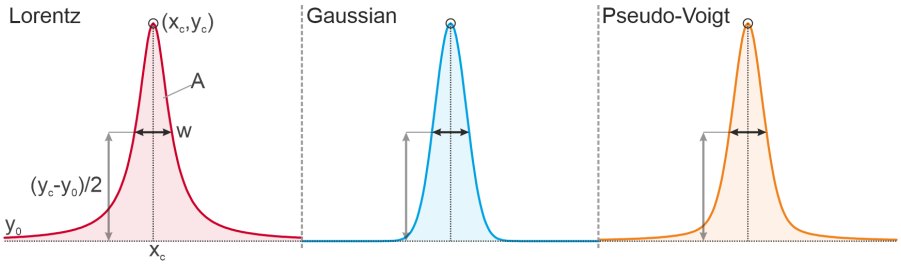

Figure 3.12.: Representation of the Lorentz-, Gaussian-, and Pseudo-Voigt curve. Own representation.

3.2.3. Fitting procedure

In the following, the iterative fitting process will be shown in more detail, using the Ti 2p spectra exemplary. First of all, it is necessary to clarify which components a spectrum contains and how many peaks are to be assumed, starting by studying the literature for similar materials and measurements. In general, for core levels with an orbital momentum larger than zero, the spin-orbit coupling doubles the number of possible peaks and specifies the area ratio between them (see Tab. 2.1). A 2p core level shows an area ratio between the subshells of 1:2.
The Ti 2p spectrum of a TiN/TiO_2 contains at least 8 components, 4 for TiN and shake-up peak, 2 for TiO_2 and 2 for the mixed state of TiN_xO_y at an interface (see Fig. 3.13). The comparison of Ti 2p spectra from samples with high and low TiO_2 concentration, shown in the previous section, can be used to determine the binding energy as well as the parameters for the shape of a peak. As the first input, the obtained parameters and the binding energies found in the literature are used [73–75]. Even if the parameters of the literature cannot be transferred directly, distances between the binding energies of the peaks give good starting values. In addition to the area ratio (1:2) between $2p_{1/2}$ and $2p_{3/2}$ peaks, the area ratios within a subshell are kept the same, respectively. Figure 3.13 a) shows the fit of a Ti 2p core level spectrum with a TiO_2 concentration. The area of TiN's shake-up feature is larger than the main TiN peak and could contain additional contributions of TiN_xO_y. To be able to fit the TiN signal, it turned out that it is good to set the peak width the same for both subshells. Table 3.2 lists the parameters and its relations used in the fits.
The fitting procedures result in exact binding energies and quantification of the relative signal contributions. Comparing the binding energies across multiple samples provide information about possible shifts and their type (see sec. 2.2.3 *Binding energy shifts*). The energy difference between the TiN and the TiN_xO_y peak at the Ti 2p core level is an example of a chemical shift, which can also be observed at the N 1s core level. Since the N 1s core level is the counterpart to Ti 2p, the TiN_xO_y contribution shift to lower binding energies. Figure 3.13 b) depicts the fit of N 1s core level spectra with high (low) TiO_2 concentration. In the context of the TiN/HfO_2 stack, the TiO_2 concentration manly controls the possible formation of HfN.

Table 3.2.: Ti 2p fitting parameters for a TiN/TiO_2 layer stack. For the different TiN contributions, a relative area is calculated.

	TiN	TiN_xO_y	TiN shake-up	TiO_2
	Gaussian	**Ps.-Voigt**	**Gaussian**	**Ps.-Voigt**
Bin. Energy $\mathbf{x_c}$	455.4	456.3	457.6	459.5
ΔEnergy ($\mathbf{x}_{Ti\,2p_{3/2}}$-$\mathbf{x}_{Ti\,2p_{1/2}}$)	5.8	5.7	5.5	5.7
Rel. Area ($\mathbf{A}_x/\mathbf{A}_{TiN}$)	1	0.52	1.38	-
FWHM $\mathbf{w}_{Ti\,2p_{3/2}}$	1	1	2.6	1.5
FWHM $\mathbf{w}_{Ti\,2p_{1/2}}$	1	1	2.6	2.4
Form Factor μ	-	0.723	-	0.723

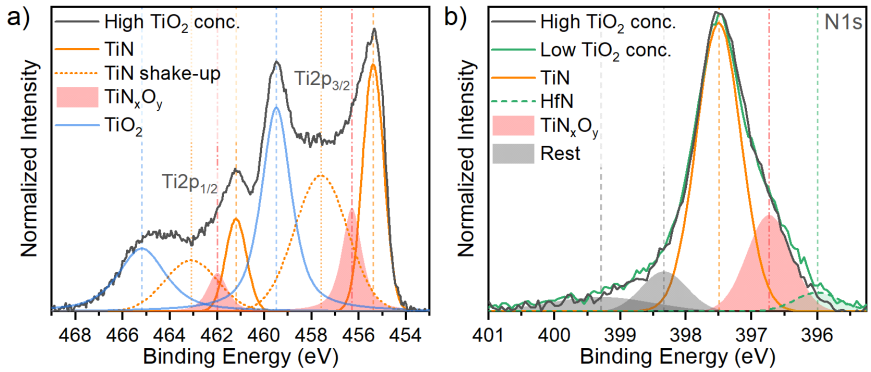

Figure 3.13.: a) Spectrum of the Ti 2p core level from a high TiO_2 concentration with the fitted contributions. b) The N 1s core level of samples with high and low TiO_2 concentration. The difference reveals a HfN contributions at 396 eV for the low TiO_2 conc. sample. The higher energy peaks (*Rest*) are related to different molecular nitrogen species, which are inherent features characteristic of TiN.

Valence band (VB) maximum and Kraut method

In section 2.2.3 the origin of binding energy shifts is explained. One possibility to distinguish between a chemical shift or Fermi level shift is to study the energy difference between the core levels and the VB maximum (VB_{max}) since this value is independent of the Fermi level [57]. Any shift in VB_{max} will likewise shift the core levels equivalently. The VB_{max} can be determined by fitting the valence band area with a step function (e.g., f_{BM} from equ. (3.4)), and generating a linear equation from the center position (x_c, y_c) and the slope $m = f'_{BM}(x_c)$ at this position. Figure 3.14 a) shows the fit of the valence band area and the linear equation whose zero-crossing x_0 corresponds to VB_{max}. This value can be calculated by:

$$x_0 = \frac{x_c \cdot m - y_c}{m} . \tag{3.6}$$

In layer stacks of different materials, the VB of those materials can overlap, making a direct determination of VB_{max} difficult. In those cases, the Kraut method can be applied [76, 77], which uses the fact that the energy difference between the VB_{max} and any core-level has a material-specific value. The first step of this method involves the determination of the energy difference E_{diff} between an appropriate core level and the VB_{max} in reference bulk or thick-film samples of the material represented in the layer stack (see Fig. 3.14 b)). Ideally, the binding energy of the chosen core level is uncomplicated to determine, and the core level can be recorded together with the VB in a single spectrum. The determined values are then combined with the binding energies E_{stack} of the same core levels in the layer stacks to determine VB_{max}: $VB_{max} = E_{stack}\text{-}E_{diff}$.

In this thesis, the Kraut method becomes relevant for the samples having IrO_2 as electrode material (see chapter 6) and is used to form a model of the binding energy shift in the metal-insulator-meta stack. This is realised by comparing the VB_{max} of the insulator layer (HZO) with and without top electrode. For the VB_{max} value with top electrode the Kraut method has to be applied, since the signal of the top electrode overlaps with the signal of the insulator layer. Figure 3.14 c) plots the HAXPES spectra of a sample measured with and without a IrO_2 top electrode. Due to the measurement without top electrode, the Hf $4f_{7/2}$ core level and the VB_{max} can be determined. This value can be assigned to the bottom interface. For the measurement with top electrode, the Kraut method has to be applied to determine VB_{max}, which can be assigned to the top electrode. In this example, the VB_{max} value is smaller at the top interface than at the bottom electrode, indicating the existence of a bias field pointing in the direction of the bottom electrode.

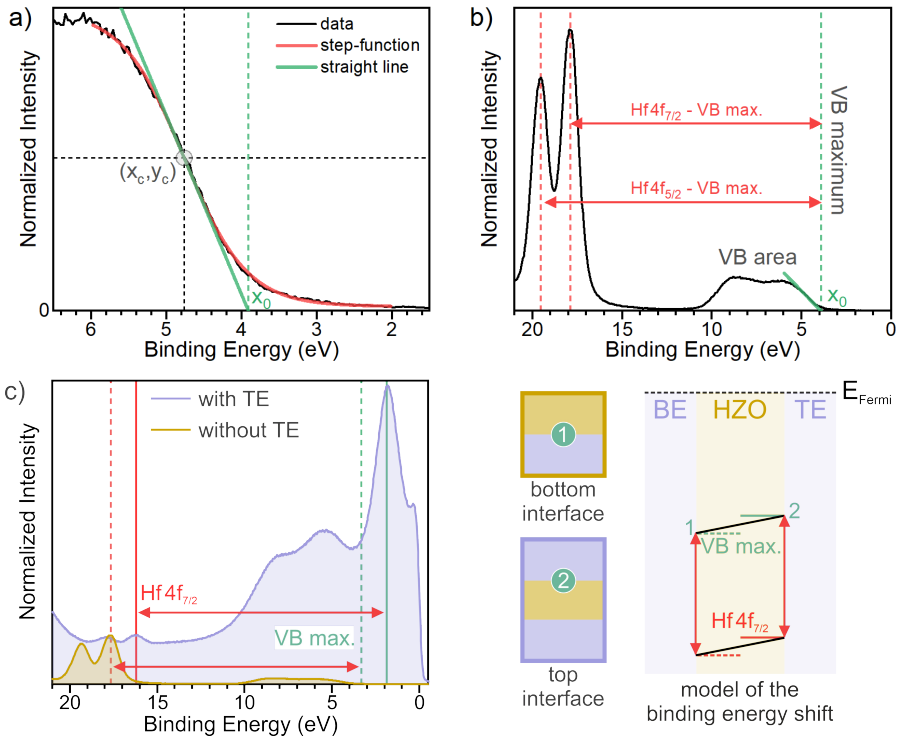

Figure 3.14.: a) Determination of VB_{max}; b) Illustration of the energy difference between VB_{max} and the core levels. c) Exemplary use of the Kraut method. HAXPES spectra of the Hf 4f, and VB area is used to determine the VB_{max} values at the bottom and top interface.

3.2.4. Thickness determination

Frequently used in this thesis is the determination of layer thicknesses by comparing the measured signal intensity of photoelectrons from different layers. Using the fitting procedure described in section 3.2.3, peak areas of core levels can be obtained and the signal intensity I thus quantified. For the signal intensity comparison, usually, a single core level is chosen. For example, when studying a SiO_2 film on a Si substrate, the Si 2p core level is chosen.
The depth-dependency of the signal intensity, described in section 2.2.4, is the basis of any thickness determination and will be applied to a two-layer model. Figure 3.15) depicts two different scenarios of the two-layer model, on the one hand, the case where a homogeneous thin film lays on top of a homogeneous bulk-like layer (1.), and on the other hand, where two homogeneous thin films are given (2.):

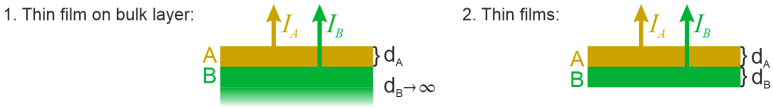

Figure 3.15.: Visual representation of signal intensity I for different layer systems.

In both cases, the top layer **A** has a finite film thickness $\mathbf{d_A}$ and a total signal intensity $\mathbf{I_A}$, which equals in the HAXPES experiment the integrated peak areas of the chosen core-level and can theoretically be described by:

$$I_\mathrm{A} = I_\mathrm{A}^\infty \cdot [1 - \mathrm{e}^{-d_\mathrm{A}/(\lambda_\mathrm{A,A}\cos\theta)}]\,. \tag{3.7}$$

Here I^∞ is the total intensity of a theoretical infinite thick layer, which can be determined by the measurement of the same material as a bulk layer, assuming that all experimental parameters are unchanged, or can be calculated, if the experimental and material parameters are known in detail (e.g., X-ray flux density, atomic number densities). $\lambda_{x,y}(E_\mathrm{kin})$ is the attenuation length of photoelectrons in layer y emitted from layer x. For a bulk-like layer **B** beneath layer **A**, the signal is dampened according to equ. (2.22):

$$I_\mathrm{B} = I_\mathrm{B}^\infty \cdot \mathrm{e}^{-d_\mathrm{A}/(\lambda_\mathrm{B,A}\cos\theta)}\,. \tag{3.8}$$

Studying the same core level, like Si 2p in a Si/SiO_2 system, the attenuation length $\lambda_\mathrm{A,A}$ and $\lambda_\mathrm{B,A}$ can be assumed being equal. In this case, the thickness of a thin film A on a bulk layer B can be determines by the ratio $I_\mathrm{A}/I_\mathrm{B}$:

$$\begin{aligned} \underbrace{\frac{I_\mathrm{A}}{I_\mathrm{B}}}_{R} &= \underbrace{\frac{I_\mathrm{A}^\infty}{I_\mathrm{B}^\infty}}_{R^\infty} \frac{[1 - \mathrm{e}^{-d_\mathrm{A}/(\lambda_\mathrm{A,A}\cos\theta)}]}{\mathrm{e}^{-d_\mathrm{A}/(\lambda_\mathrm{B,A}\cos\theta)}} \approx R^\infty(\mathrm{e}^{d_\mathrm{A}/(\lambda_\mathrm{A,A}\cos\theta)} - 1) \\ \Leftrightarrow \quad d_\mathrm{A} &= \lambda_\mathrm{A,A}\cos\theta \cdot \ln\left(R/R^\infty + 1\right). \end{aligned} \tag{3.9}$$

R and R^∞ are the ratios of the intensities I and I^∞. In the second scenario of two thin films, layer B has a finite layer thickness d_B and signal intensity of:

$$I_\mathrm{B} = I_\mathrm{B}^\infty \cdot [1 - \mathrm{e}^{-d_\mathrm{B}/(\lambda_{\mathrm{B,B}} \cos\theta)}] \cdot \mathrm{e}^{-d_\mathrm{A}/(\lambda_{\mathrm{B,A}} \cos\theta)} \,. \tag{3.10}$$

The ratio of the signal intensity of two thin layers can be calculated by:

$$R = R^\infty \frac{[1 - \mathrm{e}^{-d_\mathrm{A}/(\lambda_{\mathrm{A,A}} \cos\theta)}]}{[1 - \mathrm{e}^{-d_\mathrm{B}/(\lambda_{\mathrm{B,B}} \cos\theta)}] \cdot \mathrm{e}^{-d_\mathrm{A}/(\lambda_{\mathrm{B,A}} \cos\theta)}} \,. \tag{3.11}$$

This equation can be resolved for the thickness of d_A or d_B and needs the knowledge of the respective other. In this thesis, the second model applies to the sample system studied. In order to use the equations the parameters have to be determined. As mentioned, the values for I_A and I_B are determined by the HAXPES experiment. However, the values for R^∞ and λ can not be obtained directly and have to be calculated by theoretical values.

Effective Attenuation Length (EAL)

For quantitative analyses, it has been shown that it is insufficient to use the IMFP λ as attenuation length [78]. Elastic electron scattering of photoelectrons can lead to a significantly different length traveled through the solid, thus changing the attenuation length. For common measurement conditions, the attenuation length becomes smaller [79]. Taking elastic-scattering into account, the Effective Attenuation Length (EAL) is applied. For high energy X-rays, the EAL can be calculated by [79]

$$L = \lambda_\mathrm{in}(1 - 0.738\frac{\lambda_\mathrm{in}}{\lambda_\mathrm{in} + \lambda_\mathrm{tr}}) \tag{3.12}$$

with λ_in as the IMFP and λ_tr as the Transport Mean Free Path (TRMFP), defined by the average distance between successive elastic collisions. The theoretical values needed for L are created by the SESSA software.

Simulation of Electron Spectra for Surface Analysis (SESSA)

SESSA is a software from the National Institute of Standards and Technology (NIST) to, among other options, be used to simulate AES, and XPS spectra [80]. In this thesis, SESSA is mainly used to compute the IMFP and TRMFP of the studied sample structures. These values are needed to calculate the effective attenuation length L (see equ. (3.12)). As input for the computation of IMFP and TRMFP, SESSA requires the composition of the compound, its density ρ in atoms/cm^3, and the photon energy E_Ph. Typically the density is measured in g/cm^3 and can be converted from g/cm^3 to atoms/cm$_3$ by:

$$\rho[\mathrm{atoms/cm^3}] \equiv \rho[\mathrm{g/cm^3}]/F \cdot \mathrm{N_A} \cdot n \,. \tag{3.13}$$

Here F represents the formula weight, N_A the Avogadro constant, and n the number of elements in the compound. A detailed step-by-step instruction how to use SESSA to calculate IMFP, and TRMFP is included in the appendix A.1. Using the default density for TiO_2 $\rho_{default,TiO_2}$=0.943·10^{23} atoms/cm^3 and the experimental determined density for TiN $\rho_{exp,TiN}$=1.043·10^{23} atoms/cm^3 the effective attenuation length for the Ti 2p core-level is calculated and listed in Tab. 3.3:

Table 3.3.: EAL at E_{Ph}=6 keV for the Ti 2p core-level calculated by equation 3.12.

		IMFP (nm)	TRMP (nm)	L (nm)	Mean L (nm)
TiO_2	Ti $2p_{1/2}$	8.296	128.845	7.926	
	Ti $2p_{3/2}$	8.304	129.093	7.934	*7.93*
TiN	Ti $2p_{1/2}$	7.481	92.220	7.067	
	Ti $2p_{3/2}$	7.488	92.395	7.073	*7.07*

Value for R^∞

To determine a value for R^∞, one should first restrict oneself to appropriate peaks or core-level. In the following, the Ti 2p core-level and a TiN/TiO_2 layer system will be used as an example.
R^∞=I_A/I_B is the ratio of the intensities of infinite thick samples. The values for the individual intensities will depend upon X-ray flux density, atomic number densities, asymmetry parameters, sensitivity factors, etc. For the ratio R^∞, all parameters cancels out except the atomic number densities and the effective attenuation lengths if the two layers compared contain the same element (e.g., TiO_2 on top of TiN) and the same core level is taken (e.g., Ti 2p):

$$R^\infty = \frac{N_{\mathrm{Ti,TiO_2}} \cdot L_{\mathrm{TiO_2,TiO_2}}}{N_{\mathrm{Ti,TiN}} \cdot L_{\mathrm{TiN,TiN}}} \,. \tag{3.14}$$

Here $N_{X,Y}$ is the atomic number density (atoms per unit volume) of the element X in the material Y. The ratio of N is defined by the density ρ and the formula weight F of each material:

$$\frac{N_{\mathrm{Ti,TiO_2}}}{N_{\mathrm{Ti,TiN}}} = \frac{\rho_{\,\mathrm{TiO_2}}/F_{\mathrm{TiO_2}} \cdot n_{\mathrm{Ti,TiO_2}}}{\rho_{\,\mathrm{TiN}}/F_{\mathrm{TiN}} \cdot n_{\mathrm{Ti,TiN}}} \,. \tag{3.15}$$

$n_{x,y}$ is used to weight the formula by the representation of the element x in the unit volume of the material y. Here $n_{\mathrm{Ti,TiO_2}}$ and $n_{\mathrm{Ti,TiN}}$ equals 1, but in general this can differ (e.g., $n_{\mathrm{O,TiO_2}} = 2$).
Equation (3.15) applied to TiO_2 ($\rho_{\,\mathrm{TiO_2}} = 4.18\,\mathrm{g/cm^3}$, $F_{\mathrm{TiO_2}} = 80\,\mathrm{u}$) and TiN ($\rho_{\,\mathrm{TiN}} = 5.36\,\mathrm{g/cm^3}$, $F_{\mathrm{TiN}} = 62\,\mathrm{u}$) gives $N_{\mathrm{Ti,TiO_2}}/N_{\mathrm{Ti,TiN}} \approx 0.6$. Using equ. (3.14) and the L values from Tab. 3.3 the R^∞ value for the TiN/TiO_2 layer system equals R^∞=0.673.
Experimentally R^∞ can also be determined by measuring the intensities of thick layers (>100 nm) of the materials.

This method requires exactly same conditions for each measurement and an exact determination of the intensity which can be reduced, e.g., by plasmon excitation. The experimental value for R^∞ tends to be erroneous and larger than the theoretical value.

Solution of the intensity ratio equation

Equation (3.11) is a universal description of the intensity ratio of a two-layer model without additional approximations. Comparing the intensity of the same element and core-level, the EAL of photoelectrons in the upper layer can be assumed to be similar: $L_{A,A} = L_{B,A} = L_A$. Due to this assumption and with the simplified notation L_B for $L_{B,B}$, equ. (3.11) can be rewritten to:

$$\begin{aligned} R =& R^\infty \frac{[1 - \mathrm{e}^{-d_\mathrm{A}/(L_\mathrm{A}\cos\theta)}]}{[1 - \mathrm{e}^{-d_\mathrm{B}/(L_\mathrm{B}\cos\theta)}] \cdot \mathrm{e}^{-d_\mathrm{A}/(L_\mathrm{A}\cos\theta)}} \\ \Leftrightarrow \quad d_\mathrm{A} =& L_\mathrm{A}\cos\theta \cdot \ln\frac{R + R^\infty}{R \cdot \mathrm{e}^{(-d_\mathrm{B}/L_\mathrm{B} - d_\mathrm{A}/L_\mathrm{A})/\cos\theta} + R^\infty} \,. \end{aligned} \tag{3.16}$$

The complete conversion to d_A with all intermediate steps can be found in the appendix A.4. The formula resolved to d_A is recursive and requires the knowledge of d_B.
In this thesis, the thickness determination is mainly done for the special case of TiO_2 growth on TiN by additional oxygen gas flow (or oxygen-containing atmosphere). During the oxidation of the TiN layer, the amount of Ti atoms stays the same, only the N atoms are exchanged by two O atoms. The thickness d_TiN of a former pure TiN film decreases, but the total film thickness $d_\mathrm{TiN} + d_{\mathrm{TiO_2}}$ increases, since the atomic number density of TiO_2 is lower than that of TiN ($N_{\mathrm{Ti,TiO_2}} < N_{\mathrm{Ti,TiO_2}}$). The relation of the thickness evolution can be formalized by:

$$d_\mathrm{TiN} = d_\mathrm{in} - d_{\mathrm{TiO_2}} \frac{N_{\mathrm{Ti,TiO_2}}}{N_{\mathrm{Ti,TiN}}} \,. \tag{3.17}$$

The value of d_in is predefined by the preparation method and verified by an oscillating quartz sensor. This relation can be used in equ. (3.16) to remove the dependency on d_B (d_TiN) so that only the recursive property remains. For the TiN/TiO_2 model the resulting formula looks as follows:

$$\begin{aligned} d_{\mathrm{TiO_2}} =& L_{\mathrm{TiO_2}} \cos\theta \cdot \ln \frac{R^\infty + R}{R \cdot \mathrm{e}^{-x/\cos\theta} + R^\infty} \\ \text{with} \qquad x =& \, d_{\mathrm{TiO_2}}/L_{\mathrm{TiO_2}} + (d_\mathrm{in} - d_{\mathrm{TiO_2}} \cdot N_{\mathrm{Ti,\ TiO_2}}/N_{\mathrm{Ti,TiN}})/L_\mathrm{TiN} \,. \end{aligned} \tag{3.18}$$

Although this equation is recursive, it converges to a single value. Using concrete parameters (d_in=10 nm), Fig. 3.16 illustrates the resulting $d_{\mathrm{TiO_2}}$ for starting values reaching from 0 to 10 nm over 9 iterations. After six iterations, the calculated value is exact down to the tenth decimal place.

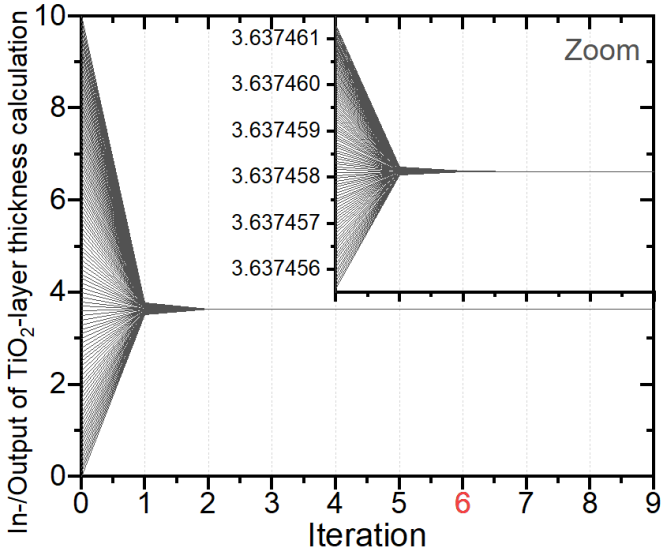

Figure 3.16.: Example of the convergence behavior of formula (3.18), calculating the effective layer thickness of TiO_2. With each iteration, the calculated value converges closer to the same effective layer thickness. After six iterations, the values differ at the eleventh decimal place.

CHAPTER 4

I. Interface properties and oxygen vacancies

This work focuses on identifying stabilizing factors for the ferroelectric phase in HfO_2 and HZO thin films. Since those thin films are integrated into a capacitor structure, the influence of the electrodes on the electrical and ferroelectric properties is also explored in detail. In total three different sample sets are studied, differentiating by different deposition techniques and electrode material (see Table 3.1). The results of those studies have been reviewed and published [64–69]. The results will be presented in three separate chapters dedicated to the three publications where HAXPES studies are the main focus [64, 66, 68]. The chapter 4 illuminates the properties and formation of the interface between the bottom TiN electrode and the HfO_2 layer, as well as the role of oxygen vacancies in the stabilization of the ferroelectric phase. The following chapter 5 compares the sample set with TiN electrodes and different deposition techniques, extracting how various types of oxygen vacancies influence the overall properties and how the types can be distinguished using HAXPES. Thirdly, chapter 6 expands the studies by IrO_2 as electrode material, influenced by different annealing gases. In addition, electrical field-induced chemical changes are explored.

The presented results in this chapter are taken from the published paper *"Enhanced Ferroelectric Polarization in TiN/HfO_2/TiN Capacitors by Interface Design"*: T. Szyjka, L. Baumgarten, T. Mittmann, Y. Matveyev, C. Schlueter, T. Mikolajick, U. Schroeder, and M. Müller, ACS Applied Electronic Materials 2, 3152 (2020) [64]. The HAXPES measurements and data analysis for this paper and all data representations and descriptions are done by me. The interpretation, literature research, and written text were done cooperatively.

Table 4.1.: Ti $2p_{3/2}$ binding energies for different Ti related chemical species.

	binding energy (eV)		
	experiment	literature	Ref.
TiN	455.4 ± 0.06	455.03 ± 0.05	[73]
TiN (shake-up)	457.6 ± 0.5	457.22± 0.05	[73]
TiN_xO_y	456.3 ± 0.14	455.4 – 456.7	[81]
TiO_2 crystalline	459.5	459.2	[82]
TiO_2 amorphous	458.8	458.7	[83]

This chapter explores the tunability of oxygen vacancies V_O concentration and chemical stability of $TiN/HfO_2/TiN$ capacitor structures as well as the correlation to the ferroelectric phase in HfO_2. For this, PVD as the deposition technique is used for all layers (see Table 3.1), ensuring the exclusion of contamination like carbon or nitrogen, which can act as a dopant. In addition, PVD offers a controlled variation of the growth parameters and stoichiometry of the layers. Here, the flow rate $\dot{m}$ of an additional oxygen flow supplied before and during growth of the HfO_2 layer is used (see section 3.1.1).
This chapter is divided into the description of the chemical properties of the bottom interface, ferroelectric interlayer, and the electrical characterization.

4.1. Bottom interface: TiN/HfO_2

The surface of all samples is structured in an array of circular contacts (see sec. 3.1 *Surface structuring*). During the surface structuring of the samples the top electrode is etched away between the contacts. The HAXPES experiments were performed on areas right in between the contacts (see Fig. 3.1). Therefore, no contributions from the top TiN electrodes are measured, and the data reflects the chemical properties of the HfO_2 layer and the bottom TiN/HfO_2 interface only. The following data presented were acquired at two different synchrotron facilities (DESY, BESSYII), where the beamline P22 (DESY) had slightly lower energy resolution than the beamline HIKE (BESSYII). This difference does not affect the results, but the spectra of samples grown at $\dot{m} = 0.25 - 1$ sccm O_2 flow (S025, S05, S1) will show up to 15% narrower peaks.
Before the deposition of the HfO_2 layer, the added oxygen flow was directed over the samples for 3 min in order to stabilize the flow, resulting in the oxidation of the amorphous, as-deposited TiN bottom electrode. The degree of oxidation depends on the oxygen flow rate and exposure time. In order to determine the chemical properties of the TiN/HfO_2 bottom interface, we recorded HAXPES spectra of the Ti 2p core-levels, which overlaps with the shake-up satellite of Hf $4p_{1/2}$ core-level (see sec. 3.2.2). The background-corrected and normalized Ti 2p core levels are shown in Fig. 4.1 a) - c).
Figure 4.1 a) features the fitted Ti 2p spectra of the samples grown at $\dot{m} = 0 - 2$ sccm and RTA-treated at 800°C, which have been normalized to the Ti $2p_{3/2}$ peak belonging to TiN ($E_{\text{bin}} = 455.4$ eV). Comparing this dataset, two major observations can be deduced:

1) The spectra of the sample with $\dot{m} = 2$ sccm O_2, annealed without top electrode (S2 without TE, black line), and the complementary sample with an etched top electrode (S2, red line) are similar in shape, confirming that the etching process completely removes the top electrode since a remaining top electrode on the surface would noticeably increase the Ti 2p intensity and could change the ratio between different contributions present (e.g., TiN, TiO_2). Thus the recorded photoelectron intensity only originates from the Ti of the bottom electrode.
2) All Ti 2p spectra show contributions of TiN, TiN_xO_y sub-oxides [75, 84] and TiO_2, whose Ti $2p_{3/2}$ peak positions are listed in Tab. 4.1. With increasing oxygen flow during growth a significant increase of the spectral weight of the TiO_2 component can be detected. In Figure 4.1 b) the Ti 2p spectra of S2, normalized to the Ti $2p_{3/2}$ core level of TiO_2, is compared for different electron emission angles. With the increasing angle, the signal intensity of TiN decreases, and the surface sensitivity of the HAXPES experiment increases, which places the location of the TiO_2 contributions on top of the TiN bottom layer. For S0, the TiO_2 layer has to form during the annealing process by scavenging the HfO_2 layer of O and potentially supplying N. Thus, at least for SO, Hf-N bonds at the interface could form. Figure 4.1 c) depicts the Ti 2p spectra of non-annealed samples grown at $\dot{m} = 2$ sccm, where the stabilization times of the oxygen flow *before* growth is varied from t=3 min to 10 s. The reduction of this time decreases the TiO_2 contributions, which shows that the TiO_2 interlayer primarily results from the oxygen flow prior to the HfO_2 deposition and not as a result of the annealing process. The TiO_2 peaks for the amorphous systems appear at lower binding energies than the corresponding annealed (thus crystallized) samples since the average bond lengths in amorphous TiO_2 are longer and weaker.
Taken together, the Ti 2p core-levels reveal a TiO_2 contribution on top of TiN which may be described by a two-layer model of the bottom electrode with a TiO_2 intralayer located between the TiN bottom electrode and HfO_2, which is very likely caused by the initial PVD growth procedure.
The fits of the Ti 2p core-level provide the spectral intensities I needed for quantifying the thickness of the TiO_2 interlayer. A two-layer model is used, ignoring any possible gradients between the layers as well as any incomplete layer formation of TiO_2, making any calculated thickness of the TiO_2 layer an effective layer thickness. Section 3.2.4 explains in detail how to determine this thickness. Using equ. (3.18) the effective thicknesses of the TiO_2 intralayers have been calculated and are plotted in Fig. 4.1 d). The description of the error calculation is given, and a complete table of all values used for the calculation is listed in the appendix A.4.1.
The relation between the oxygen flow and the effective layer thickness of TiO_2 shows a rapid increase for $\dot{m}<1$ sccm and a saturating behavior for $\dot{m}>1$ sccm. A self-limiting reaction process can explain this behavior: Increasing the TiO_2 intralayer thickness serves as a buffer for oxygen diffusion, protecting the TiN bottom electrode from further oxidation and blocking any oxygen scavenging from the HfO_2 layer, which might lead to an increased oxygen vacancy density at the interface.

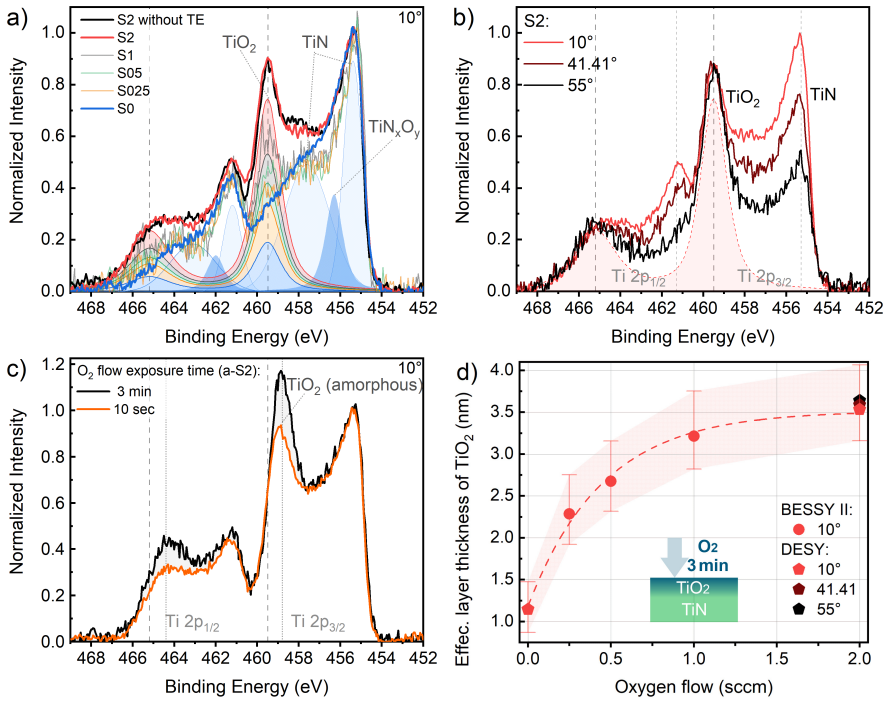

Figure 4.1.: HAXPES spectra of the Ti 2p core level: a) samples with different oxygen flow rates ($\dot{m}$=0-2 sccm) during the deposition (S0, S025, S05, S1, S2, S2 without TE); b) S2 at different emission angels (10° (bulk sensitive), 41.41°, 55° (surface sensitive)); c) Amorphous and non-annealed samples without top electrode and varying oxygen exposure time; d) Effective layer thickness of TiO_2 dependent on the oxygen flow before the HfO_2 deposition (see equ. (3.18)); Own images, published in ref. [64].

4.2. Ferroelectric HfO_2 interlayer

The idea to supply additional oxygen during HfO_2 deposition was intended to control the stoichiometry and oxygen vacancy concentration of the HfO_2 layer. The additionally observed oxidation of the TiN bottom electrode has to be kept in mind for the further interpretation of the properties of the HfO_2 layer. The HfO_2 layer was investigated by HAXPES spectra of the Hf 4f, Hf 4s, O 1s and N 1s core levels, respectively. Figure 4.2 a) depicts the Hf 4f core-level of the samples with the lowest (S0) and highest (S2) oxygen flow for two different electron emission angles ($\theta = 10°$ and $41.41°$), normalized to the Hf $4f_{5/2}$ peak. The binding energy of the Hf 4f core-level in the S0 spectra shows a distinct shift of $\Delta E \approx 110$ meV to higher energies compared to the S2 spectra.
For a shape comparison of the spectra, the S0 spectrum (higher binding energies) is shifted to fit S2. The insets of Fig. 4.2 a) use the shifted spectra and show a zoom of the space between the Hf peaks and of the lower binding energy flank of the Hf $4f_{7/2}$ peak. The visible signal differences are extracted by subtracting the shifted S0 spectrum from the S2 spectrum, revealing an additional double-peak structure at lower binding energies and with identical energy splitting as the Hf 4f doublet ($\Delta E = 1.65\,\text{eV} \pm 0.05\,\text{eV}$). In agreement with literature [85], this additional spectral contribution can be assigned to Hf^{3+}. In stoichiometric HfO_2 the valency of Hf is Hf^{4+}. In the context of the elements represented in the samples, *charged* oxygen vacancies and $Hf^{3+}N^{3-}$-bonds are valid explanations for the Hf^{3+} signal (see sec. 2.1.2). To determine the local origin of this signal, the spectra for different electron emission angles are compared (see dotted lines in Fig. 4.2 a)). On the one hand, the S2 sample does not show any notable difference, but on the other, the S0 shows a decrease of the Hf^{3+} contribution, with an increasing emission angle. This decrease in intensity indicates that the origin of the Hf^{3+} signal lies at the interface to the bottom electrode or at least has a depth-dependent gradient in the HfO_2 layer.
Figure 4.2 b) plots the extended spectra of the same two samples containing the O 1s, Hf 4s, and Ti 2s core levels, normalized to the signal intensity of the Hf 4s core level. Here the insets provide a zoom of the peak maxima and show a similar shift as in the Hf 4f core-level for the O 1s and Hf 4s core-levels. The binding energy of each peak is determined by a fit and is marked by a dotted straight line, respectively. In contrast to the O 1s and Hf 4s peaks, the spectral features originating from the TiN/TiO_2 electrode (Ti 2p, Ti 2s) do not show any rigid shift. Like the Ti 2p core level, the Ti 2s level also shows an explicit TiO_2 contribution for the S2 sample.
The O 1s core level from the S2 sample reveals an oxygen contribution of TiO_2 and a more significant one for HfO_2 in comparison to S0. Due to the additional O contribution in S2, a relatively higher V_O density can be assumed in the S0 sample compared to S2. Oxygen vacancies usually introduce vacancy states in the bandgap, shifting the Fermi level towards the conducting band, which results in higher binding energies in the spectra (see sec. 2.1.2). Relative to the S2 sample, the S0 sample has a rigid binding energy shift to higher energies in all HfO_2-related core levels. These rigid shifts can therefore be associated with a re-positioning of the Fermi-level due to the presence of oxygen vacancies in S0, which have been "doped" into the HfO_2 layer during PVD growth.

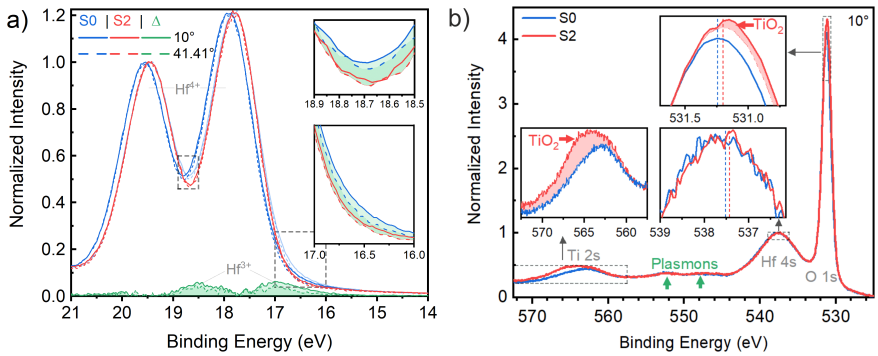

Figure 4.2.: a) Hf 4f HAXPES spectra of S0 (blue) and S2 (red) at 10° (bulk sensitive) and 41.41° emission angle (surface sensitive). The binding energy between the samples is shifted by $\Delta E \approx 110$ meV. Compensating the shift between S0 and S2 enables a shape comparison (S0-S2), revealing additional Hf peaks (green), which can be assigned to Hf-N (Hf^{3+}) bonds for S0. The inset shows the areas of interest with the numerically corrected spectra. The additional Hf^{3+} contribution decreases with increasing emission angle. Own images, published in ref. [64]. b) Extended HAXPES spectra containing the O 1s, Hf 4s and Ti 2s core level. The insets show zoom on the peak maxima, where dotted straight lines mark the binding energies, determined by fits. At the long-range background of the O 1s, and Hf 4s core levels, plasmon contributions are observable.

Since all parameters during the growth process of HfO_2 are unchanged, a uniform distribution of V_O can be assumed. This seems to contradict the gradient seen for the angle-dependent Hf^{3+} signal in the Hf 4f spectra, requiring additional causes for its source.

Figure 4.3 a) depicts the background-corrected (see sec. 3.2.2) and normalized N 1s HAXPES spectra recorded for S0 and S2. Both spectra show similar contributions of TiN (397.5 eV) and O-Ti-N (396.7 eV) compounds and peaks appearing at higher E_{bin} (398.3 eV, 399.3 eV) related to different molecular nitrogen species inherent to TiN and other transition metal nitrides [81, 86–89]. In addition, the S0 spectrum shows a peak at 396 eV, which can be assigned to the presence of Hf-N bonds [89, 90]. The inset shows the spectra of S025, S05, and S1 at the binding energy of Hf-N. With increasing oxygen flow (S025→S05→S1), the Hf-N contribution diminishes and disappears.

Figure 4.3 b) summarizes the findings of the TiN bottom electrode and HfO_2 layer schematically. The additional oxygen flow 3 min before the HfO_2 growth leads to the formation of a TiO_2 interlayer inhibiting the formation of HfN during RTA. As expected, the additional oxygen flow during the HfO_2 deposition leads to an overall reduction of oxygen vacancies. In the next step, we correlate the findings to the crystal structure and electrical characterization determined in the pre-characterization.

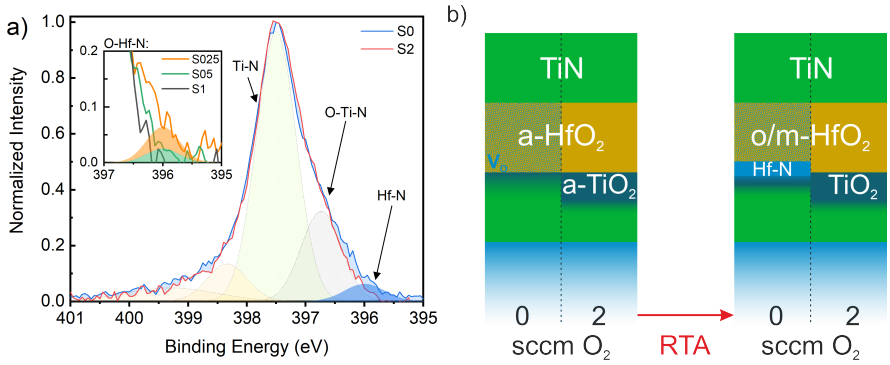

Figure 4.3.: a) N 1s HAXPES spectra with subtracted reference background of S0 (blue) and S2 (red) at 10° emission angle. Both spectra show similar contributions of TiN and O-Ti-N compounds. In addition, the S0 spectrum shows a peak at 396 eV (Hf-N). The inset shows the spectra of S025, S05, and S1 at the binding energy of Hf-N, where S1 shows no additional intensity. Own images, published in ref. [64]. b) Schematic representation of devices with different O_2 flow before and after RTA. The additional oxygen reduces the amount of V_O and inhibits the HfO_2 formation via a TiO_2 interlayer.

4.3. Electrical characterization

As described in section 3.1.2, all samples have been pre-characterized by GiXRD and electrical field switching experiments at NaMLab by Terence Mittmann. GiXRD is used to determine the crystal structure. Thus the ratio of the orthorhombic(/tetragonal) to monoclinic phase o/(o+m) can be calculated and is plotted over different oxygen flows in Fig. 4.4 a) [65]. A distinction between the orthorhombic and tetragonal phases is not possible since the signal in GiXRD overlap. For oxygen flows below 1 sccm, the HfO_2 layer is mainly orthorhombic(/tetragonal) and becomes more monoclinic with higher $\dot{m}$. Dynamic hysteresis measurements, as a particular form of electrical field switching experiment, with a maximum switching current of 3 V are performed on the HfO_2 capacitor structures to determine the ferroelectric hysteresis (see sec. 3.1.2). Figure 4.4 b) shows the double remanent polarisation $2P_r$ of S0, S05, and S1 depending on the number of cycles. Unlike S0 and S1, S05 has much higher $2P_r$ values and does not show a distinct wake-up phase. The S0 sample has the strongest wake-up phase in comparison. In part, the wake-up phase could be caused by local internal bias field due to V_O accumulation at the interfacial layer between the electrode and HfO_2 or domain walls (see sec. 2.1.3). The relationship between the wake-up phase and V_O concentration is consistent with the electrical characterization and the HAXPES experiment, which revealed the highest V_O concentration in S0. For further discussion the *Pristine* data ($n = 1$) and the data *after WakeUp* ($n = 10^5$) are compiled.
Figure 4.4 c) plots the respective $2P_r$ values over $\dot{m}$ showing a decrease for oxygen flow rates $\dot{m} \geq 0.75$ sccm, but an increase of $2P_r$ for $\dot{m} = 0 - 0.5$ sccm.

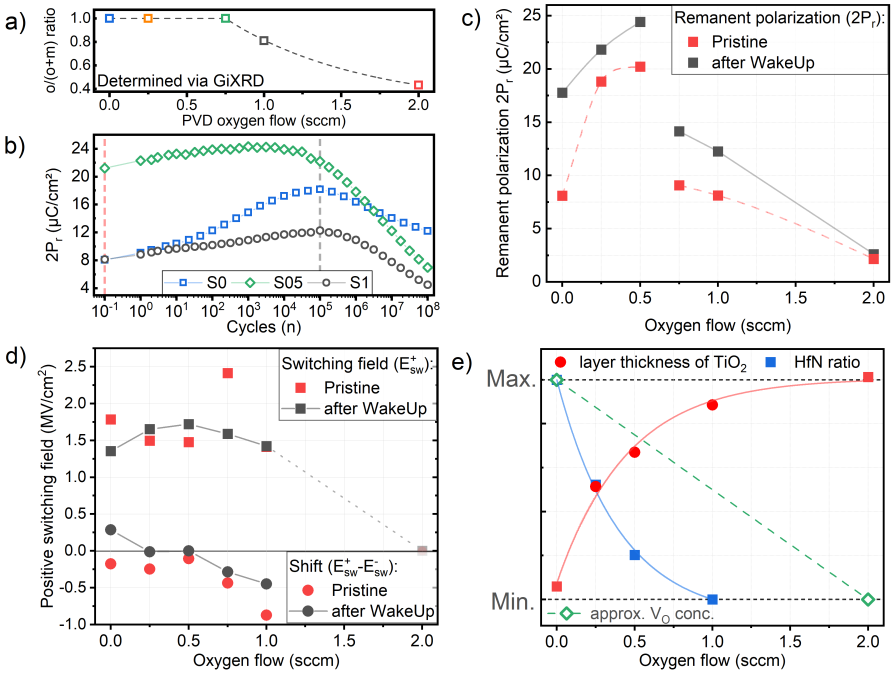

Figure 4.4.: a) The ratio of the orthorhombic to monoclinic phase o/(o+m) for samples with different oxygen flow determined by GiXRD. The GiXRD data are published in [65]. b) Double remanent polarisation $2P_r$ of S0, S05, and S1 depending on the cycles. The dotted red line marks the pristine datapoints, and the dotted black line marks the datapoints *after WakeUp* (10^5 cycles); c) Double remanent polarisation $2P_r$ of *Pristine* and *after WakeUp* data for different oxygen flows. d) Positive switching field and the asymmetry between positive and negative switching field of hystereses. e) Schematic summary of the HAXPES results: Saturating TiO_2 formation, reduction in HfN formation, and reduction of oxygen vacancies with increasing oxygen flow. The data points for the HfN-ratio are determined by comparing the changes in the HfN contribution at the N 1s core level. Fig. c)-e) are part of ref. [64].

The decreasing $2P_r$ values for $\dot{m} \geq 0.75$ sccm is in agreement with the GiXRD data, since the $2P_r$ value is inherently connected to the contribution of the ferroelectric orthorhombic phase. According to the HAXPES experiment, a continuous reduction of the V_O concentration with increasing oxygen can be assumed. Since oxygen vacancies are seen as a possible way to stabilize the othorhombic phase (see sec. 2.1.2), a reduction in V_O should destabilize the ferroelectric orthorhombic HfO_2 phase and thus in turn lead to lower $2P_r$ values [65]. Even for $\dot{m} = 0 - 0.5$ sccm a reduction in $2P_r$ is expected, if only V_O are to be taken into account. Therefore the increase of $2P_r$ for $\dot{m} = 0 - 0.5$ sccm needs another explanation.
Figure 4.4 d) shows the values of the positive switching field E_{SW}^{+} and the asymmetry between positive and negative switching field calculated by equ. (3.8): $E_{SW}^{+} - E_{SW}^{-}$. The asymmetry in the switching field (*after WakeUp*) changes its sign at approximately $\dot{m} = 0.5$ sccm from positive to negative, indicating the presence of an internal electrostatic field, which changes its polarity depending on the oxygen flow. This bias field is likely caused by a difference between the interfaces at the top and bottom electrodes.
The interface between the top electrode and the HfO_2 layer could not be studied by HAXPES. However, it can be assumed that all samples have a similar interface at the top electrode since no additional O_2 flow is used during the deposition of the top electrode. Without oxygen flow, the interface at the bottom electrode contains TiO_2 and Hf-N bonds, created during the annealing process. With increasing oxygen flow, the interface changes to a saturated TiO_2 layer. The different interfaces at the bottom electrode and the assumed similar interfaces at the top electrode fit the asymmetry seen in the switching field.
For a final comparison between chemical and electrical characterization, a schematic summary of the HAXPES results is depicted in Fig. 4.4 e). The reduction of oxygen vacancies are in line with the decrease of $2P_r$ at higher oxygen flow and the increase of $2P_r$ for $\dot{m} = 0 - 0.5$ sccm coincide with the growth of the TiO_2 layer and reduction of HfN formation.

In summary, chapter 4 revealed the interface formation between ferroelectric PVD-sputtered HfO_2 and TiN bottom electrode and how an additional oxygen supply reduces the oxygen vacancy concentration. In addition, the effects of oxygen vacancies on the ferroelectric properties and the representation of charged V_O in the HAXPES spectra have been shown. The following chapter draws a comparison between samples with PVD-sputtered HfO_2 and ones with ALD-formed HfO_2.

CHAPTER 5

II. Various types of oxygen vacancies

The presented results in this chapter are taken from the published paper *"Impact of vacancies and impurities on ferroelectricity in PVD- and ALD-grown HfO_2 films"*: L. Baum -garten, T. Szyjka, T. Mittmann, M. Materano, Y. Matveyev, C. Schlueter, T. Mikolajick, U. Schroeder, and M. Müller, Applied Physics Letters 118, 032903 (2021) [66]. All measurements and data analysis for this paper and all data representations and descriptions are done by me. The interpretation, literature research, and written text were done cooperatively.

Atomic layer deposition (ALD) is a widely employed growth process enabling thickness control down to single atomic layers at relatively low deposition temperatures. Unlike PVD deposited layer, growing thin films with ALD can introduce many impurities like carbon or nitrogen, altering the chemical and electrical properties. In this chapter, HfO_2 layer systems grown with ALD are compared to those deposited by PVD as previously presented.

5.1. Key parameters and pre-characterization

Except for the HfO_2 layer, the PVD and ALD sample sets were fabricated similarly. Especially the electrodes were deposited using the same process parameters during PVD. The critical parameters in the differently fabricated HfO_2 layer are depicted in Fig. 5.1 a). Where an additional oxygen flow controlled the properties for the PVD sample set, the ALD one uses different exposure times of the reactant gas O_3 ($ALD_{10\,s}$, $ALD_{60\,s}$). Similar to the oxygen flow in PVD, the idea behind different exposure times was to influence the V_O concentration. But unlike the PVD case, it is not intuitively clear if a longer O_3 exposure time increases or decreases the oxygen content in the HfO_2 layer since the role of the reactant O_3 is twofold, breaking up the precursor molecule and providing

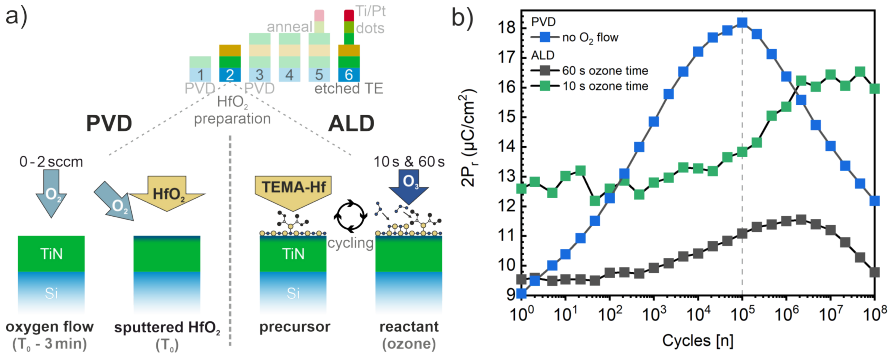

Figure 5.1.: a) Process schematics for PVD and ALD deposition of ferroelectric HfO_2 in $TiN/HfO_2/TiN$ capacitors: (Left) Using PVD, HfO_2 is sputtered in an additional oxygen flow of $\dot{m} = 0$ or 2 sccm, respectively. (Right) Using ALD, layer-by-layer growth of HfO_2 is accomplished by an alternating supply (cycling) of TEMA-Hf as the precursor and reactive ozone as the reactant, applying pulse times of $t_{O_3} = 10$ and 60 s, respectively. b) Electric field cycling behaviour of $TiN/HfO_2/TiN$ capacitors, showing the double remanent polarization $2P_r$ of $ALD_{10\,s}$, $ALD_{60\,s}$ and PVD_{0sccm} samples, which vanishes for PVD_{2sccm} to $2P_r = 0$. Own images, published in ref. [66]

the oxygen for HfO_2. The pre-characterization done by NaMLab reveals that both ALD samples show ferroelectric properties but have an essentially have a different endurance behaviour (see Fig. 5.1 b)): Whereas the PVD_{0sccm} sample reveals a pronounced increase of the remanent ferroelectric polarisation $2P_r$ during wake-up, both ALD samples show only a minor increase and a smaller slope of the $2P_r$ curves. The electrical measurements hint at stronger ferroelectricity in the ALD_{10s} sample, fitting to the GiXRD data, which show more significant orthorhombic contribution for ALD_{10s} than ALD_{60s} (see Tab. 5.1).

Table 5.1.: Phase ratio o/(o+m) determined by GiXRD.

	PVD_{0sccm}	PVD_{2sccm}	ALD_{10s}	ALD_{60s}
o/(o+m)	1	0.43	0.86	0.51

To explain the differences in the electric properties, a microscopic analysis is needed. In the following the HAXPES measurements of the PVD- and ALD-sample set will be compared, classifying the similarities and differences of the samples sets.

5.2. Classification of the ALD samples with HAXPES

All bottom electrodes are deposited by PVD in a vacuum chamber. To deposit a HfO_2 layer with ALD, this vacuum has to be broken. In the studied ALD samples, the bottom electrode was exposed to air for at least 24 h before the growth of HfO_2.
Figure 5.2 a) shows the HAXPES spectra of the Ti 2p core levels for PVD- and ALD-grown samples, whose binding energies are identical. An enhanced interfacial TiO_2 formation is observed for both ALD samples as well as for PVD_{2sccm}.With the results from the previous chapter 4 in mind, it is reasonable to assume that the oxidation of the bottom electrode at $ALD_{10\,s}$ and $ALD_{60\,s}$ is in the saturated regime, forming a $\sim$3.5($\pm$0.5) nm thick TiO_2 interlayer, which inhibits an intermixing during the annealing process.
Figure 5.2 b) depicts the HAXPES spectra of the Hf 4f core levels, normalized to the Hf $4f_{5/2}$ peak maximum. A relative energy shift to lower binding energies is evident between the $PVD_{0,2sccm}$ and $ALD_{10,60\,s}$ samples (see Tab. 5.2). The $ALD_{60\,s}$ spectrum shows, in comparison to the other samples' spectra, the lowest signal intensity in the valley between the Hf 4f peaks, which is unchanged for different emission angles (see Fig. 5.2 d)). The binding energy of the valley matches the Hf^{3+} contribution of the Hf $4f_{5/2}$ state, as seen in the previous chapter. Thus no or a negligible Hf^{3+} contribution for $ALD_{60\,s}$ can be assumed. For a shape comparison of the spectra, the $ALD_{60\,s}$ spectrum was used as a reference, shifted to fit the other spectra, and subtracted, respectively. The differences were fitted for a quantitative analysis. The fit of the differences can be seen in Figure 5.2 b) as shaded areas corresponding to Hf^{3+} components present in the $PVD_{0,2sccm}$ samples and less pronounced in $ALD_{10\,s}$. As in the PVD samples, the Hf^{3+} signal in the $ALD_{10\,s}$ spectra decreases with increasing emission angle (see Fig. 5.2 c)). The intensity ratios of Hf 4f, i.e. Hf^{3+}/Hf^{4+} obtained by the fits can be seen in Tab. 5.2. Other core levels directly assigned to the HfO_2 layer are O 1s, and Hf 4s. The related spectra, background-subtracted and normalized to Hf 4s are plotted in Figure 5.3 a). Both core levels show a similar shift as present at the Hf 4f core level (see Tab. 5.2).

Table 5.2.: Binding energies in eV of the Hf $4f_{7/2}$, and O 1s peak positions in Fig. 5.2, with peak shifts ΔE_{bin} relative to the PVD_{0sccm} binding energies. The binding energy of Hf $4f_{5/2}$ (Hf 4s) are 1.66 eV (6.2 eV) higher than the respective Hf $4f_{7/2}$ (O 1s) peak. In addition, the area ratio of Hf 4f:Hf^{3+}/Hf^{4+} and O 1s/Hf 4s is presented.

	Hf^{4+} $4f_{7/2}$	ΔE_{bin}	Hf^{3+}/Hf^{4+}	O 1s	ΔE_{bin}	O 1s/Hf 4s
$PVD_{0\,sccm}$	17.91	-	6.2%	531.23	-	1.64
$PVD_{2\,sccm}$	17.80	0.11	2.7%	531.17	0.06	1.73
$ALD_{60\,s}$	17.69	0.22	0.0%	531.13	0.10	1.81
$ALD_{10\,s}$	17.64	0.27	0.8%	531.04	0.19	1.89

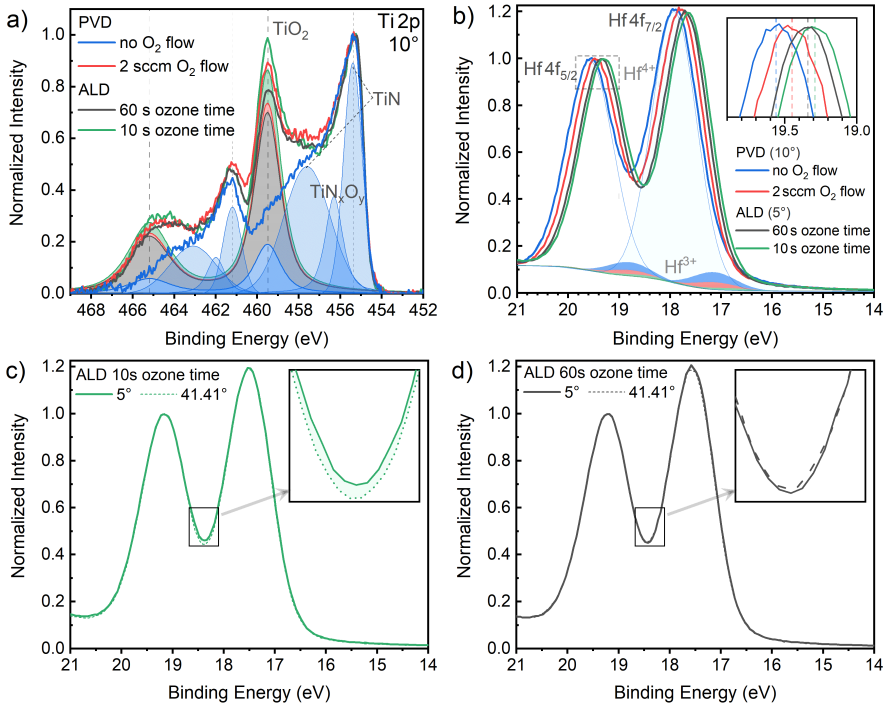

Figure 5.2.: **a)** HAXPES spectra of the Ti 2p core levels for PVD- and ALD-grown samples. An extended interfacial TiO_2 formation is observed for both $ALD_{10\,s}$ and $ALD_{60\,s}$ samples as well as for PVD_{2sccm}, but not for the PVD_{0sccm} sample. The TiO_2 serves as a chemical buffer between the HfO_2 and TiN bottom electrode. **b)** HAXPES spectra of the Hf 4f core levels for PVD- and ALD-grown samples. The $PVD_{0,2sccm}$ samples are energetically shifted relative to the $ALD_{10,60\,s}$ samples. Shaded areas ∼0.77 eV lower than the main Hf peaks correspond to Hf^{3+} components present in the $PVD_{0,2sccm}$ samples. Own images, published in ref. [66]; c) and d) show the Hf 4f core level for the ALD-samples recorded at 5° and 41.41° photoelectron emission angles.

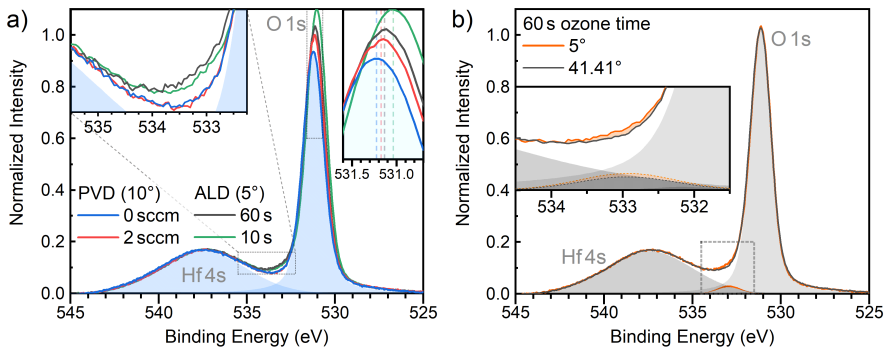

Figure 5.3.: a) Normalized HAXPES spectra of the Hf 4s and O 1s core levels for PVD- and ALD-grown samples. (Inset, upper left) The valley region between the Hf 4s, and O 1s core level reveals larger intensity for the ALD samples. (Inset, upper right) The peak maximum of the O 1s core level varies for either PVD or ALD-grown samples, respectively.**b)** ALD-grown sample with 60 s ozone time recorded at 5° and 41.41° photoelectron emission angles. The inset expands the area between the Hf 4s, and O 1s core level and captures the fit of this area, showing a decrease in intensity at 533 eV. Own images, published in ref. [66].

In the PVD samples the shift to lower binding energy was accompanied by a relative increase of the O 1s peak intensities and associated to a reduction of oxygen vacancies. The correlation of shifts and oxygen content also extends to the ALD samples so that the increasing intensity ratio O 1s/Hf 4s follows the decreasing binding energies (see Tab. 5.2): $PVD_{0sccm} \rightarrow PVD_{2sccm} \rightarrow ALD_{60\,s} \rightarrow ALD_{10\,s}$. The intensity ratio O 1s/Hf 4s also shows that the shorter exposure time in the $ALD_{10\,s}$ sample leads to a higher oxygen content.

A shape comparison of the O 1s spectra between $PVD_{0,2sccm}$ and $ALD_{10,60s}$ reveals an additional contributions at 533 eV for the ALD samples (see inset of Fig. 5.3 a)). The binding energy of this feature is around 1.8 eV higher than the main O 1s peak, which makes it likely to be a signature of oxide ions, which are characterized by a lower electron density than the classical O^{2-} ions. Studies showed such "O^{1-}" feature in transition metal oxides, including HfO_2, when oxygen vacancies are present [91–93]. One can argue that removing an oxygen ion from its lattice site forces the surrounding ions into new stable positions, which will have slightly different bond lengths and thus different covalence of the bonds. Hf-O bonds with higher covalence could include oxygen ions characterized by lower electron density and be detected as the "O^{1-}" feature. The exact implementation of the "O^{1-}" ion in the lattice is still an open question.
For the ALD samples, this feature is seen as an indicator of oxygen vacancies. In order to identify the local origin of this feature, angle measurements at 5° and 41.41° were taken. Figure 5.3 b) plots the Hf 4s-/O 1s-core level spectra of $ALD_{60\,s}$ for both angles and has an inset which expands the area between the Hf 4s, and O 1s core level. A small

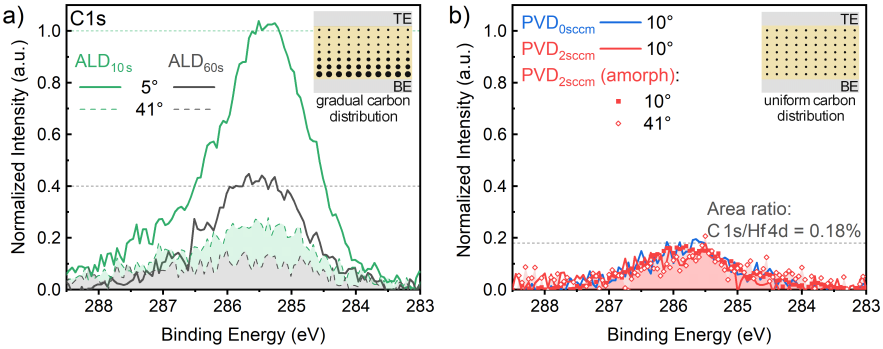

Figure 5.4.: HAXPES spectra of the C 1s core levels for a) ALD- and b) PVD-grown samples. The C content in ALD samples depends on ozone dosage and emission angle. At the higher angle, the signal is reduced by 2/3, which can be explained by a gradually increasing C content towards the bottom TiN interface. The PVD samples show only a very small, uniformly distributed and growth-independent amount of C impurities. Own images, published in ref. [66].

reduction of the signal is visible for the 41.41° measurement, which is more surface sensitive. The spectra are fitted using a Gaussian function for the Hf 4f core level as well as for the contribution in the area between the core levels. For the O 1s core level, a linear combination of Gaussian and Lorentzian functions was used. Only the contribution in the valley area between the two main peaks changes with photoelectron emission angle. The reduction in its intensity can be quantified to $I_{41.41°}/I_{5°}$=80%, indicating a gradient and a slightly enhanced defect concentration at the bottom electrode. For the $ALD_{10\,s}$ sample (not shown), this reduction can not be confirmed, which may be due to the larger O 1s peak compared to ALD_{60s}, overshadowing a possible angle-difference in the feature at 533 eV.

The existence of a possible vacancy gradient in the ALD samples can be explained by an increasing layer quality during the ALD process. At the beginning of the ALD process, HfO_2 is grown onto TiN/TiO_2, which is not the optimal starting point.

Not completely purged precursor molecules ($[(CH_3)(C_2H_5)N]_4Hf$) can contribute impurities like C and N, but also H. Figure 5.4 a) and b) depict the HAXPES spectra of the C 1s core level normalized to the neighbouring Hf 4d core-levels (not shown) recorded at two different photoelectron emission angles. The C content in ALD samples a) decreases with increasing ozone time by 60% and the signal intensity at higher angles is reduced by 2/3. The angle dependence demonstrate a higher carbon concentration at the interface to the bottom electrode. The PVD samples b) only show a marginal carbon concentration with homogeneous distribution which most possibly stems from the residual atmosphere in the PVD vacuum chamber.

Figure 5.5 a) and b) depict the HAXPES spectra of the N 1s core level normalized to the Hf $4p_{3/2}$ core-level (not shown) for the ALD- and PVD-samples. The N1s spectra

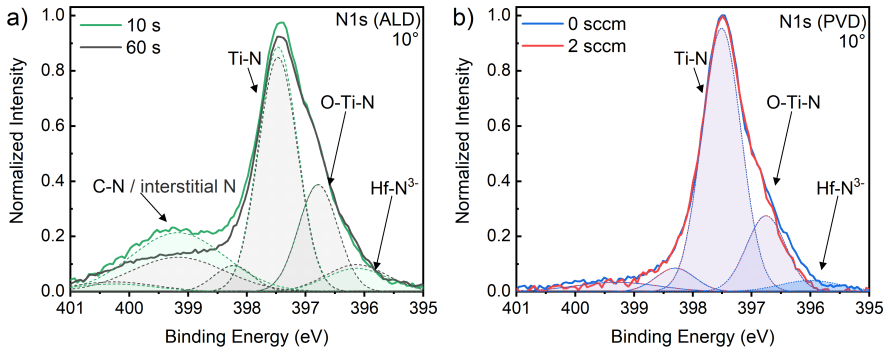

Figure 5.5.: HAXPES spectra of the N 1s core levels for a) ALD- and b) PVD-grown samples, dominated by Ti-N contribution from the bottom electrode and O-Ti-N contribution from the TiN/HfO_2 interface. Hf-N contributions are observed for all samples but PVD_{2sccm}. In ALD samples, C-N or interstitial N decreases with increasing ozone dose, as does the corresponding C 1s spectra in Fig. 5.4 a). Own images, published in ref. [66].

were fitted by Gaussian functions. In total, three different N contributions can be distinguished, which originate from C-N, from Ti-N related compounds, as well as from Hf-N^{3-} bonds. The most dominated peaks refer to the Ti-N contribution from the bottom electrode and O-Ti-N contribution from the TiN/HfO_2 interface [64]. The broad emission around E_{bin} = 399 eV is related to C-N bonds and possibly to interstitial nitrogen contributions [94, 95] and the peak shoulder at E_{bin} = 396 eV can be assigned to the Hf-N coordination [96]. In the ALD samples, the Hf-N can not stem from an intermixing at the bottom electrode due to the preexisting TiO_2 interlayer and presumably originate from the precursor used for the HfO_2 layer, which already contains chemical bonds between Hf and N. The different origins of Hf-N bonds in PVD and ALD can potentially affect the local N concentration and the character of the bond, e.g., more Hf^{3+}-N^{3+}-like or Hf^{4+}-N^{3+}-like (e.g., VN_2-complex). Noteworthy, the C-N feature in the ALD samples shows a similar reduction with increasing ozone time as seen at the C 1s core level, but the Hf-N^{3-} contributions remains nearly unchanged similar to the "O^{1-}" contribution found at the O 1s core level. The difference in C and N indicates different strengths between the bonds of Hf-N and N-C in the precursor molecule.

5.3. Comparison of the electrical and chemical properties

In the following, the HAXPES results will be summarized and linked to the electric field cycling experiment. The PVD_{2sccm} and ALD_{10s} samples show the largest $2P_r$ values after wake-up and the largest o/(o+m) ratio. As shown in the previous chapter, V_O are a key factor for the stabilization of the ferroelectric phase in the PVD samples.
The PVD-ALD comparison reveal for the ALD samples an increase in impurities (C, N) and a decrease in Hf^{3+} signal, which is an indicator for charged vacancies. This reduction in combination with an increased O to Hf ration found in ALD suggests a V_O reduction. Nevertheless the $ALD_{10,60s}$ show a O^{1-}-feature, not found in $PVD_{0,2sccm}$, which can be seen as an indication for V_O. This discrepancy can be explained by the formation of VN_2 in $ALD_{10,60s}$, making charged V_O possible without a Hf^{3+} signal (see Fig. 2.6). The VN_2 can also in part explain the binding energy shifts found in the core-levels related to the HfO_2 layer. Those shift are similar for all core-level and thus correlate with the position of the Fermi-level. From high to low E_{bin} the order of the shifts are: PVD_{0sccm} $\rightarrow$$PVD_{2sccm}$ $\rightarrow$ $ALD_{60\,s}$ $\rightarrow$$ALD_{10\,s}$. As described in section 2.1.2 *Vacancy states in HfO_2*, O vacancies lead to a shift of the Fermi level towards the CB and thus to higher binding energies. The reduction of V_O from PVD_{0sccm} to PVD_{2sccm} reduces the shift of the Fermi level and the binding energies. The shifts to lower E_{bin}, detected in the ALD samples, can be explained by a further reduction in the V_O concentration, which can be concluded from the decreased Hf^{3+} component at the Hf 4f core level and from the increased O 1s/Hf 4s ratio. Among the ALD samples it is not totally clear which sample has the lower V_O concentration, since ALD_{10s} has some remaining Hf^{3+} contributions but although the highest O 1s/Hf 4s ratio. In both ALD samples N supports the formation of VN_2, which passivates any existing vacancy states and leads to a shift further away from the CB. The C 1s and N 1s core-levels show higher C and N concentrations in ALD_{10s} compared to ALD_{60s}, which can explain that the lowest binding energies of HfO_2 related core-levels are found for ALD_{10s}. The GiXRD measurements show a higher content of the orthorhombic phase in ALD_{10s} (86%) compared to ALD_{60s} (51%). It has been argued that C impurities can stabilize the ferroelectric HfO_2 phase [95] and it has been shown that N as an anion dopant stabilizes the ferroelectric HfO_2 phase [39, 97]. In this context, the GiXRD data match the difference found in the C and N concentrations in the ALD samples. It is an open question how C is built into the lattice. Indications are given by the C-N peak at N 1s and a lack of Hf-C signal in C 1s, which should be located at $\approx$282.5 eV [98]. Figure 5.6 recapitulates the key findings of the HAXPES measurements. Where oxygen vacancies seem to be a key component in the stabilization of the ferroelectric phase in PVD, but in ALD, the impurities seem to take this role.
The same impurities can also potentially explain the different behavior for the remanent ferroelectric polarisation $2P_r$ during electrical field cycling, whereas PVD_{0sccm} reveals a pronounced increase of $2P_r$ during wake-up, both ALD samples show a delayed and reduced wake-up phase.
The wake-up phase is essentially characterized by the mobility of oxygen vacancies under the application of an electric field (see sec. 2.1.3). The VN_2-complex in $ALD_{10,60s}$ has a

stable closed-shell character with N impurities forming a chemical bond to the oxygen vacancy, which should result in a decreased mobility compared to vacancies V_0 in PVD-grown samples [29]. This assumption fits with the delayed and reduced wake-up phase in ALD compared to PVD samples.

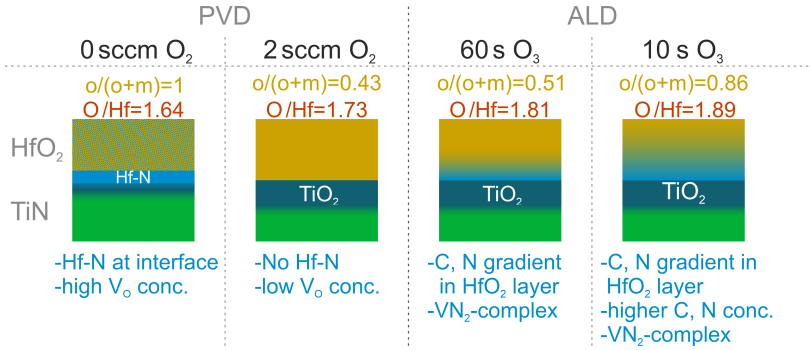

Figure 5.6.: Schematic representation of the HAXPES results. The key parameter for the PVD samples is the additional oxygen supplied during the deposition of the HfO_2 layer. In the case of ALD, the critical factor is the O_3 time during HfO_2 layer growth.

CHAPTER 6

III. Annealing gas and electrical field induced chemical changes

The presented results in this chapter are taken from the published paper *"Chemical Stability of IrO_2 Top Electrodes in Ferroelectric HZO-Based Metal–Insulator–Metal Structures: The Impact of Annealing Gas"*: T. Szyjka, L. Baumgarten, T. Mittmann, Y. Matveyev, C. Schlueter, T. Mikolajick, U. Schroeder, and M. Müller, physica status solidi (RRL) – Rapid Research Letters 15, 2100027 (2021) [68]. All HAXPES measurements and data analysis for this paper and all data representations and descriptions are done by me. The interpretation, literature research, and written text were done cooperatively.

The two previous chapters focused mainly on the ferroelectric layer but also showed that the interface between the electrodes and the ferroelectric layer play an essential role in the chemical and electrical properties. The N and O exchange detected in the PVD samples showed that TiN electrodes can scavenge O from HfO_2 and increase the V_O concentration locally. Using an oxide electrode material like IrO_2 instead of TiN has the potential to be an O donor for HfO_2 and thus be an option for V_O reduction at the interfaces. For ferroelectric perovskite material $Pb(Zr_xTi_{1-x})O_3$, the use of IrO_2 as electrode material has shown the potential to increase the ferroelectric performance [99, 100].
This chapter investigates the third sample set with IrO_2/HZO/IrO_2 as the general layer structure, where PVD is used for the IrO_2 electrodes and ALD for the ferroelectric HZO layer (see sec. 3.1.1). The top electrode of the samples has a layer thickness of 20 nm, and is deposited via a shadow mask, structuring the surface without the requirement of any additional Pt deposition and etching process, like in the case of TiN. In addition to the known dot array, a larger rectangular area ($\sim 1\,cm^2$) of the HZO-layer is covered by the IrO_2 top electrode (see pictures in Fig. 6.1). The parameter changed in this sample

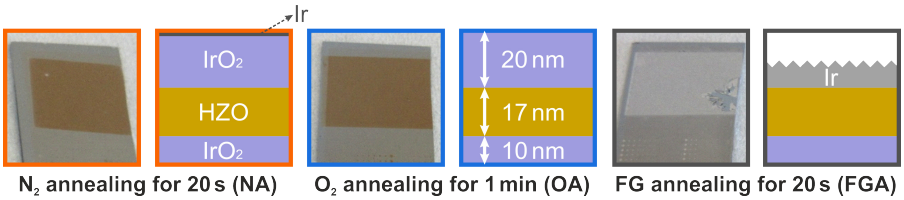

Figure 6.1.: Pictures of $IrO_2/Hf_{0.5}Zr_{0.5}O_2/IrO_2$ samples after rapid thermal annealing (RTA) at 500°C in different gas atmospheres (N_2, O_2, and forming gas (FG)). The squares visible in the pictures are the IrO_2 top electrode. Optical inspections reveal significant chemical modifications of the IrO_2 top electrode for the FGA sample. HAXPES data reveals the chemical state of the respective samples and are schematically presented.

set is the atmospheric gas used during the annealing process at 500°C (O_2, N_2, forming gas: N_2:H_2 mixture in a 9:1 ratio). Nitrogen is a typical gas used to avoid chemical reactions during the annealing process due to its inert character. In contrast, an oxygen atmosphere can improve the oxidation state of unstable oxides or not completely oxidized layers [101]. Annealing under forming gas atmosphere is an inevitable process for Si-based memory devices to achieve appropriate transistor performance [4]. Thus it is essential to understand the effects forming gas has on HfO_2-based ferroelectric MIM structures.
It is important to note that all three samples origin from one piece and were separated before annealing. Thus all measured changes can be traced back to the annealing process. Figure 6.1 shows pictures taken from the different samples as well as a schematic of the layer structure, determined by the HAXPES measurements. The optical inspection of the top electrodes reveals a color change from brownish to grey, comparing the nitrogen and oxygen annealed samples (NA & OA) to the forming gas annealed one (FGA).

6.1. Classification of the top electrode

Already the optical inspection shows significant changes in the top electrode if different annealing gases are used. In order to quantify the exact changes, the Ir 4f, and Ir 5p core levels are studied in more detail. Figure 6.2 a) shows a HAXPES overview spectra of the FGA, NA, and OA samples, ranging from the Ir 4f, and Ir 5p core level up to E_F, including the Hf 4f core-level. All spectra are normalized to the integrated signal of the Ir core levels. Since all three samples are from one original piece, the absolute Ir content is the same. The normalization by the area of the Ir core levels enables a direct comparison of any changes in the top electrode.
The Ir peaks at 49.2 eV (NA,OA) and 48.2 eV (FGA) belong to Ir $5p_{3/2}$. The Ir $5p_{1/2}$ state overlaps with the Ir 4f core-level and has a binding energy which lays between the peaks of Ir 4f. According to reference [102] the doublet separation of Ir 4f is 3 eV and of Ir 5p is 15 eV.

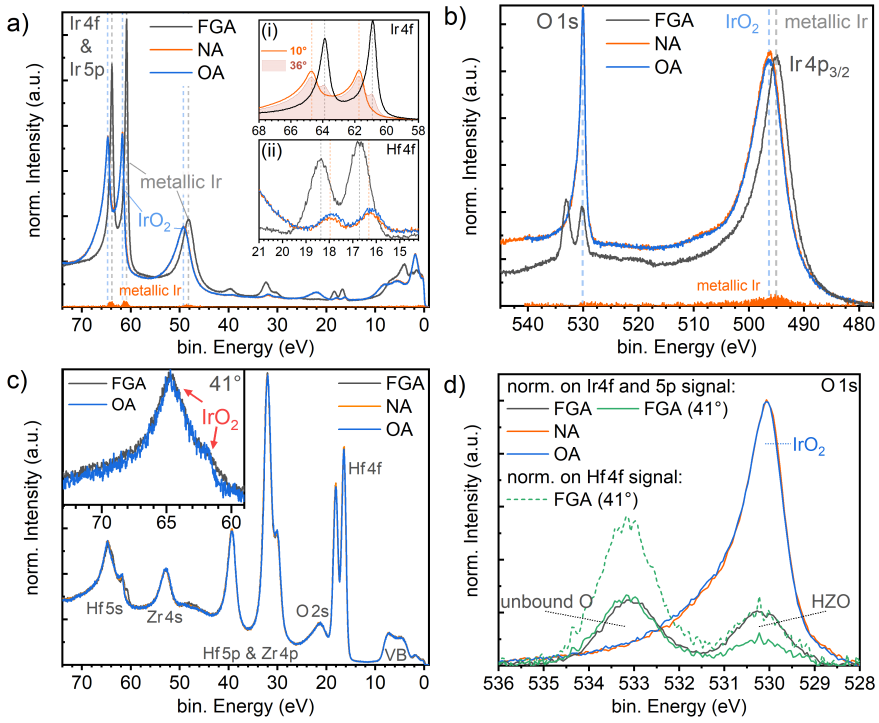

Figure 6.2.: a) HAXPES overview spectra of FGA, NA, and OA, ranging from the Ir 4f, and Ir 5p core level up to E_F, including the Hf 4f core-level. All spectra are normalized to the integrated signal of the Ir core levels. To work out the differences between NA and OA, the NA spectrum was subtracted by the OA one yielding the metallic Ir proportions (see shaded orange areas in Fig. 6.2 a)&b)). (i) Zoom into the Ir 4f core level of FGA and NA samples including an additional surface-sensitive angle measurement (36°) of NA (filled area). (ii) Expansion of Hf 4f peaks. The binding energy of the Hf 4f peaks of FGA is shifted by 400 meV compared to NA and OA, respectively. b) HAXPES spectra of the Ir $4p_{3/2}$ and O 1s core levels. NA also shows the metallic component in the Ir $4p_{3/2}$ core level. c) HAXPES overview spectra of all samples without top electrode. The inset shows the Hf 5s core level with the overlapping signal from the IrO_2 bottom electrode from FGA and OA at 41° emission angle. d) Background subtracted HAXPES O 1s spectra of FGA, NA, and OA, measured at an emission angle of 10°. In addition a surface-sensitive measurement of the FGA sample is shown (green line). The spectra are normalized to the integrated signal of the Ir 4f and Ir 5p core level. In addition the surface-sensitive measurement of FGA is also plotted normalized to the Hf 4f signal. Own images, a) and d) are published in ref. [68].

With this knowledge the E_{bin} of Ir $5p_{1/2}$ can be determined relative to Ir $5p_{3/2}$.
Table 6.1 lists the E_{bin} of the Ir 4f and Ir 5p peak positions and Ir $4f_{7/2}$ reference values of Ir and IrO_2. The comparison with the literature values shows that in the case of FG annealing, the IrO_2 is reduced to pure Ir. NA and OA spectra reveal the typical peak shape and binding energy position of the expected IrO_2. In addition, the NA spectrum shows an Ir component, which can be extracted by calculating the difference spectra between NA and OA (see shaded orange area). The inset (i) in Figure 6.2 a) shows the FGA and the NA spectra of the Ir 4f core level for two different emission angles. The more surface-sensitive measurement (36°) of NA shows an increase in the Ir component, revealing that this metallic component is located on top of the IrO_2 top electrode. An estimation of the thickness of this Ir layer results in a coverage of one monolayer or less. These findings are in complete agreement with the experiments done and published by Heikkilä et al. [103], where the annealing of IrO_2 thin films under different conditions was investigated. In this study, it was found that IrO_2 thin films annealed in an oxygen atmosphere at temperatures up to 1000°C are chemically stable, while annealing in N_2 and temperatures above 500°C lead to a decomposition of the IrO_2 into metallic Ir. In vacuum or FG annealed samples showed such reduction already at 250°C.
The reduction from IrO_2 to Ir in FGA, also results in a reduction of the film thickness of the top electrode. Assuming that the Ir content remains constant during the reduction, the altered film thickness can be estimated by:

$$d_{\mathrm{IrO_2}}\frac{\rho_{\mathrm{IrO_2}}}{F_{\mathrm{IrO_2}}} = d_{\mathrm{Ir}}\frac{\rho_{\mathrm{Ir}}}{F_{\mathrm{Ir}}} \quad \Leftrightarrow \quad \frac{d_{\mathrm{Ir}}}{d_{\mathrm{IrO_2}}} = \frac{\rho_{\mathrm{IrO_2}}/F_{\mathrm{IrO_2}}}{\rho_{\mathrm{Ir}}/F_{\mathrm{Ir}}}\,. \tag{6.1}$$

Here d_x is the film thickness, ρ_x is the density, and F_x is the formula weight of each material, respectively. For the IrO_2 top electrode a density of $\rho_{\mathrm{IrO_2}} = 12.61\,\mathrm{g/cm^3}$ could determined via XRR. Together with a literature values for the density of an Ir layer $\rho_{\mathrm{Ir}} = 22.56\,\mathrm{g/cm^3}$ [104], the reduction in layer thickness can be estimated as 52% ($d_{\mathrm{Ir}}/d_{\mathrm{IrO_2}}$=48%). With a reduced top electrode thickness the signal of the HZO beneath is less attenuated. This can directly be observed in the inset (ii) in Figure 6.2 a), which depicts the spectra of the Hf 4f core level, showing a significantly stronger signal and a rigid binding energy shift of 400 meV for FGA compared to NA and OA.
To complete the classification of the top electrode, the oxygen-related features are discussed. Figure 6.2 b) depicts overview spectra containing the O 1s and Ir $4p_{3/2}$ core levels, normalized by the same factor used in Fig. 6.2 a). To properly compare the O 1s component, the background of the spectra are subtracted and the result is plotted in

Table 6.1.: Binding energies in eV of the Ir 4f and Ir 5p peak positions in Fig. 6.2. The values of the $5p_{1/2}$ state are calculated using the $5p_{1/2}$ state and Δ5p from ref. [102].

	$4f_{7/2}$	$4f_{5/2}$	Δ4f	$5p_{3/2}$	$5p_{1/2}$	Δ5p [102]		$4f_{7/2}$ [102]
FGA	60.9	63.9	3	48.2	*63.2*	15	Ir	60.8
NA (OA)	61.7	64.7	3	49.2	*64.2*	15	IrO_2	61.9
FGA-NA	0.8	0.8		1	1			1.1

Figure 6.2 d). NA and OA display a strong O 1s emission originating from the IrO_2 top electrode, overlapping with any remaining signal from the HZO layer. The O 1s spectrum of FGA has two distinct components at 530.25 eV and 533.15 eV. The peak at 530.25 eV can be identified as the signal from HZO due to a 41° measurement, showing a signal decrease and locating the signal below the top electrode. In addition, more surface sensitive measurement at higher angle was normalized to the Hf 4f intensity, showing matching intensity to the 10° measurement. The contribution at higher binding energies shows a signal increase with increasing emission angle, locating its origin in the Ir layer. Novotny et al. [105] studied the oxidation of a pure Ir film and could show that prior to the formation of IrO_2, oxygen can exist in the Ir film in an unbound state. A certain threshold of O concentration has to be reached to form IrO_2. For the reduction of IrO_2 by forming gas, a reversed process is proposed, leading to unbound O, dissolved in the Ir electrode. The peak at 533.15 eV in FGA can thus be assigned to unbound O in the Ir top electrode.

6.2. Measurements without top electrode

Since all three samples originate from a single piece and are annealed at the same temperature, the bottom interface can be assumed to have similar properties. Figure 6.2 c) shows a HAXPES overview spectra of all samples at areas without the top electrode. In contrast to the strong reaction of the top electrode on the respective annealing atmosphere, here it does not impact either the peak shape or the binding energies of the core levels of the bare HfO_2 layer. Only a single deviation at around 61 eV can be detected in FGA (10°). At ∼65 eV the peak of the Hf 5s core level is located, which overlaps with the IrO_2 signal of the bottom electrode. The inset depicts this core level at a higher emission angle, where the former deviation disappears. Changing the emission angle to higher values reduces the size of the photon beam and can lead to a slightly changed measuring position on the sample. The deviation has to be counted as an artifact in the measurement of FGA due to having a fraction of the beam still hitting the top electrode. Excluding this artefact, no differences across the different samples can be detected.
Figure 6.3 a) and b) depicts the Hf 4f spectra obtained from the samples a) with and b) without top electrode. All Hf 4f spectra have the same peak shape, not showing any hidden contribution. With top electrode the FGA spectrum ($E_{\mathrm{bin,Hf4f_{7/2}}}$=16.73 ±0.03 eV) shows a shift of 450 meV compared to the NA, OA spectra ($E_{\mathrm{bin,Hf4f_{7/2}}}$=16.28 ±0.03 eV). Without top electrode all core-levels have the same binding energies ($E_{\mathrm{bin,Hf4f_{7/2}}}$=16.41 ±0.03 eV). To interpret these shifts, it is essential to keep in mind that the measurements through the top electrode mainly study the interface between the HZO layer and the top electrode. In contrast, in the measurement without the top electrode, the complete HZO layer is examined.

The observed shifts can be explained by band offsets that form due to different work functions of the electrode materials and different defect concentrations at the interfaces. Without top electrode the valence band VB of the HZO layer gives a clear signal, so that the valence band maximum VB_{max} can be determines (see Fig. 6.2). The energy difference between VB_{max} and the Hf $4f_{7/2}$ peak is 13.73 eV, which is a material-dependent

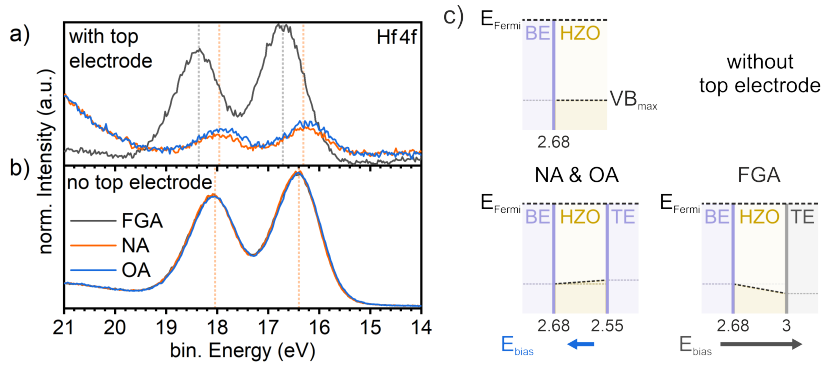

Figure 6.3.: Hf 4f spectra of all HZO-samples a) with and b) without top electrode. In a) a binding energy shift of 450 meV between the spectra of FGA and the other samples is apparent. The Hf 4f peaks in b) have the same binding energy. c) Model of the binding energy shift. The numbers represent the binding energy in eV of the valence band maximum at the interface to the bottom electrode (BE) and top electrode (TE). Own images, a) and b) are published in ref. [68].

factor. Thus the valence band maximum can be determines for the measurements with top electrode, despite the signal overlap from the top electrode, by $VB_{max} = E_{bin,Hf4f_{7/2}}$-13.73 eV (see *Kraut method* in section 3.2.3). Figure 6.3 c) illustrates the band offset schematically via the energy position of VB_{max}. From the measurements without the top electrode, the band alignment at the bottom electrode is deducible. With the top electrode, the value for VB_{max} is different at the bottom and the top interface. For NA and OA, at the bottom electrode VB_{max} has a slightly higher value than the top electrode, demonstrating a bias field in the direction of the bottom electrode. This indicates differences at the top and bottom interfaces that can be explained by the deposition process. For once, at the interfaces, lattice mismatches can occur, leading to strain. Due to the order of deposition, possible lattice mismatches at the bottom electrode are more likely to affect the HZO layer, and at the top electrode, more likely to affect the IrO_2 layer. In addition, the ALD process increases in quality with increasing deposition cycles. Thus the HZO layer has a higher probability that oxygen vacancies emerge at the interface to the bottom electrode than to the top electrode.
The reduction of the top electrode from IrO_2 to Ir in FGA acts twofold. Ir has a higher density and smaller volume of the unit cell than IrO_2, such that the reduction introduces additional strain at the top electrode. This can already be observed in the image from FGA (see Fig. 6.1), showing one corner of the larger rectangular top electrode splintered. Ir has a higher work function than IrO_2 (ϕ_{Ir}=5.42-5.78 eV [106];ϕ_{IrO_2}=4.2-4.6[107]), which creates the bias field in the direction of the top electrode and thus leads to higher $E_{bin,Hf\,4f_{7/2}}$ and VB_{max} at the top interface.

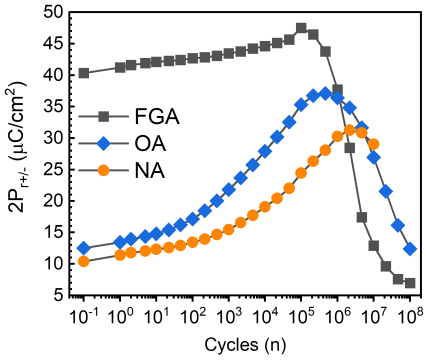

Figure 6.4: Electric field cycling behaviour of NA, OA, and FGA, showing the double remanent polarization $2P_r$. Data is presented in ref. [68, 69].

Summarizing the HAXPES results, it could be shown that the use of O_2 instead of N_2 as annealing gas oxidizes any remaining metallic Ir content of the top electrode or avoids any formation of metallic Ir. Using FG as annealing gas completely reduces the top electrode from IrO_2 to Ir, creating a capacitor structure with asymmetric electrodes, which forms a bias field across the HZO layer. In addition, unbound oxygen could be detected in the Ir layer. To see how those chemical changes affect the ferroeletric properties, the double remanent polarization $2P_r$ is plotted in Figure 6.4. NA and OA show almost similar pristine polarization values, but differently strong wake-up phases. The OA sample was annealed for 1 min, instead of 20 s like in the NA and FGA cases. This additional parameter is a possible source for the difference in NA and OA.
The pristine $2P_r$ value for the FGA sample is significantly larger than in OA and NA, showing improved ferroelectric properties. In addition nearly no wake-up behavior and a strong decline in $2P_r$ occurs past 10^5 cycles. To understand this behavior and how electrical field cycling may change the chemical properties, HAXPES experiments have been conducted on the dot structure of FGA, which were cycled in advance.

6.3. Electrical field induced changes

The following results are part of the published paper *Hard x-ray photoelectron spectroscopy of tunable oxide interfaces* M. Müller, P. Lömker, P. Rosenberger, M. Hussein Hamed, D.N. Mueller, R.A. Heinen, T. Szyjka, and L. Baumgarten, Journal of Vacuum Science & Technology A 40, 013215 (2022) [67]. The specific section in this paper is **V.***C. Oxygen supply by IrO_2 electrodes contains.* All HAXPES measurements and data analysis for this part and all data representations and descriptions there are done by me.

The top electrode of each sample is structured in a dot array, where each dot represents the top electrode of a separate capacitor. In order to study electrical field induced changes, an FG annealed IrO_2/HZO/IrO_2 sample is used, where prior to the HAXPES experiment, different dots are electrical field cycled with different repetition rates. The challenge in this experiment is the positioning of the photon beam onto the dots, which

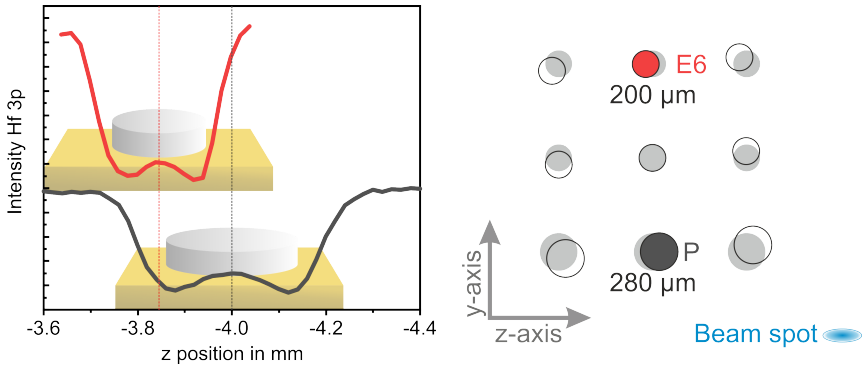

Figure 6.5.: Plot of the z-axis scan. The scan is obtained by measuring the signal intensity at the binding energy of Hf 3p at different positions. Dots block this signal enabling the determination of their position. The sample was slightly rotated in comparison to the internal coordinate system of the HAXPES setup. Due to this tilt, the dots are not aligned and have different z positions.

have a diameter that is just 2-3 times larger than the ideal spot size of the beam. The HAXPES experiment were conducted at 10° photo emission angle, which also describes the angle between the surface of the sample and the photon beam (see Fig. 2.21). At this angle, the beam spot is elongated in one direction (z-axis) at the factor $1/\sin(10°)\approx 5.8$, so that the spot size roughly matches the diameter of the dots. The position of the dots were determined by measuring the photo electron beam intensity at the binding energy of the Hf 3p core level at multiple positions. Adding up the measurement at the different positions result in a z-scan. Figure 6.5 shows a scan along the z-axis. When part of the photon beam hits a dot the signal from the HZO layer gets attenuated. The minima relate to the edges of the dots. The HAXPES measurements were performed at the center of the dots. In total, two dots with one (*Pristine* **FGA-P**) and 10^6 cycles (**FGA-E6**) are studied. The diameter of the FGA-P dot is 280 µm and of the FGA-E6 dot is 200 µm. Section 6.1 shows that the Ir top electrode in FGA contains oxygen unbound to Ir. Such oxygen can be mobile and redistributed when an electrical field is applied. Figure 6.6 a) shows HAXPES spectra of FGA-P and FGA-E6 ranging from the Ir $4p_{3/2}$ to the O 1s core level. The spectra are normalized to the measurement time per data point (dwell time). The contribution of the unbound oxygen is relatively small in comparison to the overall signal intensity and has to be separated first before comparing FGA-P to FGA-E6. Two components have to be taken into account, the background of the Ir $4p_{32}$ core level and the HZO contributions at the O 1s core level. The background of the Ir $4p_{32}$ was constructed by a Shirley background around the peak, a linear decline afterward, and a Gaussian fit of the shake-up feature, which is added to it all. The inset in Figure 6.6 a) shows the O 1s spectra without this background. The O 1s core level of the HZO layer shows a shift and different intensities. The intensity difference can be explained by the smaller size of the FGA-E6 dot, where a small contribution

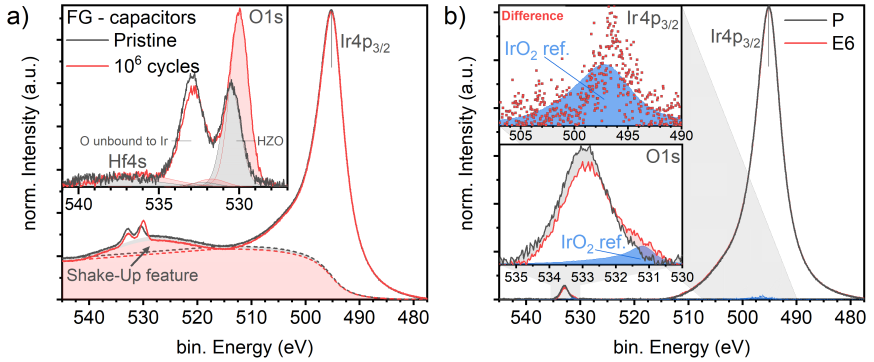

Figure 6.6.: a) HAXPES spectra of the Ir $4p_{3/2}$ and O 1s core levels. The shaded area marks the background created by the Ir $4p_{3/2}$ core level. The inset shows the O 1s core level without the background of Ir $4p_{3/2}$. b) Background corrected spectra of the Ir $4p_{3/2}$ and O 1s core levels with subtracted HZO contributions. Own images, a modified version of b) is published in ref. [68].

of the elongated beam spot might miss the dot and add some signal of the HZO layer without attenuation. Using measurements next to the dots as a reference, the exact fitting parameters of all HZO relating components are known. Accounting for the correct intensities and binding energies, the fit parameters were used to subtract the HZO contribution.
Figure 6.6 b) depicts the background-corrected spectra of the Ir $4p_{3/2}$ and O 1s core level. Comparing the shape by subtracting the FGA-P spectrum from the FGA-E6 spectrum reveals additional contributions at O 1s and Ir $4p_{3/2}$ and an intensity decrease in the O 1s peak. The binding energies and shape of those contributions fit IrO_2. The spectrum of OA is taken as a reference for IrO_2 and plotted with a downscaled intensity, matching the additional contributions. A closer look at the O 1s peak shows that the intensity reduction in FGA-E6 at 533 eV matches the intensity increase at 531 eV. Concluding those observations, the intensive electric field cycling in FGA-E6 leads to the formation of IrO_2 at the expense of the unbound oxygen.

In the following the cycling-induced effects on the HZO layer are discussed. Figure 6.7 a) depicts the Hf 4f core level, with the background of the Ir top electrode subtracted and normalized to the Hf $4f_{5/2}$ peak maximum. A peak shape comparison between FGA and FGA-P in combination with a fitting process revealed an additional Hf^{3+} contribution for FGA-P, which persists even when the increased noise in the FGA-P measurement is accounted for. This can be interpreted as an indication of the existence of neutral vacancies at the top electrode in the uncycled case and a redistribution of the charges after applying an electrical field, thus creating Hf with a valency of 3+. The binding energies of FGA and FGA-P are identical, but FGA-E6 shows an energy shift so that the binding energy match that of OA. With an increasing number of cycles, the Hf^{3+}

vanishes, indicating a reduction of the V_O concentration at the interface, and, as shown, IrO_2 forms. It is plausible that the IrO_2 forms at the interface, dissolving the asymmetry in the electrodes and reducing the internal bias field. Figure 6.7 c) schematically illustrates the chemical changes between FGA-P and FGA-E6 and the band offset via the energy position of VB_{max}. After 10^6 cycles, the energy shifts and internal bias field of the FGA sample are similar to the ones found in the NA and OA samples (see Fig. 6.3).

The electrical field cycling experiment of FGA showed a high pristine $2P_r$ value, nearly no wake-up, and a strong decline past 10^5 cycles (see Fig. 6.4). The behavior can be reconciled with the HAXPES results. For this purpose, all findings are recapitulated:
During the annealing process of the FGA sample, the IrO_2 top electrode is reduced to Ir containing unbound O, possibly also affecting the HZO layer at the top interface and creating neutral V_O. The reduction introduces additional strain at the top interface due to the different lattice constants of IrO_2 and Ir, as well as a bias field pointing from the bottom to the top electrode. Strain and vacancies are known stabilizing factors for the ferroelectric o-phase, which, combined with the bias field, could explain the high pristine $2P_r$ value and the lack of a wake-up phase.
Extensive electric field cycling leads to a reduction of the V_O concentration and the formation of IrO_2 at the top interface, which dissolves the bias field and the strain at the top interface. Thus the ferroelectric phase is destabilized, explaining the relatively rapid decline of the $2P_r$ value with further increasing electrical field cycling.

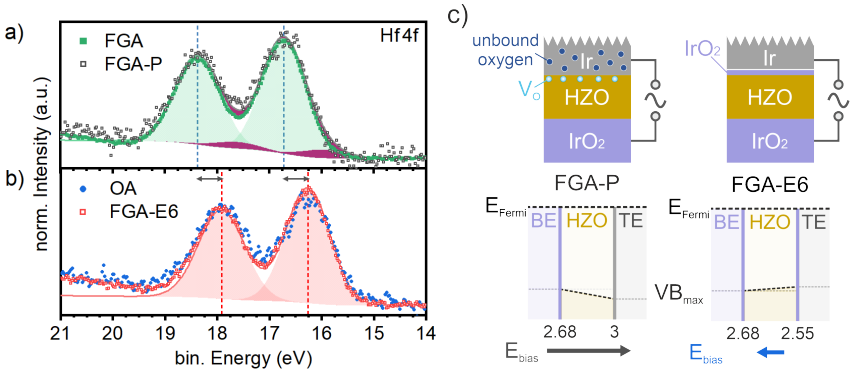

Figure 6.7.: Hf 4f spectra of FGA, FGA-P, FGA-E6, and OA. The background created by the Ir top electrode is subtracted and the spectra are normalized to the Hf $4f_{5/2}$. a) A comparison between FGA and FGA-P reveals Hf^{3+} contributions in the pristine cycled dot. b) The spectrum of FGA-E6 completely matches the one of OA. c) Model of the chemical changes and binding energy shift in FGA-P and FGA-E6. The numbers represent the binding energy in eV of the valence band maximum at the interface to the bottom electrode (BE) and top electrode (TE). Own images, slightly modified versions of a) and b) are published in ref. [67].

CHAPTER 7

Conclusion and Outlook

This thesis aims at developing a holistic picture of the root causes and properties of ferroelectricity in HfO_2-based capacitor structures. HAXPES studies were conducted on metal-isolator-metal structures, which had undergone complementing structural and transport pre-characterizations, determining their ferroelectric properties. Thus a direct correlation between the ferroelectric properties and chemical characterization via HAXPES could be achieved.

Several stabilizing factors for the ferroelectric phase could be identified, ranging from oxygen vacancies to strain induced by the electrodes. In addition, the influence of electrical field switching on the ferroelectric properties could be determined and linked to chemical changes. In total, the results of three sample sets were presented, where the HAXPES results could be separated into the main ferroelectric layer, the interfaces to the electrodes, and the electrodes themselves. The results shall be summarized, starting with the detection of oxygen vacancies.

Detecting vacancies

Since a vacancy is the absence of an atom in a lattice, it can not be directly observed and has to be studied by its indirect effect on the surrounding electronic properties. Figure 7.1 a) & b) summarizes how oxygen vacancies can be detected in a HfO_2 layer via HAXPES. In the case of charged V_O, Hf ions with a valency of 3+ instead of the typically observed 4+ and a chemical shift of the Hf 4f core levels to higher binding energies could be detected. For HfO_2 films produced via ALD, no substantial binding energy shift to higher E_{bin}, and no significant Hf^{3+} contribution could be detected. However, an additional O 1s feature at higher binding energies is detected. Studies showed that such an "O^{1-}" feature can be an accompanying phenomenon of oxygen vacancies in transition metal oxides [91–93]. The lattice positions of the ions surrounding an V_O probable

include Hf-O bonds with higher covalence, thus "O^{1-}" ions. The exact implementation in the lattice is still an open question.
The contradictory observations between missing V_O characteristics (E_{bin} shifts, Hf^{3+}) on the one hand and additional V_O characteristic ("O^{1-}") on the other hand was attributed to a more subtle feature, namely a VN_2-complex. Here, no Hf^{3+} is present, and the valence states created by the charged vacancies are compensated. An additional hint for the formation of VN_2 is a Hf-N^{3-} signal at the N 1s core level. Due to the quantification of the relative V_O concentration, V_O as a stabilizing factor of the ferroelectric orthorhombic phase in HfO_2 could be confirmed. The different configurations of oxygen vacancies (V_O^{2+}, V_O^{1+}, VN_2) coincide with different behaviors of the capacitor structure during electrical field cycling. Samples with the VN_2-complex seem to have a wake-up phase that takes more cycles than in the case of charged vacancies. This could indicate different V_O mobility during cycling, depending on the configuration of the V_O.

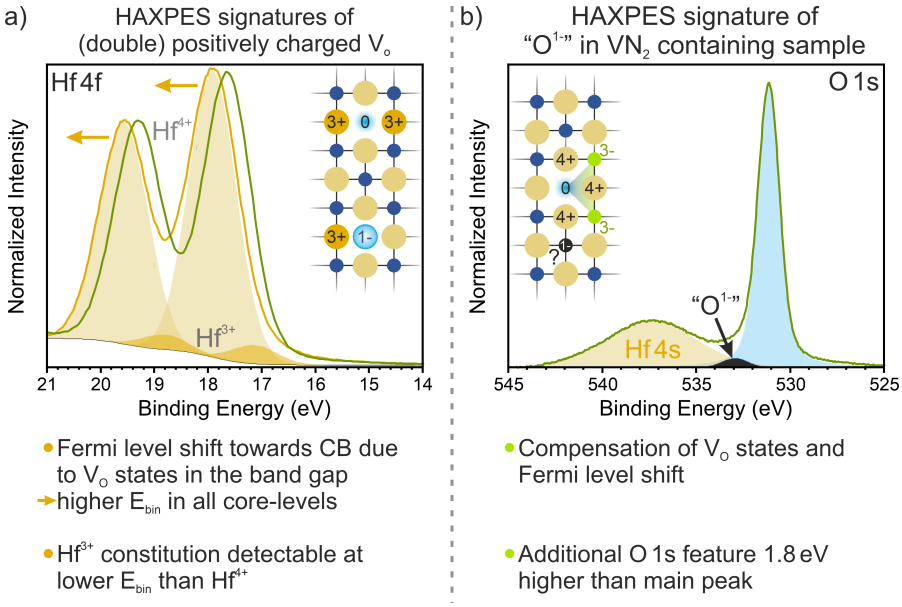

Figure 7.1.: Detecting vacancies via HAXPES spectra: a) Charged oxygen vacancies. b) Possible VN_2 induced "O^{-1}" feature.

The role of the electrodes

TiN and IrO_2 as electrode materials have been studied. Having the HfO_2 layer in direct contact with the TiN bottom electrode leads to an exchange of N and O during the annealing process and the creation of additional V_O at the interface (see Fig. 7.2 a)). This exchange could be reduced by the introduction of an intermediate TiO_2 layer (see Fig. 7.2 b)). This can be achieved by exposing the bottom electrode in the vacuum chamber to an O_2 gas flow or by exposing the electrode to a normal atmosphere. The oxidation process of the TiN layer is limited to $\sim 3.5(\pm 0.5)$ nm. An improvement of the remanent polarisation value could be seen anlong with an increase of the layer thickness of TiO_2 up to 1 nm, where no longer any N and O exchange could be detected.
IrO_2 as electrode material exposed to N_2 or O_2 as annealing gas seems to act passively or potentially fills up vacancies at the interfaces during the annealing process (see Fig. 7.2 c)). Annealing with FG reduces the top electrode from IrO_2 to Ir with traces of unbound O, and introduces an additional lattice strain, due to the different lattice parameters in Ir and IrO_2. The reduction might also be observed at the ferroelectric layer and leads to an introduction of additional vacancies at the interface (see Fig. 7.2 d)). For FGA, a bias field pointing from the bottom to the top electrode could be determined, which relates to the different work functions at the interfaces to the bottom (IrO_2) and top electrode (Ir). Compared to NA and OA, FGA samples shows around four times higher pristine $2P_r$ value, nearly no wake-up phase, and a strong decrease of $2P_r$ after 10^5 cycles. The difference in the pristine $2P_r$ values can be directly attributed to the changes at the top electrode.
Additional HAXPES experiments on capacitors of FGA samples were conducted to study the effects of increasing electrical field cycling on the chemical properties. For capacitors switched by 10^6 cycles, a formation of IrO_2 at the interface to the top electrode could be detected, and the Hf^{3+} signal vanishes (see Fig. 7.2 e)). Thus the strain at the interface is reduced, and the work function at the top and bottom interface equalizes. These findings can explain the rapid decline in the $2P_r$ value found in FGA.

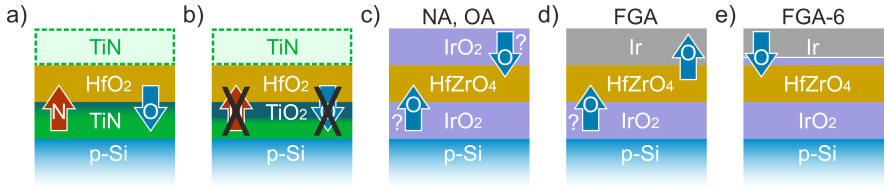

Figure 7.2.: Different interface oxygen exchange mechanisms occur in $Hf(Zr)O_2$ -based MIM structures, dependent on the choice of the metal electrodes: a) oxygen scavenging by a TiN electrode, b) interface passivation by a TiO_2 interlayer, c) oxygen source during annealing in O_2 (N_2), d) oxygen source at the bottom electrode and oxygen scavenging during annealing in forming gas, and e) oxygen source (unbound O in Ir) during electrical field cycling. Own images, a simplified version of this image is published in ref. [68].

Outlook

In conclusion, the results of the conducted HAXPES studies could directly be linked to the ferroelectric properties and electrical field cycling behavior, enabling a more specific design of the capacitor structures in the future and enabling an optimized performance. Moreover, we extracted indirect and direct HAXPES spectral signatures related to V_O. This approach may also be applied to identify V_O not only in HfO_2 but also in other oxides. However, for example more studies on the relation of the "O^{1-}" and the VN_2-complex are needed.
As a proposition for a future experiment, which investigates this relationship and also the different V_O mobility in charged vacancies and VN_2, a capacitor stack similar to the completely PVD-grown TiN/HfO_2/TiN layer stack could be realized but with a targeted treatment of the bottom electrode. In this case, the bottom electrode would be exposed to a high dose of an O_2 flow, creating a saturated TiO_2 layer and inhibiting any nitrogen exchange a the bottom interface during RTA. During the deposition of the HfO_2 layer, instead of O_2, a N_2 gas flow would be used (see Fig. 7.3 c)). Under the naive assumption that the overall V_O concentration stays the same with added N_2 instead of O_2, it might be possible to induce a direct transition of charged vacancies into the VN_2 complex while using higher N_2 flow rates. The TiO_2 interlayer at the bottom electrode ensures that no Hf-N exchange interferes with the desired introduction of N into the HfO_2 layer.

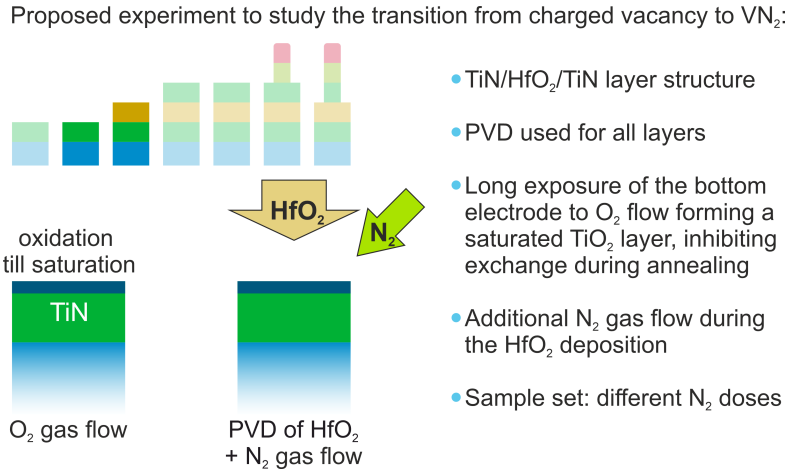

Figure 7.3.: Proposed future experiment to study the formation of the VN_2-complex and the effects on the (ferro-)electrical properties.

APPENDIX A

Appendix

A.1. SESSA

In this thesis, SESSA is mainly used to compute the IMFP and TRMFP of the studied sample structures. SESSA needs as information the **Source** (photon energy E_{Ph}), the energy range of the **Spectrometer**, as well as the composition and density of the **Sample**. The results of the computed IMFP and TRMFP can be found at **Parameters**. Figure A.1 shows the starting menu of SESSA. The first step is to change the source to *Photons* with the desired photon energy E_{Ph} (e.g. 6000 eV) (see Fig. A.2). In parallel with this change, the energy range of the spectrometer has to be changed (see. Fig. A.2). Important note: SESSA can have some problems if one tries to change the range of the predefined "Region #1" directly. It is better just to create ("Add...") a new region, where the higher bound equals the chosen photon energy and the lower bound some lower value including the core-level of interest.

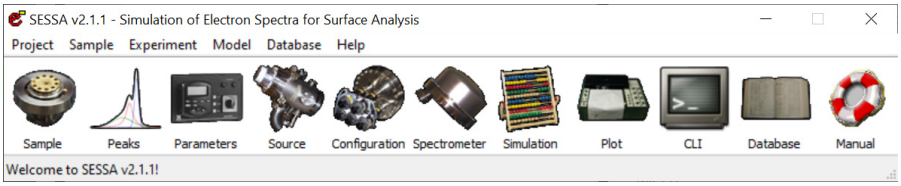

Figure A.1.: Overview of the menu. The order the different windows have to be open are: 1. Source; 2. Spectrometer; 3. Sample; 4. Parameter.

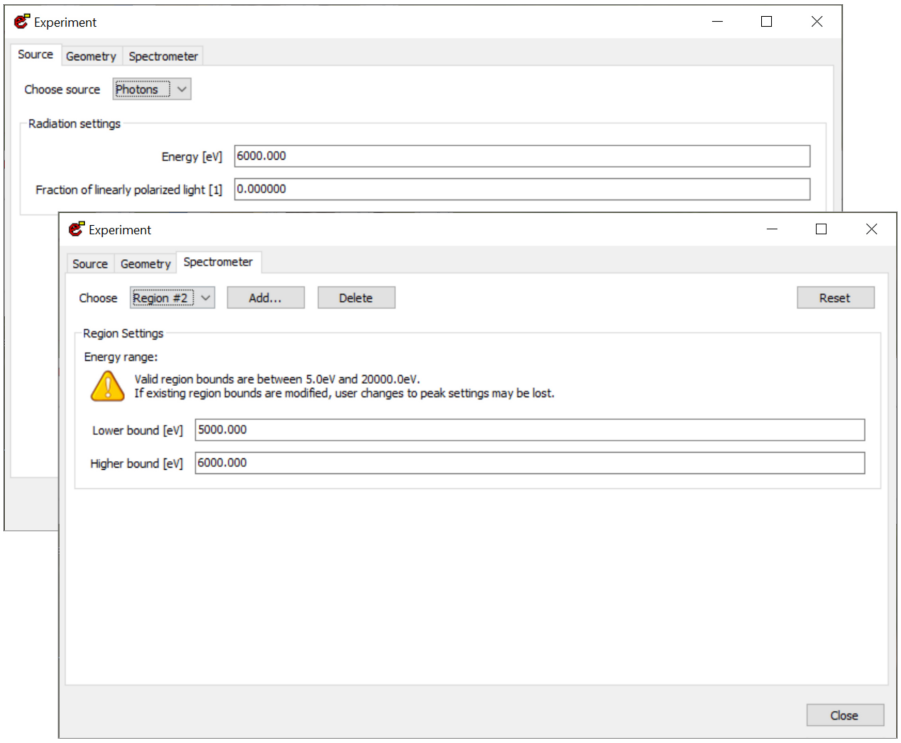

Figure A.2.: Source and Spectrometer

The first step of defining the sample properties is to change the "Morphology" from Spheres (default) to Planar. Under "Layer Specification", the Material can be defined (e.g. /HF/O2/ for HfO_2). SESSA checks its internal database for the material and fills in a default density. If one wants to fill in a specific density, it is important to consider the units. Typically the density is measured in g/cm^3. This can be converted from g/cm^3 to atoms/cm^3 by:

$$\rho[\text{atoms/cm}^3] \equiv \rho[\text{g/cm}^3]/F \cdot \text{N}_\text{A} \cdot n \tag{A.1}$$

Here F represents the formula weight, N_A the Avogadro constant, and n the number of elements in the compound (e.g., n_{TiO_2}=3; n_{TiN}=2;).

Example calculation for TiN:

- $\rho_{\text{default}}[\#/\text{cm}^3] = 1.016{\cdot}10^{23}$ atoms/cm^3
- $\rho_{\text{exp}} = 5.36$ g/cm^3
- Atomic mass: Ti = 47.88 u; N = 14.007 u
- $F = 47.88\,\text{u} + 14.007\,\text{u} = 61.887\,\text{u}$
- $\text{N}_\text{A} = 6.022{\cdot}10^{23}$/mol
- $n_{\text{TiN}} = 2$
- $\rightarrow \rho_{\text{exp}} = 1.043{\cdot}10^{23}$ atoms/cm^3

The thickness is irrelevant for IMFP and TRMFP.

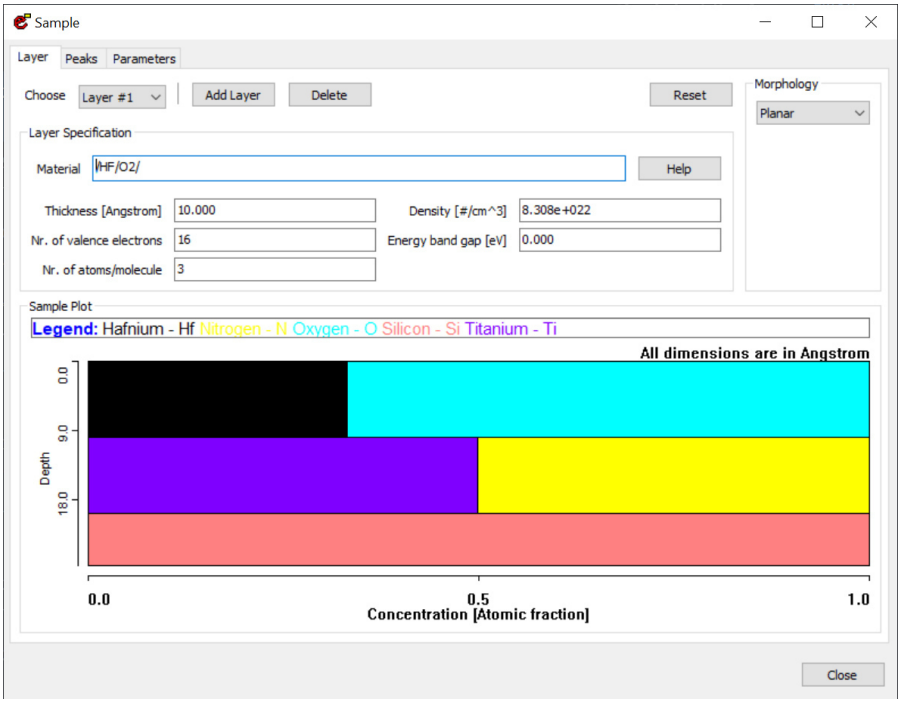

Figure A.3.: Sample

After entering the necessary input the IMFP and TRMFP values can be found in **Parameters** (see Fig. A.4). There the core level can be chosen ("Choose Peak"). Important note for calculating L (see equ. (3.12)): The values are given in Å.

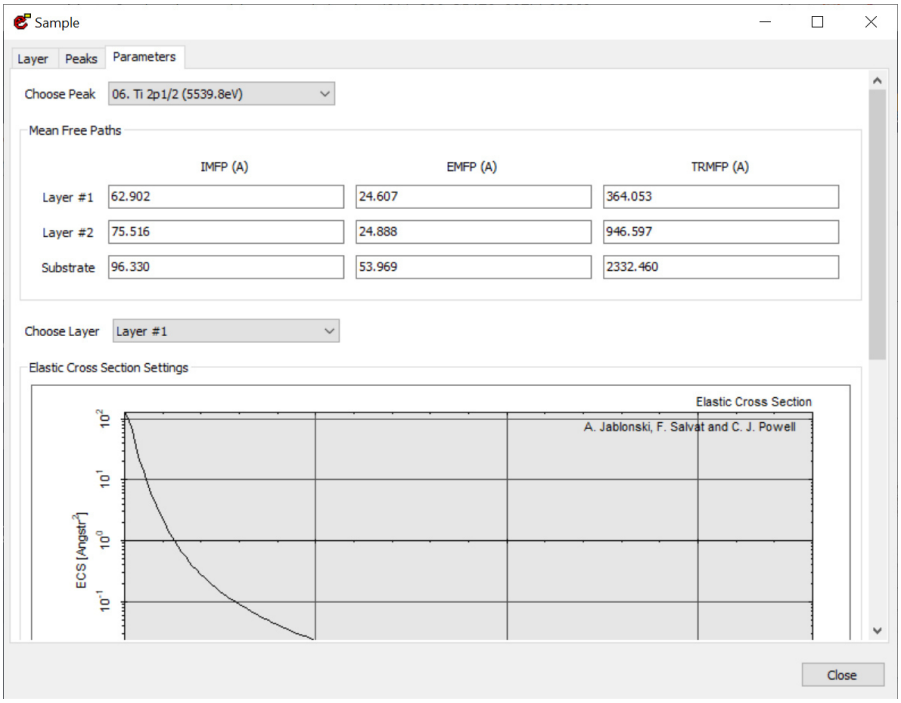

Figure A.4.: Parameters

A.2. Photoionization cross sections

Figure A.5 and A.6 show the photoionization cross sections of selected elements and core-levels. The photoionization cross section is discussed in section 2.2.4.

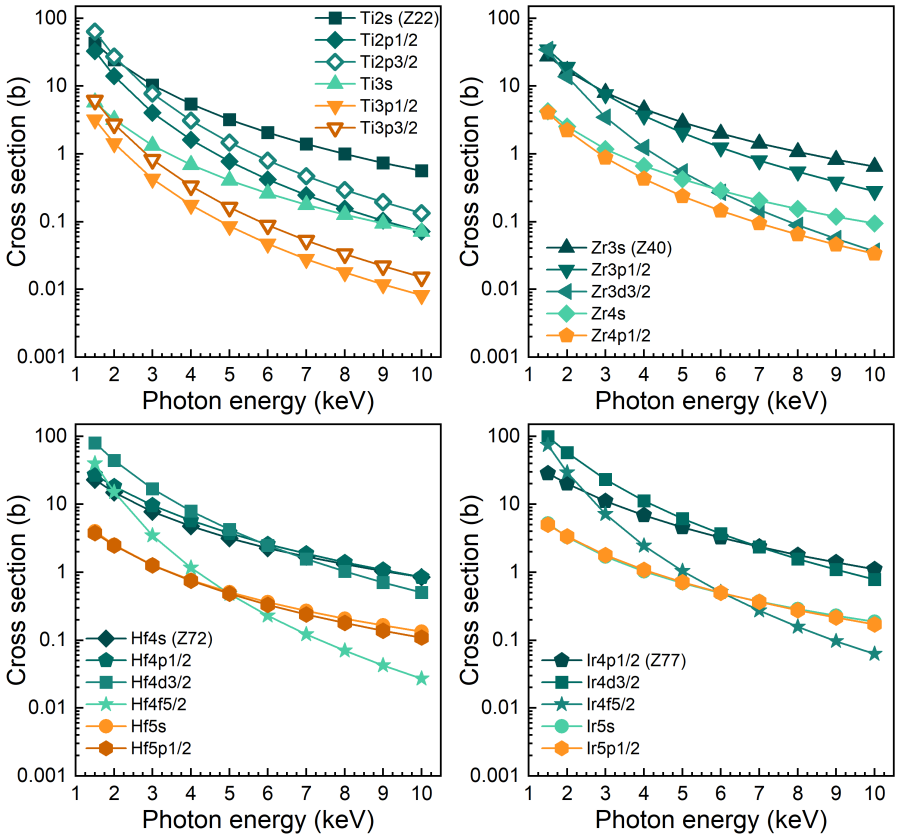

Figure A.5.: Photoionization cross sections of selected elements and core-levels. The data for these plots stem from [56].

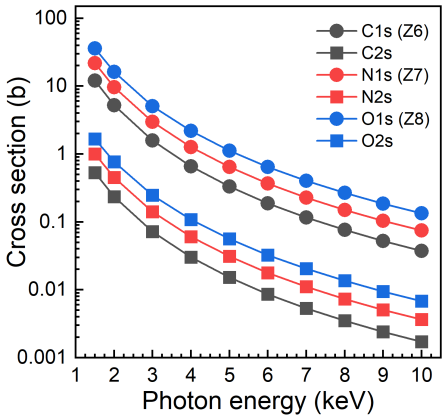

Figure A.6.: Photoionization cross sections of selected elements and core-levels. The data for these plots stem from [56].

A.3. Estimation of surface carbon signal contribution in XPS and HAXPES

The following estimation is used in section 2.2.4.

Sample surfaces can be contaminated by carbon. A model system of 0.2 nm thick C layer at the surface of a HfO_2 layer with 1% C content is used to estimate how much the surface C obscures XPS and HAXPES measurements of possible carbon in a HfO_2 sample (see Figure A.7).

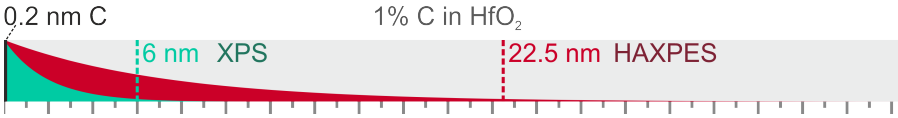

Figure A.7.: Model system: HfO_2 with 1% C and a 0.2 nm thick C layer at the surface. The dotted lines show the information depth of XPS (1486.6 eV) and HAXPES (6 keV).

The intensity in the direction of the surface's normal is considered and can be determined by integrating over equ. (2.21). The general solution of the integration is:

$$I = I^{\infty} \int_a^b dx[\mathrm{e}^{-x/L}] = I^{\infty} L(\mathrm{e}^{-a/L} - \mathrm{e}^{-b/L}) \,. \tag{A.2}$$

For the 0.2 nm thick C surface ($a = 0$ nm, $b = 0.2$ nm) the signal intensity is thus:

$$I_{\mathrm{surface}} = I_{\mathrm{C}}^{\infty} \cdot L_{\mathrm{C}}(1 - \mathrm{e}^{-0.2\,\mathrm{nm}/L_{\mathrm{C}}}) \,. \tag{A.3}$$

The bulk signal is damped by the surface and can be calculated by:

$$I_{\mathrm{bulk}} = I_{\mathrm{HfO_2:C}}^{\infty} \cdot L_{\mathrm{HfO_2:C}} \cdot \mathrm{e}^{-0.2\,\mathrm{nm}/L_{\mathrm{C}}} \,. \tag{A.4}$$

$L_{\mathrm{C,C}}$ and $L_{\mathrm{HfO_2:C}}$ are the effective attenuation length of the C signal in surface and bulk, respectively. Table A.1 list the IMFP, TRMFP and the effective attenuation length of C 1s photo electrons excited by photons with 1486.6 eV (XPS) and 6 keV (HAXPES) photon energy. The values were calculated by SESSA using the default density of C ($\rho_{\mathrm{C}}[\#/\mathrm{cm}^3] = 1.103{\cdot}10^{23}$ atoms/cm^3) and $HfO_2C_{0.03}$ ($\rho_{\mathrm{HfO_2C_{0.03}}}[\#/\mathrm{cm}^3] = 5.151{\cdot}10^{22}$ atoms/cm^3). Those densities in combination with L can be used to determine R^{∞}, the ratio of infinite thick layers (see sec. 3.2.4):

$$R^{\infty} = \frac{\rho_{\mathrm{C}}[\#/\mathrm{cm}^3]/N_{\mathrm{C}} \cdot n_{\mathrm{C,C}} \cdot L_{\mathrm{C}}}{\rho_{\mathrm{HfO_2C_{0.03}}}[\#/\mathrm{cm}^3]/N_{\mathrm{HfO_2C_{0.03}}} \cdot n_{\mathrm{C,HfO_2C_{0.03}}} \cdot L_{\mathrm{HfO_2:C}}} \,. \tag{A.5}$$

Here N is the number of atoms in the chemical formula, and $n_{a,b}$ is the number of element a in compound b. In the model system the values for N and n are as follows: $N_{\mathrm{C}} = n_{\mathrm{C,C}} = 1$; $N_{\mathrm{HfO_2C_{0.03}}} = 3.03$; $n_{\mathrm{C,HfO_2C_{0.03}}} = 0.03$.

Table A.1.: IMFP and TRMFP of the C 1s core level of a pure C layer and 1% C in a HfO_2 bulk material. The values were calculated by SESSA using the default density.

C 1s	XPS Al K_α			HAXPES 6 keV		
	λ_{in} (nm)	λ_{tr} (nm)	L(nm)	λ_{in} (nm)	λ_{tr} (nm)	L(nm)
C	3.08	31.89	2.88	11.03	504.05	10.85
HfO_2:C	2.31	8.85	1.96	8.11	61.92	7.42

Using equ. (A.5) the R^∞ values can be calculated for XPS and HAXPES as: $R^\infty_{XPS} = 31.78$; $R^\infty_{HAXPES} = 31.57$.
The ratio of equation (A.3), and (A.4) defines the relative C 1s signal contribution of the surface:

$$I_{\text{C 1s, surface}} = \frac{I_{\text{surface}}}{I_{\text{surface}} + I_{\text{bulk}}} = \frac{1 - \mathrm{e}^{-0.2/L_{\text{C}}}}{(1 - \mathrm{e}^{-0.2/L_{\text{C}}}) + 1/R^\infty \cdot L_{\text{HfO}_2\text{:C}}/L_{\text{C}} \cdot \mathrm{e}^{-0.2/L_{\text{C}}}} \quad \text{(A.6)}$$

This equation with all parameters for C and HfO_2:C result in $I_{\text{C 1s, surface}}$=77% for XPS, and 46.2% for HAXPES. Figure 2.18 in section 2.2.4 depicts $I_{\text{C 1s, surface}}$ by plotting a C 1s core level spectrum. For the plots two peaks (*Gaussian*) at $x_{\text{c}} = 285.4\,\text{eV}$ and $x_{\text{c}} = 287\,\text{eV}$ with a FWHM of $w = 1.6\,\text{eV}$ are used. The ratio between the peak area is $A_{287\,\text{eV}}/A_{285.4\,\text{eV}} = 0.182$. The peak positions, FWHM and the ratio stem from a measured C 1s spectrum.

A.4. Derivation of the thickness determination

In section 3.2.4 the relation of the photoelectron intensity of a two-layer model is formulated in equ. (3.11):

$$R = R^{\infty} \frac{[1 - \mathrm{e}^{-d_A/(L_{A,A}\cos\theta)}]}{[1 - \mathrm{e}^{-d_B/(L_{B,B}\cos\theta)}] \cdot \mathrm{e}^{-d_A/(L_{B,A}\cos\theta)}} \,. \tag{A.7}$$

To make this equation applicable for thickness determination, the special case of comparing the intensity of the same element and core-level is used (e.g., Ti 2p when comparing TiN with TiO_2). Here the EAL of photoelectrons in the upper layer can be assumed to be similar: $L_{A,A} = L_{B,A} = L_A$. For simplification the notation of $L_{B,B}$ can be reduced to L_B. In the following the equation is solved for d_A:

$$\begin{aligned}
R =& R^{\infty} \frac{[1 - \mathrm{e}^{-d_A/(L_A\cos\theta)}]}{[1 - \mathrm{e}^{-d_B/(L_B\cos\theta)}] \cdot \mathrm{e}^{-d_A/(L_A\cos\theta)}} \\
\Leftrightarrow \quad R \cdot [1 - \mathrm{e}^{-d_B/(L_B\cos\theta)}] =& R^{\infty} \cdot [\mathrm{e}^{d_A/(L_A\cos\theta)} - 1] \\
\Leftrightarrow \quad R - R \cdot \mathrm{e}^{-d_B/(L_B\cos\theta)} =& R^{\infty} \cdot \mathrm{e}^{d_A/(L_A\cos\theta)} - R^{\infty} \\
\Leftrightarrow \quad R + R^{\infty} =& R \cdot \mathrm{e}^{-d_B/(L_B\cos\theta)} + R^{\infty} \cdot \mathrm{e}^{d_A/(L_A\cos\theta)} \\
\Leftrightarrow \quad R + R^{\infty} =& \frac{[R \cdot \mathrm{e}^{-d_B/(L_B\cos\theta)} + R^{\infty} \cdot \mathrm{e}^{d_A/(L_A\cos\theta)}] \cdot \mathrm{e}^{-d_A/(L_A\cos\theta)}}{\mathrm{e}^{-d_A/(L_A\cos\theta)}} \\
\Leftrightarrow \quad R + R^{\infty} =& \mathrm{e}^{d_A/(L_A\cos\theta)} \cdot [R \cdot \mathrm{e}^{-d_B/(L_B\cos\theta) - d_A/(L_A\cos\theta} + R^{\infty}] \\
\Leftrightarrow \quad \mathrm{e}^{d_A/(L_A\cos\theta)} =& \frac{R + R^{\infty}}{R \cdot \mathrm{e}^{(-d_B/L_B - d_A/L_A)/\cos\theta} + R^{\infty}} \\
\Leftrightarrow \quad \frac{d_A}{L_A\cos\theta} =& \ln \frac{R + R^{\infty}}{R \cdot \mathrm{e}^{(-d_B/L_B - d_A/L_A)/\cos\theta} + R^{\infty}} \\
\Leftrightarrow \quad d_A =& L_A\cos\theta \cdot \ln \frac{R + R^{\infty}}{R \cdot \mathrm{e}^{(-d_B/L_B - d_A/L_A)/\cos\theta} + R^{\infty}} \,.
\end{aligned}$$

This can be simplified expressed by:

$$\begin{aligned}
d_A =& L_A\cos\theta \cdot \ln \frac{R + R^{\infty}}{R \cdot \mathrm{e}^{-x/\cos\theta} + R^{\infty}} \\
with \quad x =& (d_A/L_A + d_B/L_B).
\end{aligned} \tag{A.8}$$

A.4.1. Error calculation of the thickness determination

In this section, the error of the equ. (3.18) will be presented. Following equ. (3.18) will be repeated:

$$\begin{aligned} d_{\mathrm{TiO_2}} =& L_{\mathrm{TiO_2}} \cos\theta \cdot \ln \frac{R^\infty + R}{R \cdot \mathrm{e}^{-x/\cos\theta} + R^\infty} \\ \text{with} \quad & x = d_{\mathrm{TiO_2}}/L_{\mathrm{TiO_2}} + (d_{\mathrm{in}} - d_{\mathrm{TiO_2}} \cdot N_{\mathrm{Ti,\ TiO_2}}/N_{\mathrm{Ti,TiN}})/L_{\mathrm{TiN}} \,. \end{aligned}$$

The value R equals $I_{\mathrm{TiO_2}}/I_{\mathrm{TiN}}$. The error is calculated by the *Propagation of error*. For a function $f(a,b)$ the error is thus:

$$\Delta f = \| \frac{\partial f(a,b)}{\partial a} \Delta a \| + \| \frac{\partial f(a,b)}{\partial b} \Delta b \| \,. \tag{A.9}$$

Δa and Δb are the respective errors of the parameters. Using the propagation of error on equ. (3.18) results in:

$$\begin{aligned} \Delta d_{\mathrm{TiO_2}} = & \| \frac{\partial d_{\mathrm{TiO_2}}}{\partial I_{\mathrm{TiO_2}}} \Delta I_{\mathrm{TiO_2}} \| + \| \frac{\partial d_{\mathrm{TiO_2}}}{\partial I_{\mathrm{TiN}}} \Delta I_{\mathrm{TiN}} \| + \| \frac{\partial d_{\mathrm{TiO_2}}}{\partial \theta} \Delta \theta \| + \| \frac{\partial d_{\mathrm{TiO_2}}}{\partial d_{\mathrm{in}}} \Delta d_{\mathrm{in}} \| \\ & + \| \frac{\partial d_{\mathrm{TiO_2}}}{\partial R^\infty} \Delta R^\infty \| + \| \frac{\partial d_{\mathrm{TiO_2}}}{\partial L_{\mathrm{TiO_2}}} \Delta L_{\mathrm{TiO_2}} \| + \| \frac{\partial d_{\mathrm{TiO_2}}}{\partial L_{\mathrm{TiN}}} \Delta L_{\mathrm{TiN}} \| \end{aligned} \tag{A.10}$$

To solve this formula analytically, the derivation of each parameter has to be calculated. For practical use, the derivation can also be computed locally. In general, the derivation of a function $f(x)$ at the value x_0 can be described as:

$$\frac{\partial f(x_0)}{\partial x} = \lim_{\epsilon \to 0} \frac{f(x_0 + \epsilon) - f(x_0)}{\epsilon} \tag{A.11}$$

For a practical calculation of a derivative it is sufficient to use a small value for ϵ, e.g., ϵ=10^{-10}. Using this approach ($f = d_{\mathrm{TiO_2}}$, $x_0 = d_{\mathrm{TiO_2},n6}$), equ. (A.10) can be rewritten as:

$$\begin{aligned} \Delta d_{\mathrm{TiO_2}} =& \| \frac{\partial d_{\mathrm{TiO_2}}}{\partial I_{\mathrm{TiO_2}}} \Delta I_{\mathrm{TiO_2}} \| + ... \\ =& \| L_{\mathrm{TiO_2}} \cos\theta \cdot \ln \frac{R^\infty + (I_{\mathrm{TiO_2}} + \epsilon)/I_{\mathrm{TiN}}}{(I_{\mathrm{TiO_2}} + \epsilon)/I_{\mathrm{TiN}} \cdot \mathrm{e}^{-x/\cos\theta} + R^\infty} \Delta I_{\mathrm{TiO_2}} \| + ... \\ \text{with} \quad & x = d_{\mathrm{TiO_2},n6}/L_{\mathrm{TiO_2}} + (d_{\mathrm{in}} - d_{\mathrm{TiO_2},n6} \cdot N_{\mathrm{Ti,\ TiO_2}}/N_{\mathrm{Ti,TiN}})/L_{\mathrm{TiN}} \,. \end{aligned} \tag{A.12}$$

The error is calculated using the $d_{\mathrm{TiO_2}}$ value after 6 iterations ($d_{\mathrm{TiO_2},n6}$). This approach for the derivative has the advantage to be easily implemented in the calculating software (OriginPro, Excel, etc.), and to avoid mistakes in the analytical derivation. The values used for $d_{\mathrm{TiO_2}}$ and $\Delta d_{\mathrm{TiO_2}}$ depicted in Fig. 4.1 d) are listed in Table A.2.

Table A.2.: Values used in equ. (3.18) & (A.10) to calculate the effective thickness and its error of the TiO_2 layer. The results are plotted in Fig. 4.1.

	S0	S025	S05	S1	S2		
I_{TiO_2}	0.58	1.06	1.29	1.64	2.30	2.92	3.90
ΔI_{TiO_2}	0.08	0.06	0.04	0.04	0.04	0.05	0.10
I_{TiN}	4.02	3.27	3.27	3.27	4.02	4.02	4.02
ΔI_{TiN}	0.2	0.2	0.2	0.2	0.2	0.2	0.2
Angle θ	10°	10°	10°	10°	10°	41.41°	55°
$\Delta\theta$	0.1°	0.1°	0.1°	0.1°	0.1°	0.1°	0.1°
d_{in} (nm)	10	10	10	10	10	10	10
Δd_{in} (nm)	0.025	0.125	0.25	0.5	1	1	1

R^{∞}	ΔR^{∞}	L_{TiO_2}	L_{TiN}	ΔL
0.677	0.05	7.93	7.07	0.05

A.5. Appendix: Various types of oxygen vacancies

Figure A.8 shows the HAXPES spectra of the N 1s core level for both ALD-grown samples, recorded at 10° and 41.41° photoelectron emission angles. The spectra were normalized to the Hf $4p_{3/2}$ core level at 382.6 eV (not shown). For an improved presentation, the intensity scale of both plots in Fig. A.8 have been multiplied by a factor of 69.06. The N 1s spectra were fitted by Gaussian functions. We can distinguish between three different N contributions, which originate from C-N, from Ti-N related compounds as well as from Hf-N^{3-}. Normalized to the Hf 2p core level, the total N signal decreases with increasing photoelectron emission angle. This indicates that the origin of the signal lies deeper in the sample structure.

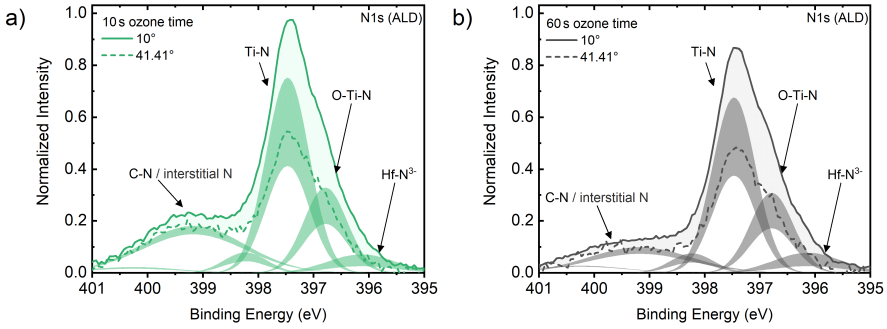

Figure A.8.: HAXPES spectra of N 1s core level for ALD-grown samples. The spectra are recorded at 10° and 41.41° photoelectron emission angles. a) ALD-grown sample with 10 s ozone time. b) ALD-grown sample with 60 s ozone time. Images from the SI of [66]

A.6. List of Abbreviations

BE/TE	bottom electrode / top electrode
a.u.	arbitrary units
ALD	Atomic Layer Deposition
BESSY	Berliner Elektronenspeicherring-Gesellschaft für Synchrotronstrahlung GmbH
CBM	conducting band minimum
CMOS	complementary metal-oxide-semiconductor
CN	coordination
DESY	Deutsches Elektronen-Synchrotron
DHM	Dynamic Hysteresis Measurement
EAL	Effective Attenuation Length
FeFET	ferroelectric field-effect transistor
FG	forming gas (90% N_2/10% H_2)
FWHM	Full Width at Half Maximum
GiXRD	Grazing incident X-ray diffraction
HDF5	Hierarchical Data Format 5
HZO	$Hf_{0.5}Zr_{0.5}O_2$
HAXPES	Hard X-ray Photoelectron Spectroscopy
IMFP	Inelastic Mean Free Path
MIM	metal-insulator-metal
NIST	National Institute of Standards and Technology
PVD	Physical Vapor Deposition
RTA	Rapid Thermal Annealing
sccm	standard cubic centimetres per minute
SESSA	Simulation of Electron Spectra for Surface Analysis
TEMA-Hf	$[(CH_3)(C_2H_5)N]_4Hf$
TEY	total electron yield
TRMFP	Transport Mean Free Path
VB	valence band
XRD	X-ray diffraction
XRR	X-ray reflectometry
XPS	X-ray Photoelectron Spectroscopy

Bibliography

[1] T. S. Böscke, J. Müller, D. Bräuhaus, U. Schröder, and U. Böttger, "Ferroelectricity in hafnium oxide thin films", Applied Physics Letters **99**, 102903, ISSN: 0003-6951 (2011) 10.1063/1.3634052 (cited on pages 1, 11).

[2] O. Ohtaka, H. Fukui, T. Kunisada, T. Fujisawa, K. Funakoshi, W. Utsumi, T. Irifune, K. Kuroda, and T. Kikegawa, "Phase relations and volume changes of hafnia under high pressure and high temperature", Journal of the American Ceramic Society **84**, 1369 (2001) https://doi.org/10.1111/j.1151-2916.2001.tb00843.x (cited on page 1).

[3] O. Ohtaka, H. Fukui, T. Kunisada, T. Fujisawa, K. Funakoshi, W. Utsumi, T. Irifune, K. Kuroda, and T. Kikegawa, "Phase relations and equations of state of ZrO_2 under high temperature and high pressure", Phys. Rev. B **63**, 174108 (2001) 10.1103/PhysRevB.63.174108 (cited on page 1).

[4] M. Hyuk Park, H. Joon Kim, Y. Jin Kim, W. Lee, H. Kyeom Kim, and C. Seong Hwang, "Effect of forming gas annealing on the ferroelectric properties of $Hf_{0.5}Zr_{0.5}O_2$ thin films with and without Pt electrodes", Applied Physics Letters **102**, 112914, ISSN: 0003-6951 (2013) 10.1063/1.4798265 (cited on pages 1, 82).

[5] T. S. Boscke, J. Muller, D. Brauhaus, U. Schroder, and U. Bottger, "Ferroelectricity in hafnium oxide: cmos compatible ferroelectric field effect transistors", in 2011 ieee international electron devices meeting (iedm) (2011), pages 24.5.1–24.5.4, ISBN: 978-1-4577-0506-9, 10.1109/IEDM.2011.6131606 (cited on page 1).

[6] S. Dunkel et al., "A fefet based super-low-power ultra-fast embedded nvm technology for 22 nm fdsoi and beyond", in Iedm (2018), pages 19.7.1–19.7.4, ISBN: 978-1-5386-3559-9, 10.1109/IEDM.2017.8268425 (cited on page 1).

[7] J. Muller, E. Yurchuk, T. Schlosser, J. Paul, R. Hoffmann, S. Muller, D. Martin, S. Slesazeck, P. Polakowski, J. Sundqvist, M. Czernohorsky, K. Seidel, P. Kucher, R. Boschke, M. Trentzsch, K. Gebauer, U. Schroder, and T. Mikolajick, "Ferroelectricity in hfo 2 enables nonvolatile data storage in 28 nm hkmg", in Vlsi technology (vlsit), 2012 symposium on (2012), pages 25–26, ISBN: 978-1-4673-0846-5, 10.1109/VLSIT.2012.6242443 (cited on page 1).

[8] J. Muller et al., "Ferroelectric hafnium oxide: a cmos-compatible and highly scalable approach to future ferroelectric memories", in 2013 ieee international electron devices meeting (iedm 2013), edited by T. Ghani (2013), pages 10.8.1–10.8.4, ISBN: 978-1-4799-2306-9, 10.1109/IEDM.2013.6724605 (cited on page 1).

[9] M. Hoffmann, U. Schroeder, T. Schenk, T. Shimizu, H. Funakubo, O. Sakata, D. Pohl, M. Drescher, C. Adelmann, R. Materlik, A. Kersch, and T. Mikolajick, "Stabilizing the ferroelectric phase in doped hafnium oxide", Journal of Applied Physics **118**, 072006, ISSN: 0021-8979 (2015) 10.1063/1.4927805 (cited on pages 2, 11, 12).

[10] D. Damjanovic, "Ferroelectric, dielectric and piezoelectric properties of ferroelectric thin films and ceramics", Reports on Progress in Physics **61**, 1267 (1998) 10.1088/0034-4885/61/9/002 (cited on page 6).

[11] P. Chandra and P. B. Littlewood, in *Physics of ferroelectrics*, Vol. 105, edited by K. M. Rabe, C. H. Ahn, and J.-M. Triscone, Topics in applied physics, 0303-4216 (Springer, Berlin, 2007), pages 69–116, ISBN: 978-3-540-34590-9, 10.1007/978-3-540-34591-6_3 (cited on pages 6, 7).

[12] H. D. Megaw, "Origin of ferroelectricity in barium titanate and other perovskite-type crystals", Acta Crystallographica **5**, 739, ISSN: 0365-110X (1952) 10.1107/S0365110X52002069 (cited on page 10).

[13] S. Fatale, S. Moser, J. Miyawaki, Y. Harada, and M. Grioni, "Hybridization and electron-phonon coupling in ferroelectric $BaTiO_3$ probed by resonant inelastic x-ray scattering", Physical Review B **94**, 10.1103/PhysRevB.94.195131, ISSN: 2469-9950 (2016) 10.1103/PhysRevB.94.195131 (cited on page 10).

[14] R. Gross and A. Marx, *Festkörperphysik* (De Gruyter, 2018), ISBN: 97831105 59187, doi:10.1515/9783110559187 (cited on pages 10, 17, 22).

[15] K. Persson, *Materials data on HfO_2 (SG:29) by materials project*, An optional note, July 2014, 10.17188/1284096 (cited on page 10).

[16] J. Wang, H. P. Li, and R. Stevens, "Hafnia and hafnia-toughened ceramics", Journal of Materials Science **27**, 5397, ISSN: 0022-2461 (1992) 10.1007/BF00541601 (cited on page 11).

[17] T. S. Böscke, P. Y. Hung, P. D. Kirsch, M. A. Quevedo-Lopez, and R. Ramírez-Bon, "Increasing permittivity in HfZrO thin films by surface manipulation", Applied Physics Letters **95**, 052904, ISSN: 0003-6951 (2009) 10.1063/1.3195623 (cited on page 11).

[18] K. Tomida, K. Kita, and A. Toriumi, "Dielectric constant enhancement due to si incorporation into HfO_2", Applied Physics Letters **89**, 142902, ISSN: 0003-6951 (2006) 10.1063/1.2355471 (cited on page 11).

[19] D. Fischer and A. Kersch, "Ab initio study of high permittivity phase stabilization in HfSiO", Microelectronic Engineering **84**, 2039, ISSN: 01679317 (2007) 10.1016/j.mee.2007.04.006 (cited on page 11).

[20] C. S. Hwang, H. Funakubo, and U. Schroeder, editors, *Ferroelectricity in doped hafnium oxide: Materials properties and devices*, First edition, Woodhead Publishing series in electronic and optical materials (Woodhead Publishing, Duxford, 2019), ISBN: 0081024312 (cited on page 11).

[21] K. Ishihara, M. Maeda, and P. Shingu, "The nucleation of metastable phases from undercooled liquids", Acta Metallurgica **33**, 2113, ISSN: 00016160 (1985) 10.1016/0001-6160(85)90172-5 (cited on page 11).

[22] C.-K. Lee, E. Cho, H.-S. Lee, C. S. Hwang, and S. Han, "First-principles study on doping and phase stability of HfO_2", Physical Review B **78**, 10.1103/PhysRevB.78.012102, ISSN: 1098-0121 (2008) 10.1103/PhysRevB.78.012102 (cited on pages 12, 14).

[23] F. P. G. Fengler, M. Pešić, S. Starschich, T. Schneller, C. Künneth, U. Böttger, H. Mulaosmanovic, T. Schenk, M. H. Park, R. Nigon, P. Muralt, T. Mikolajick, and U. Schroeder, "Domain pinning: comparison of Hafnia and PZT based ferroelectrics", Advanced Electronic Materials **3**, 1600505, ISSN: 2199160X (2017) 10.1002/aelm.201600505 (cited on page 12).

[24] H. Mulaosmanovic, S. Slesazeck, J. Ocker, M. Pesic, S. Muller, S. Flachowsky, J. Muller, P. Polakowski, J. Paul, S. Jansen, S. Kolodinski, C. Richter, S. Piontek, T. Schenk, A. Kersch, C. Kunneth, R. van Bentum, U. Schroder, and T. Mikolajick, "Evidence of single domain switching in hafnium oxide based FeFETs: enabler for multi-level FeFET memory cells", in 2015 ieee international electron devices meeting (iedm) (2015), pages 26.8.1–26.8.3, ISBN: 978-1-4673-9894-7, 10.1109/IEDM.2015.7409777 (cited on page 12).

[25] R. Zhang, H. Huang, Q. Xia, C. Ye, X. Wei, J. Wang, L. Zhang, and L. Q. Zhu, "Role of oxygen vacancies at the TiO_2/HfO_2 interface in flexible oxide-based resistive switching memory", Advanced Electronic Materials **5**, 1800833 (2019) https://doi.org/10.1002/aelm.201800833 (cited on page 12).

[26] F. P. G. Fengler, R. Nigon, P. Muralt, E. D. Grimley, X. Sang, V. Sessi, R. Hentschel, J. M. LeBeau, T. Mikolajick, and U. Schroeder, "Analysis of performance instabilities of hafnia–based ferroelectrics using modulus spectroscopy and thermally stimulated depolarization currents", Advanced Electronic Materials **4**, 1700547, ISSN: 2199160X (2018) 10.1002/aelm.201700547 (cited on page 13).

[27] N. Umezawa, K. Shiraishi, T. Ohno, H. Watanabe, T. Chikyow, K. Torii, K. Yamabe, K. Yamada, H. Kitajima, and T. Arikado, "First-principles studies of the intrinsic effect of nitrogen atoms on reduction in gate leakage current through hf-based high-k dielectrics", Applied Physics Letters **86**, 143507 (2005) 10.1063/1.1899232 (cited on page 14).

[28] N. Umezawa, K. Shiraishi, Y. Akasaka, A. Oshiyama, S. Inumiya, S. Miyazaki, K. Ohmori, T. Chikyow, T. Ohno, K. Yamabe, Y. Nara, and K. Yamada, "Chemical controllability of charge states of nitrogen-related defects in HfO_xN_y : first-principles calculations", Physical Review B - PHYS REV B **77**, 10.1103/PhysRevB.77.165130 (2008) 10.1103/PhysRevB.77.165130 (cited on page 14).

[29] K. Xiong, J. Robertson, and S. J. Clark, "Passivation of oxygen vacancy states in HfO_2 by nitrogen", Journal of Applied Physics **99**, 044105 (2006) 10.1063/1.2173688 (cited on pages 14, 15, 79).

[30] C. Lee, J. Choi, M. Cho, J. Park, C. S. Hwang, H. J. Kim, and J. Jeong, "Nitrogen incorporation engineering and electrical properties of high-k gate dielectric (HfO_2 and Al_2O_3) films on si (100) substrate", Journal of Vacuum Science & Technology B: Microelectronics and Nanometer Structures Processing, Measurement, and Phenomena **22**, 1838 (2004) 10.1116/1.1775203 (cited on page 14).

[31] J. H. Kim, T. J. Park, M. Cho, J. H. Jang, M. Seo, K. D. Na, C. S. Hwang, and J. Y. Won, "Reduced electrical defects and improved reliability of atomic-layer-deposited HfO_2 dielectric films by in situ NH|sub 3| injection", Journal of The Electrochemical Society **156**, G48 (2009) 10.1149/1.3098978 (cited on page 14).

[32] S. Mueller, J. Mueller, A. Singh, S. Riedel, J. Sundqvist, U. Schroeder, and T. Mikolajick, "Incipient ferroelectricity in Al-doped HfO_2 thin films", Advanced Functional Materials **22**, 2412, ISSN: 1616301X (2012) 10.1002/adfm.201103119 (cited on page 14).

[33] X. Liu, L. Yao, Y. Cheng, B. Xiao, M. Liu, and W. Wang, "Observing large ferroelectric polarization in top-electrode-free Al:HfO_2 thin films with Al-rich strip structures", Applied Physics Letters **115**, 152901, ISSN: 0003-6951 (2019) 10.1063/1.5110668 (cited on page 14).

[34] U. Schroeder, W. Weinreich, E. Erben, J. Mueller, L. Wilde, J. Heitmann, R. Agaiby, D. Zhou, G. Jegert, and A. Kersch, "Detailed correlation of electrical and breakdown characteristics to the structural properties of ALD grown HfO_2- and ZrO2-based capacitor dielectrics", ECS Transactions **25**, 357 (2009) 10.1149/1.3205070 (cited on page 14).

[35] P. D. Lomenzo, Q. Takmeel, C. Zhou, C. M. Fancher, E. Lambers, N. G. Rudawski, J. L. Jones, S. Moghaddam, and T. Nishida, "TaN interface properties and electric field cycling effects on ferroelectric Si-doped HfO_2 thin films", Journal of Applied Physics **117**, 134105, ISSN: 0021-8979 (2015) 10.1063/1.4916715 (cited on page 14).

[36] M. H. Park, H. J. Kim, Y. J. Kim, W. Jeon, T. Moon, and C. S. Hwang, "Ferroelectric properties and switching endurance of $Hf_{0.5}Zr_{0.5}O_2$ films on TiN bottom and TiN or RuO_2 top electrodes", physica status solidi (RRL) - Rapid Research Letters **8**, 532, ISSN: 18626254 (2014) 10.1002/pssr.201409017 (cited on page 14).

[37] M. C. Cheynet, S. Pokrant, F. D. Tichelaar, and J.-L. Rouviere, "Crystal structure and band gap determination of HfO_2 thin films", Journal of Applied Physics **101**, 054101, ISSN: 0021-8979 (2007) 10.1063/1.2697551 (cited on page 14).

[38] G. Shang, P. W. Peacock, and J. Robertson, "Stability and band offsets of nitrogenated high-dielectric-constant gate oxides", Applied Physics Letters **84**, 106 (2004) 10.1063/1.1638896 (cited on page 15).

[39] L. Xu, T. Nishimura, S. Shibayama, T. Yajima, S. Migita, and A. Toriumi, "Ferroelectric phase stabilization of HfO_2 by nitrogen doping", Applied Physics Express **9**, 091501 (2016) 10.7567/apex.9.091501 (cited on pages 15, 78).

[40] R. D. Shannon, "Revised effective ionic radii and systematic studies of interatomic distances in halides and chalcogenides", Acta Crystallographica Section A **32**, 751, ISSN: 0567-7394 (1976) 10.1107/S0567739476001551 (cited on page 15).

[41] M. H. Park, Y. H. Lee, H. J. Kim, T. Schenk, W. Lee, K. D. Kim, F. P. G. Fengler, T. Mikolajick, U. Schroeder, and C. S. Hwang, "Surface and grain boundary energy as the key enabler of ferroelectricity in nanoscale hafnia-zirconia: a comparison of model and experiment", Nanoscale **9**, 9973 (2017) 10.1039/c7nr02121f (cited on page 16).

[42] D. Zhou, J. Xu, Q. Li, Y. Guan, F. Cao, X. Dong, J. Müller, T. Schenk, and U. Schröder, "Wake-up effects in Si-doped hafnium oxide ferroelectric thin films", Applied Physics Letters **103**, 192904, ISSN: 0003-6951 (2013) 10.1063/1.4829064 (cited on page 18).

[43] M. Pešić, F. P. G. Fengler, L. Larcher, A. Padovani, T. Schenk, E. D. Grimley, X. Sang, J. M. LeBeau, S. Slesazeck, U. Schroeder, and T. Mikolajick, "Physical mechanisms behind the field-cycling behavior of HfO_2-based ferroelectric capacitors", Advanced Functional Materials **26**, 4601, ISSN: 1616301X (2016) 10.1002/adfm.201600590 (cited on page 18).

[44] D. Dimos, H. N. Al–Shareef, W. L. Warren, and B. A. Tuttle, "Photoinduced changes in the fatigue behavior of $SrBi_2Ta_2O_9$ and $Pb(Zr,Ti)O_3$ thin films", Journal of Applied Physics **80**, 1682, ISSN: 0021-8979 (1996) 10.1063/1.362968 (cited on page 19).

[45] W. L. Warren, D. Dimos, B. A. Tuttle, G. E. Pike, R. W. Schwartz, P. J. Clews, and D. C. McIntyre, "Polarization suppression in $Pb(Zr,Ti)O_3$ thin films", Journal of Applied Physics **77**, 6695, ISSN: 0021-8979 (1995) 10.1063/1.359083 (cited on page 19).

[46] J. Rodriguez, K. Remack, J. Gertas, L. Wang, C. Zhou, K. Boku, J. Rodriguez-Latorre, K. R. Udayakumar, S. Summerfelt, T. Moise, D. Kim, J. Groat, J. Eliason, M. Depner, and F. Chu, "Reliability of ferroelectric random access memory embedded within 130nm CMOS", in 2010 ieee international reliability physics symposium (2010), pages 750–758, 10.1109/IRPS.2010.5488738 (cited on page 20).

[47] S. Hüfner, *Photoelectron spectroscopy: Principles and applications*, Vol. 82, Springer series in solid-state sciences (Springer, Berlin and Heidelberg, 1995), ISBN: 0387191089 (cited on pages 21, 23).

[48] S. Tanuma, C. J. Powell, and D. R. Penn, "Calculations of electron inelastic mean free paths. ix. data for 41 elemental solids over the 50 ev to 30 kev range", Surface and Interface Analysis **43**, 689 (2011) https://doi.org/10.1002/sia.3522 (cited on pages 21, 29, 30).

[49] I. V. Hertel and C.-P. Schulz, *Atome, Moleküle und optische Physik 1: Atome und Grundlagen ihrer Spektroskopie*, 2. Aufl. 2017, Springer-Lehrbuch (Springer Berlin Heidelberg, Berlin, Heidelberg, 2017), ISBN: 9783662531044 (cited on pages 22, 31).

[50] F. A. Stevie and C. L. Donley, "Introduction to x-ray photoelectron spectroscopy", Journal of Vacuum Science & Technology A **38**, 063204 (2020) 10.1116/6.0000412 (cited on page 24).

[51] J. F. Moulder, W. F. Stickle, W. M. Sobol, and K. D. Bomben, *Handbook of x-ray photoelectron spectroscopy* (1992) (cited on page 26).

[52] S. Tougaard, "Improved xps analysis by visual inspection of the survey spectrum", Surface and Interface Analysis **50**, 657 (2018) https://doi.org/10.1002/sia.6456 (cited on page 27).

[53] M. H. Engelhard, D. R. Baer, A. Herrera-Gomez, and P. M. A. Sherwood, "Introductory guide to backgrounds in xps spectra and their impact on determining peak intensities", Journal of Vacuum Science & Technology A **38**, 063203 (2020) 10.1116/6.0000359 (cited on pages 27, 28).

[54] A. Proctor and P. M. A. Sherwood, "Data analysis techniques in x-ray photoelectron spectroscopy", Analytical Chemistry **54**, 13 (1982) 10.1021/ac00238a008 (cited on page 27).

[55] J. Yeh and I. Lindau, "Atomic subshell photoionization cross sections and asymmetry parameters: $1 \geq z \geq 103$", Atomic Data and Nuclear Data Tables **32**, 1, ISSN: 0092-640X (1985) https://doi.org/10.1016/0092-640X(85)90016-6 (cited on page 30).

[56] M. B. Trzhaskovskaya and V. G. Yarzhemsky, "Dirac–Fock photoionization parameters for HAXPES applications", Atom. Data Nucl. Data Tabl. **119**, 99 (2018) 10.1016/j.adt.2017.04.003 (cited on pages 30, 99, 100).

[57] J. Woicik, *Hard X-Ray Photoelectron Spectroscopy (HAXPES)*, Vol. v.59, Springer Series in Surface Sciences Ser (Springer International Publishing AG, Cham, 2016), ISBN: 9783319240435 (cited on pages 31, 51, 53).

[58] W. Demtröder, *Experimentalphysik 2: elektrizität und optik*, 6., überarb. u. akt. Aufl. 2013, Springer-Lehrbuch (Springer Berlin Heidelberg, Berlin, Heidelberg, 2013), ISBN: 9783642299445 (cited on pages 31, 32).

[59] W. Drube, *X-ray spectroscopy beamline P22 HAXPES/HAXPEEM-Technical Design Report*, Hamburg, Oct. 2014 (cited on pages 32, 34, 35).

[60] Brouder and Hikam, "Multiple-scattering theory of magnetic x-ray circular dichroism", Physical review. B, Condensed matter **43**, 3809, ISSN: 0163-1829 (1991) 10.1103/physrevb.43.3809 (cited on page 32).

[61] C. Schlueter, A. Gloskovskii, K. Ederer, I. Schostak, S. Piec, I. Sarkar, Y. Matveyev, P. Lömker, M. Sing, R. Claessen, C. Wiemann, C. M. Schneider, K. Medjanik, G. Schönhense, P. Amann, A. Nilsson, and W. Drube, "The new dedicated HAXPES beamline P22 at PETRAIII", AIP Conference Proceedings **2054**, 040010 (2019) 10.1063/1.5084611 (cited on page 32).

[62] K. W. Hideaki Adachi Tomonobu Hata, in *Materials science of thin films (second edition)*, edited by M. Ohring, Second Edition (Academic Press, San Diego, 2002), pages 295–359, ISBN: 978-0-12-524975-1, https://doi.org/10.1016/B978-012524975-1/50001-X (cited on page 38).

[63] A. Pakkala and M. Putkonen, in *Handbook of deposition technologies for films and coatings (third edition)*, edited by P. M. Martin, Third Edition (William Andrew Publishing, Boston, 2010), pages 364–391, ISBN: 978-0-8155-2031-3, https://doi.org/10.1016/B978-0-8155-2031-3.00008-9 (cited on page 38).

[64] T. **Szyjka**, L. Baumgarten, T. Mittmann, Y. Matveyev, C. Schlueter, T. Mikolajick, U. Schroeder, and M. Müller, "Enhanced ferroelectric polarization in TiN/HfO_2/TiN capacitors by interface design", ACS Applied Electronic Materials **2**, 3152 (2020) 10.1021/acsaelm.0c00503 (cited on pages 42, 61, 64, 66–68, 77).

[65] T. Mittmann, M. Materano, P. D. Lomenzo, M. H. Park, I. Stolichnov, M. Cavalieri, C. Zhou, C.-C. Chung, J. L. Jones, T. **Szyjka**, M. Müller, A. Kersch, T. Mikolajick, and U. Schroeder, "Origin of ferroelectric phase in undoped HfO_2 films deposited by sputtering", Adv.. Mater. Interfaces **6**, 1900042 (2019) 10.1002/admi.201900042 (cited on pages 42, 44, 61, 67–69).

[66] L. Baumgarten, T. **Szyjka**, T. Mittmann, M. Materano, Y. Matveyev, C. Schlueter, T. Mikolajick, U. Schroeder, and M. Müller, "Impact of vacancies and impurities on ferroelectricity in PVD- and ALD-grown HfO_2 films", Applied Physics Letters **118**, 032903 (2021) 10.1063/5.0035686 (cited on pages 42, 61, 71, 72, 74–77, 105).

[67] M. Müller, P. Lömker, P. Rosenberger, M. Hussein Hamed, D. N. Mueller, R. A. Heinen, T. **Szyjka**, and L. Baumgarten, "Hard x-ray photoelectron spectroscopy of tunable oxide interfaces", Journal of Vacuum Science & Technology A **40**, 013215 (2022) 10.1116/6.0001491 (cited on pages 42, 61, 87, 90).

[68] T. **Szyjka**, L. Baumgarten, T. Mittmann, Y. Matveyev, C. Schlueter, T. Mikolajick, U. Schroeder, and M. Müller, "Chemical stability of IrO_2 top electrodes in ferroelectric $Hf_{0.5}Zr_{0.5}O_2$-based metal–insulator–metal structures: The impact of annealing gas", physica status solidi (RRL) – Rapid Research Letters **15**, 2100027 (2021) https://doi.org/10.1002/pssr.202100027 (cited on pages 42, 61, 81, 83, 86, 87, 89, 93).

[69] T. Mittmann, T. **Szyjka**, H. Alex, M. C. Istrate, P. D. Lomenzo, L. Baumgarten, M. Müller, J. L. Jones, L. Pintilie, T. Mikolajick, and U. Schroeder, "Impact of iridium oxide electrodes on the ferroelectric phase of thin $Hf_{0.5}Zr_{0.5}O_2$ films", physica status solidi (RRL) – Rapid Research Letters **n/a**, 2100012 (2021) https://doi.org/10.1002/pssr.202100012 (cited on pages 42, 61, 87).

[70] The HDF Group, *Hierarchical data format version 5*, (2022) http://www.hdfgroup.org/HDF5 (cited on page 46).

[71] OriginLab Corporation, *OriginPro*, version Version 2021, 2021 (cited on page 46).

[72] P. H. Citrin and D. R. Hamann, "Phonon broadening of x-ray photoemission line shapes in solids and its independence of hole state lifetimes", Physical Review B **15**, 2923, ISSN: 1098-0121 (1977) 10.1103/PhysRevB.15.2923 (cited on page 51).

[73] D. Jaeger and J. Patscheider, "A complete and self-consistent evaluation of XPS spectra of TiN", Journal of Electron Spectroscopy and Related Phenomena **185**, 523, ISSN: 0368-2048 (2012) https://doi.org/10.1016/j.elspec.2012.10.011 (cited on pages 52, 62).

[74] E. O. Filatova, A. S. Konashuk, S. S. Sakhonenkov, A. A. Sokolov, and V. V. Afanas'ev, "Re-distribution of oxygen at the interface between γ-Al_2O_3 and TiN", Scientific reports **7**, 4541 (2017) 10.1038/s41598-017-04804-4 (cited on page 52).

[75] N. C. Saha and H. G. Tompkins, "Titanium nitride oxidation chemistry: an x-ray photoelectron spectroscopy study", Journal of Applied Physics **72**, 3072 (1992) 10.1063/1.351465 (cited on pages 52, 63).

[76] E. A. Kraut, R. W. Grant, J. R. Waldrop, and S. P. Kowalczyk, "Precise determination of the valence-band edge in x-ray photoemission spectra: application to measurement of semiconductor interface potentials", Physical Review Letters **44**, 1620, ISSN: 0031-9007 (1980) 10.1103/PhysRevLett.44.1620 (cited on page 53).

[77] E. A. Kraut, R. W. Grant, J. R. Waldrop, and S. P. Kowalczyk, "Semiconductor core-level to valence-band maximum binding-energy differences: precise determination by x-ray photoelectron spectroscopy", Physical review. B, Condensed matter **28**, 1965, ISSN: 0163-1829 (1983) 10.1103/PhysRevB.28.1965 (cited on page 53).

[78] A. Jablonski and C. Powell, "Electron effective attenuation lengths in electron spectroscopies", Journal of Alloys and Compounds **362**, Proceedings of the Sixth International School and Symposium on Synchrotron Radiation in Natural Science (ISSRNS), 26, ISSN: 0925-8388 (2004) https://doi.org/10.1016/S0925-8388(03)00558-9 (cited on page 56).

[79] A. Jablonski and C. Powell, "Effective attenuation lengths for photoelectrons emitted by high-energy laboratory X-ray sources", Journal of Electron Spectroscopy and Related Phenomena **199**, 27, ISSN: 0368-2048 (2015) https://doi.org/10.1016/j.elspec.2014.12.011 (cited on page 56).

[80] W. Werner, W. Smekal, C. Powell, and J. Gorham, *Simulation of Electron Spectra for Surface Analysis (SESSA)Version 2.2 User's Guide*, en, 2021, https://doi.org/10.6028/NIST.NSRDS.100-2021 (cited on page 56).

[81] I. Bertóti, M. Mohai, J. Sullivan, and S. Saied, "Surface characterisation of plasma-nitrided titanium: an XPS study", Applied Surface Science **84**, 357, ISSN: 0169-4332 (1995) https://doi.org/10.1016/0169-4332(94)00545-1 (cited on pages 62, 66).

[82] M. Sowinska, T. Bertaud, D. Walczyk, S. Thiess, P. Calka, L. Alff, C. Walczyk, and T. Schroeder, "In-operando hard X-ray photoelectron spectroscopy study on the impact of current compliance and switching cycles on oxygen and carbon defects in resistive switching Ti/HfO_2/TiN cells", J. Appl. Phys. **115**, 204509 (2014) 10.1063/1.4879678 (cited on page 62).

[83] T. Schroeder, G. Lupina, R. Sohal, G. Lippert, C. Wenger, O. Seifarth, M. Tallarida, and D. Schmeisser, "Synchrotron radiation x-ray photoelectron spectroscopy study on the interface chemistry of high-k $Pr_xAl_{2-x}O_3$ (x=0–2) dielectrics on TiN for dynamic random access memory applications", Journal of Applied Physics **102**, 014103 (2007) 10.1063/1.2749468 (cited on page 62).

[84] C. Ernsberger, J. Nickerson, A. E. Miller, and J. Moulder, "Angular resolved x-ray photoelectron spectroscopy study of reactively sputtered titanium nitride", Journal of Vacuum Science & Technology A **3**, 2415 (1985) 10.1116/1.572849 (cited on page 63).

[85] S. Suzer, S. Sayan, M. M. Banaszak Holl, E. Garfunkel, Z. Hussain, and N. M. Hamdan, "Soft x-ray photoemission studies of Hf oxidation", Journal of Vacuum Science & Technology A **21**, 106 (2003) 10.1116/1.1525816 (cited on page 65).

[86] I. Milošv, H.-H. Strehblow, B. Navinšek, and M. Metikoš-Huković, "Electrochemical and thermal oxidation of tin coatings studied by xps", Surface and Interface Analysis **23**, 529 (1995) 10.1002/sia.740230713 (cited on page 66).

[87] A. Glaser, S. Surnev, F. Netzer, N. Fateh, G. Fontalvo, and C. Mitterer, "Oxidation of vanadium nitride and titanium nitride coatings", Surface Science **601**, 1153, ISSN: 0039-6028 (2007) https://doi.org/10.1016/j.susc.2006.12.010 (cited on page 66).

[88] N. C. Saha and H. G. Tompkins, "Titanium nitride oxidation chemistry: an x-ray photoelectron spectroscopy study", Journal of Applied Physics **72**, 3072 (1992) 10.1063/1.351465 (cited on page 66).

[89] E. Bruninx, A. F. P. M. Van Eenbergen, P. Van Der Werf, and J. Haisma, "X-ray photoelectron spectroscopy of hafnium nitride", Journal of Materials Science **21**, 541, ISSN: 1573-4803 (1986) 10.1007/BF01145521 (cited on page 66).

[90] M. Lee, Z.-H. Lu, W.-T. Ng, D. Landheer, X. Wu, and S. Moisa, "Interfacial growth in HfO_xN_y gate dielectrics deposited using $[(C_2H_5)_2N]_4Hf$ with O_2 and NO", Applied Physics Letters **83**, 2638 (2003) 10.1063/1.1608488 (cited on page 66).

[91] J.-C. Dupin, D. Gonbeau, P. Vinatier, and A. Levasseur, "Systematic XPS studies of metal oxides, hydroxides and peroxides", Phys. Chem. Chem. Phys. **2**, 1319 (2000) 10.1039/A908800H (cited on pages 75, 91).

[92] Y. Lai, Z. Zeng, C. Liao, S. Cheng, J. Yu, Q. Zheng, and P. Lin, "Ultralow switching current in HfO_x/ZnO bilayer with tunable switching power enabled by plasma treatment", Applied Physics Letters **109**, 063501 (2016) 10.1063/1.4960798 (cited on pages 75, 91).

[93] C.-Y. Huang, C.-Y. Huang, T.-L. Tsai, C.-A. Lin, and T.-Y. Tseng, "Switching mechanism of double forming process phenomenon in ZrO_x/HfO_y bilayer resistive switching memory structure with large endurance", Applied Physics Letters **104**, 062901 (2014) 10.1063/1.4864396 (cited on pages 75, 91).

[94] C. Zheng, G. He, X. Chen, M. Liu, J. Lv, J. Gao, J. Zhang, D. Xiao, P. Jin, S. Jiang, W. Li, and Z. Sun, "Modification of band alignments and optimization of electrical properties of InGaZnO MOS capacitors with high-k HfO_xN_y gate dielectrics", Journal of Alloys and Compounds **679**, 115, ISSN: 0925-8388 (2016) https://doi.org/10.1016/j.jallcom.2016.04.025 (cited on page 77).

[95] K. D. Kim, M. H. Park, H. J. Kim, Y. J. Kim, T. Moon, Y. H. Lee, S. D. Hyun, T. Gwon, and C. S. Hwang, "Ferroelectricity in undoped-HfO_2 thin films induced by deposition temperature control during atomic layer deposition", J. Mater. Chem. C **4**, 6864 (2016) 10.1039/C6TC02003H (cited on pages 77, 78).

[96] S. Karwal, M. A. Verheijen, B. L. Williams, T. Faraz, W. M. M. Kessels, and M. Creatore, "Low resistivity hfnx grown by plasma-assisted ald with external rf substrate biasing", J. Mater. Chem. C **6**, 3917 (2018) 10.1039/C7TC05961B (cited on page 77).

[97] Y. Zhou, Y. K. Zhang, Q. Yang, J. Jiang, P. Fan, M. Liao, and Y. C. Zhou, "The effects of oxygen vacancies on ferroelectric phase transition of HfO_2-based thin film from first-principle", Computational Materials Science **167**, 143, ISSN: 09270256 (2019) 10.1016/j.commatsci.2019.05.041 (cited on page 78).

[98] K. Hans, S. Latha, P. Bera, and H. C. Barshilia, "Hafnium carbide based solar absorber coatings with high spectral selectivity", Solar Energy Materials and Solar Cells **185**, 1, ISSN: 09270248 (2018) 10.1016/j.solmat.2018.05.005 (cited on page 78).

[99] H. Fujisawa, S. Hyodo, K. Jitsui, M. Shimizu, H. Niu, H. Okino, and T. Shiosaki, "Electrical properties of PZT thin films grown on Ir/IrO_2 bottom electrodes by MOCVD", Integrated Ferroelectrics **21**, 107 (1998) 10.1080/10584589808202055 (cited on page 81).

[100] T. Nakamura, Y. Nakao, A. Kamisawa, and H. Takasu, "Preparation of $Pb(Zr,Ti)O_3$ thin films on Ir and IrO_2 electrodes", Japanese Journal of Applied Physics **33**, 5207 (1994) 10.1143/jjap.33.5207 (cited on page 81).

[101] M. H. Hamed, D. N. Mueller, and M. Müller, "Thermal phase design of ultrathin magnetic iron oxide films: from Fe_3O_4 to γ-Fe_2O_3 and FeO", J. Mater. Chem. C **8**, 1335 (2020) 10.1039/C9TC05921K (cited on page 82).

[102] S. J. Freakley, J. Ruiz-Esquius, and D. J. Morgan, "The x-ray photoelectron spectra of Ir, IrO_2 and $IrCl_3$ revisited", Surface and Interface Analysis **49**, 794 (2017) https://doi.org/10.1002/sia.6225 (cited on pages 82, 84).

[103] M. J. Heikkilä, J. Hämäläinen, E. Puukilainen, M. Leskelä, and M. Ritala, "High-temperature x-ray scattering studies of atomic layer deposited IrO_2", Journal of Applied Crystallography **53**, 369 (2020) 10.1107/S1600576720001053 (cited on page 84).

[104] J. Arblaster, "Densities of osmium and iridium recalculations based upon a review of the latest crystallographic data", (1989) (cited on page 84).

[105] Z. Novotny, B. Tobler, L. Artiglia, M. Fischer, M. Schreck, J. Raabe, and J. Osterwalder, "Kinetics of the thermal oxidation of ir(100) toward iro2 studied by ambient-pressure x-ray photoelectron spectroscopy", The journal of physical chemistry letters **11**, 3601 (2020) 10.1021/acs.jpclett.0c00914 (cited on page 85).

[106] G. N. Derry, M. E. Kern, and E. H. Worth, "Recommended values of clean metal surface work functions", Journal of Vacuum Science & Technology A: Vacuum, Surfaces, and Films **33**, 060801, ISSN: 0734-2101 (2015) 10.1116/1.4934685 (cited on page 86).

[107] J. M. Bernhard, "Work function study of iridium oxide and molybdenum using ups and simultaneous fowler-nordheim I-V plots with field emission energy distributions", PhD thesis (University of North Texas, Jan. 1999) (cited on page 86).

Own Publications

[1] T. **Szyjka**, L. Baumgarten, T. Mittmann, Y. Matveyev, C. Schlueter, T. Mikolajick, U. Schroeder, and M. Müller, "Enhanced ferroelectric polarization in TiN/HfO_2/TiN capacitors by interface design", ACS Applied Electronic Materials **2**, 3152 (2020) 10.1021/acsaelm.0c00503.

[2] L. Baumgarten, T. **Szyjka**, T. Mittmann, M. Materano, Y. Matveyev, C. Schlueter, T. Mikolajick, U. Schroeder, and M. Müller, "Impact of vacancies and impurities on ferroelectricity in PVD- and ALD-grown HfO_2 films", Applied Physics Letters **118**, 032903 (2021) 10.1063/5.0035686.

[3] T. **Szyjka**, L. Baumgarten, T. Mittmann, Y. Matveyev, C. Schlueter, T. Mikolajick, U. Schroeder, and M. Müller, "Chemical stability of IrO_2 top electrodes in ferroelectric $Hf_{0.5}Zr_{0.5}O_2$-based metal–insulator–metal structures: The impact of annealing gas", physica status solidi (RRL) – Rapid Research Letters **15**, 2100027 (2021) https://doi.org/10.1002/pssr.202100027.

[4] M. Müller, P. Lömker, P. Rosenberger, M. Hussein Hamed, D. N. Mueller, R. A. Heinen, T. **Szyjka**, and L. Baumgarten, "Hard x-ray photoelectron spectroscopy of tunable oxide interfaces", Journal of Vacuum Science & Technology A **40**, 013215 (2022) 10.1116/6.0001491.

[5] T. **Szyjka**, L. Baumgarten, O. Rehm, C. Richter, Y. Matveyev, C. Schlueter, T. Mikolajick, U. Schroeder, and M. Müller, "From Doping to Dilution: Local Chemistry and Collective Interactions of La in HfO_2", physica status solidi (RRL) – Rapid Research Letters **n/a**, 2100582 https://doi.org/10.1002/pssr.202100582.

[6] T. Mittmann, M. Materano, P. D. Lomenzo, M. H. Park, I. Stolichnov, M. Cavalieri, C. Zhou, C.-C. Chung, J. L. Jones, T. **Szyjka**, M. Müller, A. Kersch, T. Mikolajick, and U. Schroeder, "Origin of ferroelectric phase in undoped HfO_2 films deposited by sputtering", Adv.. Mater. Interfaces **6**, 1900042 (2019) 10.1002/admi.201900042.

[7] T. Mittmann, T. **Szyjka**, H. Alex, M. C. Istrate, P. D. Lomenzo, L. Baumgarten, M. Müller, J. L. Jones, L. Pintilie, T. Mikolajick, and U. Schroeder, "Impact of iridium oxide electrodes on the ferroelectric phase of thin $Hf_{0.5}Zr_{0.5}O_2$ films", physica status solidi (RRL) – Rapid Research Letters **n/a**, 2100012 (2021) https://doi.org/10.1002/pssr.202100012.

Conference Contributions

[1] T. Szyjka, *HAXPES study of oxygen vacancies forming in thin film HfO_2-based MIM structures*, DPG-Frühjahrstagung 2019, Regensburg, Apr. 2019.

[2] T. Szyjka, *HAXPES study of oxygen vacancies forming in thin film HfO_2-based ferroelectric capacitors*, High-K Workshop 2019, Dresden, June 2019.

[3] T. Szyjka, *Enhanced ferroelectric polarization in $TiN/HfO_2/TiN$ capacitors by interface design*, DESY user workshop, Hamburg, Jan. 2021.

[4] T. Szyjka, *Spectroscopic correlation of oxygen(-vacancies) and emerging ferroelectricity in HfO_2 and HZO by HAXPES*, E-MRS 2021 Fall Meeting, Hamburg, Sept. 2021.

Acknowledgement

Zum Abschluss der Arbeit bleibt nur noch Danke zu sagen. Zunächst gilt mein Dank Prof. Dr. Martina Müller für die Möglichkeit der Promotion an einem Thema, welches nicht nur von der Grundlagenforschung her spannend ist, sondern auch Anwendung in naher Zukunft finden wird. Ihr und Dr. Lutz Baumgarten danke ich für die gemeinsame Arbeit, erhellenden Diskussionen und wertvolle Unterstützung.
Weiterer Dank gilt Terence Mittmann und Dr. Uwe Schröder, für die zur Verfügung gestellten Proben und Zusammenarbeit, durch die diese Arbeit erst in dieser Form möglich wurde.
Meinen Kolleg*innen Paul Rosenberger, Dr. Mai Hamed, Dr. Ronja Heinen und Pia Düring danke ich für die Freundschaft, Unterhaltungen und Unterstützung, insbesondere während der Messzeiten.
Mein Dank gilt auch den Wissenschaftlern und Kollegen an der Beamline P22, namentlich Dr. Yury Matveyev, Dr. Patrick Lömker, und Dr. Christoph Schlüter, für die Hilfe und aufschlussreichen Diskussionen während der Messzeiten.
Allen Kollegen am PGI-6 für die angenehme Atmosphäre und inspirierenden Unterhaltungen. Insbesondere, Dr. Carsten Wiemann, Dr. Stefan Cramm, für die Aushilfe bei den Messzeiten und Dr. David Müller für das beigesteuerte Chemie Fachwissen.
Es hat mich gefreut Oliver Rehm bei seiner Bachelorarbeit betreuen zu dürfen und gemeinsam mit ihm Datensätze aufarbeiten zu können, welche auch dadurch publiziert werden konnten.
Allen die diese Arbeit vorab gelesen und Verbesserungsvorschläge gegeben haben (*Takk*: Jaka B., Dr. Lutz B., Lukas S., Dr. Amran A. und Melanie B.).
Mein besonderer Dank gilt meinen Eltern, die mich in all meinen Entscheidungen unterstützt haben und auf die ich immer bauen konnte. Ebenso bin ich dankbar für die emotionale Unterstützung und die Hilfsbereitschaft meiner Geschwister und Freunde. Ich schätze mich glücklich, überhaupt so weit im Leben gekommen zu sein, dass ich eine Promotion abschließen durfte. Zu guter Letzt gilt mein Dank meiner liebsten Melanie für wunderschöne, von Glück geprägten Jahre, in denen sie immer an mich geglaubt und mir mit ihrer bedingungslosen Unterstützung den Rücken frei gehalten hat [5×5].

Band / Volume 80
Integrated Control Electronics for Qubits at Ultra Low Temperature
D. Nielinger (2022), xviii, 94, xix-xxvi
ISBN: 978-3-95806-631-1

Band / Volume 81
Higher-order correlation analysis in massively parallel recordings in behaving monkey
A. Stella (2022), xiv, 184 pp
ISBN: 978-3-95806-640-3

Band / Volume 82
Denoising with Quantum Machine Learning
J. Pazem (2022), 106 pp
ISBN: 978-3-95806-641-0

Band / Volume 83
Hybrid hydrogels promote physiological functionality of long-term cultured primary neuronal cells in vitro
C. Meeßen (2022), x, 120 pp
ISBN: 978-3-95806-643-4

Band / Volume 84
Surface states and Fermi-level pinning on non-polar binary and ternary (Al,Ga)N surfaces
L. Freter (2022), 137 pp
ISBN: 978-3-95806-644-1

Band / Volume 85
Dynamical and statistical structure of spatially organized neuronal networks
M. Layer (2022), xiii, 167 pp
ISBN: 978-3-95806-651-9

Band / Volume 86
Persistent firing and oscillations in the septo-hippocampal systemand their relation to locomotion
K. Korvasová (2022), 111 pp
ISBN: 978-3-95806-654-0

Band / Volume 87
Sol-Gel-Synthese, Tintenstrahldruck und Blitzlampentemperung von Tantaloxid-Dünnschichten zur pH-Messung
C. D. Beale (2022), xlix, 339 pp
ISBN: 978-3-95806-656-4

Band / Volume 88
Diversity of chiral magnetic solitons
V. Kuchkin (2022), xiv, 155 pp
ISBN: 978-3-95806-665-6

Band / Volume 89
Controlling the electrical properties of oxide heterointerfaces through their interface chemistry
M.-A. Rose (2022), vi, 162 pp
ISBN: 978-3-95806-667-0

Band / Volume 90
Modeling and Suppressing Unwanted Parasitic Interactions in Superconducting Circuits
X. Xu (2022), 123, XVIII pp
ISBN: 978-3-95806-671-7

Band / Volume 91
Activating molecular magnetism by controlled on-surface coordination
I. Cojocariu (2022), xi, 169 pp
ISBN: 978-3-95806-674-8

Band / Volume 92
Computational study of structural and optical properties of two-dimensional transition-metal dichalcogenides with implanted defects
S. H. Rost (2023), xviii, 198 pp
ISBN: 978-3-95806-682-3

Band / Volume 93
DC and RF characterization of bulk CMOS and FD-SOI devices at cryogenic temperatures with respect to quantum computing applications
A. Artanov (2023), xv, 80, xvii-liii pp
ISBN: 978-3-95806-687-8

Band / Volume 94
HAXPES study of interface and bulk chemistry of ferroelectric HfO_2 capacitors
T. Szyjka (2023), viii, 120 pp
ISBN: 978-3-95806-692-2

Weitere ***Schriften des Verlags im Forschungszentrum Jülich*** unter
http://wwwzb1.fz-juelich.de/verlagextern1/index.asp

Information
Band / Volume 94
ISBN 978-3-95806-692-2

Mitglied der Helmholtz-Gemeinschaft

JÜLICH
Forschungszentrum